

Fall 11-15-2016

Antimonide-based superlattice membranes for infrared applications

Seyedeh marziyeh Zamiri
University of New Mexico

Follow this and additional works at: https://digitalrepository.unm.edu/ece_etds



Part of the [Electrical and Computer Engineering Commons](#)

Recommended Citation

Zamiri, Seyedeh marziyeh. "Antimonide-based superlattice membranes for infrared applications." (2016).
https://digitalrepository.unm.edu/ece_etds/308

This Dissertation is brought to you for free and open access by the Engineering ETDs at UNM Digital Repository. It has been accepted for inclusion in Electrical and Computer Engineering ETDs by an authorized administrator of UNM Digital Repository. For more information, please contact disc@unm.edu.

Seyedeh Marziyeh Zamiri

Candidate

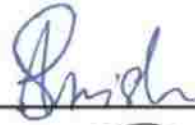
Electrical and Computer Engineering (ECE)

Department

This dissertation is approved, and it is acceptable in quality and form for publication:

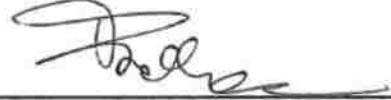
Approved by the Dissertation Committee:

Prof. Sanjay Krishna (UNM)

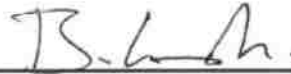


, Chairperson

Prof. Francesca Cavallo (UNM)



Prof. Ganesh Balakrishnan (UNM)



Prof. Ali Javey (UC Berkeley)



11/14/2016

Dr. Edward Smith (Raytheon)



11/14/2016

Antimonide-based superlattice membranes for infrared applications

by

Seyedeh Marziyeh Zamiri

B.S., Electrical Engineering, Isfahan University of Technology,
Isfahan, Iran, 2006

M.S., Photonics, Shahid Beheshti University, Tehran, Iran, 2009

THESIS

Submitted in Partial Fulfillment of the
Requirements for the Degree of

Doctor of Philosophy
Engineering

The University of New Mexico

Albuquerque, New Mexico

December, 2016

Dedication

*To my best friend and husband, for his unconditional support and encouragement
and
My lovely parents for being there for me*

Acknowledgments

I was so lucky to have great family, friends and colleagues during the past few years and in my whole life who helped and supported me till I get to the point to pursue my Ph.D. First, I would like to thank my academic advisor Dr. Sanjay Krishna, without whom I could not fulfill this. Even though, as the CHTM director, he was very busy in the past few years but whenever I had a question or I was totally confused about where I was and where I was supposed to go in my research, he was always available and very helpful to keep me going in the right direction. I also appreciate Prof. Francesca Cavallo for being always available and supportive. She taught me a lot about science and more important she taught me how to be a strong woman. My dissertation committee, Prof. Balakrishnan, Prof. Ali Javey, and Dr. Edward Smith have helped me to have progress in my research, indeed.

It has been an honor for me to work with my group members, other students and staff at CHTM. Students who have been part of the office # 117 in the past and present, Ajit, Nutan, Stephen, Brianna, Lilian, Emma, Happy, Vinita, Amy, Ted, Seung Hyun, Zahra, Shima, I learn a lot from all of you.

I would appreciate Stephen and Brianna a lot for being such good friends and mentors. I spent a lot of time with them to learn how to do material processing, characterization and more important how to be patient in doing experiment. I also would appreciate CHTM staff in the past and present, Joel, Dan, Rick, Douglas, Steve, Beth, Andrew, Joe M, Mike, Ron, Josh, Pat, Joe S, Wesley, Tamara, Jessica, Pam, Karen, and Stefi, Janell, and Chris.

My parents, my brother and sister have always been supportive and cheered me whenever I felt I was down and I needed them. The same is true for my in-laws. Thank you all for being such an awesome family.

My special thank goes to my husband Amin Rasoulof. Even though we went through really hard time during last two years but I always had him and his support with me which means a lot to me.

Antimonide-based superlattice membranes for infrared applications

by

Seyedeh Marziyeh Zamiri

B.S., Electrical Engineering, Isfahan University of Technology,

Isfahan, Iran, 2006

M.S., Photonics, Shahid Beheshti University, Tehran, Iran, 2009

Doctor of Philosophy, Engineering, University of New Mexico, 2016

Abstract

Semiconductor membranes offer an interesting materials and device development platform due to their ability to integrate dissimilar materials through a print, stamp and transfer process. There is a lot of interest in integrating antimonide based type-II superlattices (T2SL) onto inexpensive substrates, such as Si, to not only undertake fundamental studies into the optical, electronic and structural properties of the superlattices but also to fabricate wafer-level infrared (IR) photodetectors. An effective approach to transfer type-II superlattice membranes (T2SL-M) onto alternate substrates is based on membrane release from the native GaSb substrate followed by the transfer to a new host substrate. In this work, I have transferred InAs/GaSb and InAs/InAsSb T2SLs with different in-plane geometries from a GaSb substrate to a variety of host substrates, including Si, polydimethylsiloxane and metal coated surfaces. Electron microscopy shows structural integrity of transferred membranes with thicknesses ranging from 100 nm to 2.5 μm and lateral sizes from 24x24 μm^2

to 1x1 cm². Atomic force and electron microscopy reveal the excellent quality of the membrane interface with the new host. The crystalline structure of the membrane is not altered by the fabrication process, and minimal elastic relaxation occurs during the release step, as demonstrated by X-ray diffraction and mechanical modeling. I have also used the antimonide superlattice membranes to realize wafer level infrared detectors on silicon substrates without using conventional Indium-bump hybridization. In this approach, PIN superlattices are grown on top of a 60 nm Al_{0.6}Ga_{0.4}Sb sacrificial layer on a GaSb host substrate. Following the growth, I have transferred the individual pixels using an epitaxial lift-off technique, which consists of a wet-etch to undercut the pixels followed by a dry-stamp process to transfer the pixels to a silicon substrate prepared with a gold layer. I have done structural and optical characterization of the transferred pixels using an optical microscope, scanning electron microscopy, and photo luminescence. The interface between the transferred pixels and the new substrate is abrupt, and no significant degradation in the optical quality is observed. Next, I have fabricated an indium-bump-free membrane detector using this approach. Spectral response measurements and the current-voltage characteristics of an infrared photodetector, based on the InAs/InAsSb superlattice, bonded to Si demonstrates the functionality of transferred membranes in the infrared range. The performance of the membrane detector is compared to a control detector using the as-grown epitaxial material. The proposed approach to fabricate Indium-bump free detectors could pave the way for wafer-level integration of photonic detectors on silicon substrates, which could dramatically reduce the cost of these detectors. Since the release of T2SL-M is achieved using a high etch selectivity between the active region and the Al-containing sacrificial layers, a poor selectivity between the sacrificial layers and a variety of T2SL active regions will result in significant damage to the active layer of an IR detector. I have developed a novel two-step etching process to protect the T2SL-M while the sacrificial layer is etched away. In this process, both the top surface and the sidewalls of the membrane are coated with

a hard-baked polymer film (i.e., photoresist), and therefore they are unexposed to the chemical etchant. For Al and Ga containing compounds, with no membrane isolation, this process leads to rough sidewalls which are expected to increase surface recombination in the membrane and therefore increases the dark current density of an IR detector. I have quantified this effect by characterizing T2SL IR detectors fabricated on isolated and non-isolated mesas. A comparative analysis of the dark current density measured for the two devices signify the effect of having exposed sidewalls during membrane release. These experimental results are consistent with theoretical calculations which show a relative enhancement of surface recombination with increasing roughness of the membrane sidewalls. The development of these Sb based T2SL membranes opens up new exciting prospects for material science studies and device architecture integration.

Contents

List of Figures	xi
List of Tables	xv
1 Introduction	1
1.1 Background	1
1.1.1 Fundamental material study	3
1.1.2 Technological challenges	3
1.2 Outline of dissertation	5
1.3 Contributions of this work	6
1.4 Publications	7
2 Materials and methods	10
2.1 Theory and Design of Heterostructures	11
2.1.1 Material Design	11
2.1.2 Strain Engineering	13

Contents

2.2	Material growth and characterization	16
2.2.1	Molecular Beam Epitaxy	16
2.2.2	Scanning Electron Microscopy	18
2.2.3	Energy Dispersive x-ray Spectroscopy	18
2.2.4	Transmission/Scanning Transmission Electron Microscopy	19
2.2.5	Photoluminescence Spectroscopy	19
2.2.6	X-ray Diffraction	21
2.3	Device fabrication and characterization	24
2.3.1	Device fabrication	24
2.3.2	Dark current density	25
2.3.3	Spectral response	26
3	T2SL material system and applications	28
3.1	Infrared detectors and applications	28
3.2	T2SL Ga containing structure	30
3.3	T2SL Ga free structure	32
4	Sb-based membrane transfer using single-step etch process	34
4.1	Wet and dry transfer process	34
4.2	Bonding between Sb-based membrane and - host substrate	40
4.3	Crystalline structure characterization	44

Contents

5	Sb-based membrane photodetector	56
5.1	Sb-based membrane transfer	57
5.2	Sb-based membrane optical characterization	58
5.3	Sb-based membrane photodetector fabrication	58
6	Sb-based membrane transfer using two-step etch process	65
6.1	Two-step etch transfer process	67
6.2	material characterization	69
6.3	Device fabrication and characterization	70
6.3.1	Fabrication	70
6.3.2	Characterizations	72
7	Future work	78
7.1	Conclusion	78
7.2	Future work	79
7.2.1	Wafer-level infrared photodetectors	80
7.2.2	Method I: Die to wafer integration	82
7.2.3	Method II: Die to wafer integration	83
7.3	Membrane metamaterial detectors	84
7.4	Strain engineering	88
7.5	Electrical transport characterization	90

List of Figures

1.1	Fundamental material study and technological problems of grown materials on GaSb conducting substrate and advantages of transferring Sb-based membrane to insulating substrates.	2
2.1	Research methodology	11
2.2	Strain distribution in multilayer structure after release	14
2.3	Section of a membrane undergoing spherical bending with a radius of curvature R	15
2.4	Photoluminescence setup schematic	20
2.5	X-rays diffraction through crystal lattices and the distance between atomic planes within the material	22
2.6	Spectral response setup	27
4.1	Wet and dry transfer process	35
4.2	T2SL transfer using Wet transfer process	38
4.3	T2SL transfer using dry transfer process	39
4.4	T2SL transfer using dry transfer process	40

List of Figures

4.5	Atomic force microscopy of the top and bottom surface of an InAs/InAsSb membrane.	41
4.6	EDS analysis of transferred pixels to PDMS	42
4.7	STEM across the bonded interface	43
4.8	(a) Co-planar diffraction pattern acquired around the (004) GaSb peak of the as-grown InAs/GaSb T2SL (Black solid circles). A fit to the experimental data is plotted as a red line. (b) Co-planar XRD pattern acquired from a transferred InAs/GaSb SL on a Si substrate (Black solid circles). The inset shows the layer structure obtained from the fit of the co-planar patterns, plotted as a red line.	46
4.9	In plane diffraction pattern by GI-XRD around the (220) reflection of the as-grown (circle-line pattern) and the transferred (triangle-line pattern) InAs/GaSb.	47
4.10	Co-planar diffraction pattern of the as-grown (a) and transferred (b) InAs/InAsSb SL membrane (Black solid circles). Both patterns are acquired around the GaSb (004) reflection. A fit to the experimental data is plotted as a red line in (a) and (b). The model layer structure obtained from fitting the co-planar patterns is shown in the inset, in (b). A slight discrepancy in the layer thickness deduced from simulations of the data in (a) and (b) is observed. The thickness within brackets is obtained from fitting diffraction patterns of the as-grown membrane.	48
4.11	The GI-XRD around two (220) reflections of the as-grown SL and one (220) reflection of the transferred multilayer stack.	50

List of Figures

4.12	E-k dispersion curve along (001) direction (a) as-grown InAs/GaSb, (b) transferred InAs/GaSb, (c) as-grown InAs/InAsSb and (d) transferred InAs/InAsSb.	54
5.1	Optical microscope and SEM images of transferred InAs/InAsSb pixels on Si/Ti/Au/Ti	58
5.2	A comparison of room-temperature PL spectra between unprocessed InAs/InAsSb on a GaSb substrate and transferred InAs/InAsSb membrane on Si/Ti/Au/Ti substrate.	59
5.3	Indium-bump-free single pixel photodetector process	60
5.4	current voltage characteristics of Indium-bump-free single pixel and conventional single pixel at 77 K.	61
5.5	Normalized zero bias spectral response measured at 77 K.	62
5.6	Bottom contact behavior	63
6.1	Sidewall of Ga free and Ga containing pixels after one-step etch release and transfer process	66
6.2	Sidewall of the InAs/GaSb pixel after one-step etch process	68
6.3	Two-step etch process	74
6.4	Material characterization after two-step etch process	75
6.5	Device characterization after two-step etch, release and process	76

List of Figures

6.6	Histogram of the dark current density vs. device number. Black lines represent the fabricated devices on growth substrate (GaSb), red lines represent the fabricated devices on transferred pixels on Si substrate using two-step etch and the fabricated devices on transferred pixels on Si substrate using one-step etch.	77
7.1	Wafer-level processing method I	83
7.2	Wafer-level processing method II	85
7.3	schematic of utilizing surface plasmon coupler on a photodetector. In this design, incident light excites the surface plasmon mode at the interface of the metal-semiconductor and couple the light to the detector laterally and enhance the signal	86
7.4	Schematic of metal and semiconductor interface and the electromagnetic field behavior at this interface.	87
7.5	Strain engineering of Sb-based heterostructures.	88
7.6	Strain in the textured host	90
7.7	Minimum, maximum and average strain in the InSb quantum well vs. a radius curvature varying between 0.1 and 5 μm	91
7.8	Fabricated and wirebonded 24x24 μm^2 pixel for Hall measurements .	92

List of Tables

4.1	In-plane lattice parameters deduced from GI-XRD and co-planar XRD for the InAs/GaSb and InA/InAsSb T2SL, both before and after transfer to bulk Si. Calculated values of in-plane strain in each layer of the SL are also reported along with the bulk lattice parameters per each constitutive material of the multilayer stack.	51
4.2	Layer thickness within the InAs/GaSb and the InAs/InAsSb SL, as expected from the epitaxial growth conditions. Mismatch strain, $\epsilon_{m,XRD}$, between adjacent layers in the as-grown T2SLs, as deduced from XRD. Biaxial modulus, $M=E/1-\nu$, with E, Youngs modulus and ν the Poissons ratio of the materials [1]. Residual in-plan straine as deduced from XRD, $\epsilon_{in-plane,XRD}$, and from continuum mechanics modeling, $\epsilon_{in-plane,CM}$	52

Chapter 1

Introduction

1.1 Background

Epitaxially grown single-crystalline semiconductor membranes offer a new platform for fundamental science and advanced technology. Progress in membrane fabrication has already significantly altered the landscape, as it relates to properties and applications of group IV [2, 3, 4, 5, 6] and III-V semiconductors, [3, 7, 8, 9, 10, 11, 12, 13, 14] III-nitrides [3, 15, 16] and various oxide materials. [16, 17, 18, 19, 20] Despite the numerous demonstrations of membrane technology applied to III-V materials, Sb-based compounds in membrane form has not been investigated. Furthermore, epitaxially grown Sb compounds have recently received increasing attention as functional layers in infrared detectors [21, 22, 23, 24] and sources, [25, 26, 27, 28, 29] high mobility transistors, [30, 31, 32] resonant tunneling diodes [33, 34, 35] and low-power analog and digital electronics.[30, 36]

In this work, I establish a versatile process to release and transfer these structures from their epitaxial growth substrate to any host substrate. The focus, specifically, will be on Sb-based type II superlattices (T2SLs) which are currently used as ab-

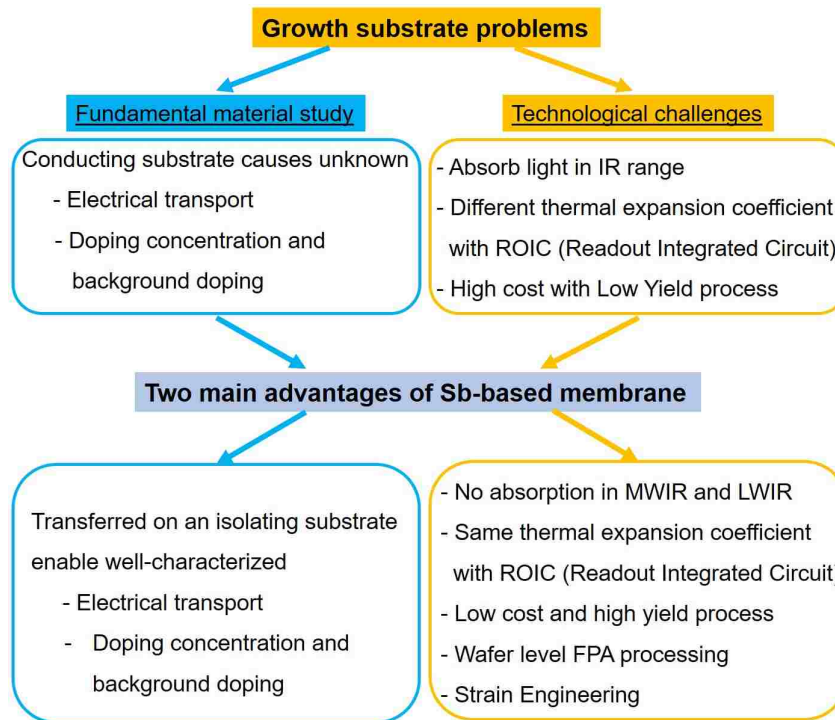


Figure 1.1: Fundamental material study and technological problems of grown materials on GaSb conducting substrate and advantages of transferring Sb-based membrane to insulating substrates.

sorbers in IR detectors. [21, 22, 23, 24] IR imagers will benefit from the release and transfer InAs/(In,Ga)Sb stacks from an epitaxial growth substrate to any host. Figure 1.1 summarizes the problems with GaSb substrate and the advantages of the Sb-based membrane. Furthermore, in the next two section, I will explain the challenges more in detail.

1.1.1 Fundamental material study

One major challenge is that fundamental properties of T2SL absorbers, such as background carrier concentration and vertical carrier mobility, have not yet been very well characterized. Background carrier concentration determines the minority carrier lifetime and diffusion lengths, whereas vertical and lateral carrier mobilities affect the extraction of the photo-generated electron-hole pairs. Electrical transport measurements in T2SLs are challenging due to the semiconducting nature of the native growth substrate, namely GaSb. Transfer of Sb-based T2SLs to insulating materials will enable a thorough investigation of electrical transport in the heterostructure via Hall and van Der Pauw measurements, which are not applicable to T2SLs supported by GaSb substrates. In addition to these fundamental questions, a number of technological challenges exist in the fabrication of IR detectors based on T2SLs.

1.1.2 Technological challenges

Typically, T2SLs are epitaxially grown on GaSb substrates. While these substrates provide mechanical support during device fabrication, they are undesirable in IR cameras. GaSb substrates absorb much of the incoming radiation in the IR range, thus reducing the signal-to-noise ratio (SNR). [37, 38] In addition, T2SLs/GaSb substrates are hybridized to a Si read-out integrated circuit (ROIC) to realize infrared focal plane arrays (FPAs). As the detectors-ROIC combination is cryogenically cooled down to 77 K for better performance, the large thermal mismatch between the GaSb substrate (7.75 ppm/°C at room temperature) and the Si ROIC (2.6 ppm/°C at room temperature) results in structural failure of the imaging device, via cracking of the absorber or delamination of the detectors from the ROIC. [39, 40] To overcome these issues, the GaSb substrate is routinely removed by chemical-mechanical pol-

Chapter 1. Introduction

ishing (CMP) [41] and selective etching, [42, 43] thereby increasing manufacturing costs, and decreasing yield by damaging either the detectors or the ROIC. Transfer of Sb-based SLs on Si will enable fabrication of IR detectors and ROICs on the same type substrate, which eliminates the large thermal mismatch between the GaSb and the Si substrate at low temperature. Si substrates have the additional advantage of being transparent to the incoming radiation, yielding a good SNR for T2SL-based detectors. Moreover, IR focal plane array detectors are realized using an expensive fabrication process, in which, part of the processing, including mesa delineation, surface passivation, metal deposition, and indium deposition is wafer-level on the host substrate. This process is followed by a die-level fabrication involving dicing, flip-chip bonding to a silicon read-out integrated circuit, substrate thinning/removal, and packaging.[44] The aforementioned die-level steps are low-yield processes[45] that dramatically increase the cost and fabrication time for the focal plane arrays. One of the reasons for the low cost of microbolometer detector arrays is that the entire fabrication and packaging is done at a wafer level.[46?] Thus Sb-based membranes potentially enable wafer-level processing of FPAs using a die-to-wafer or wafer-to-wafer bonding. Moreover, transferring Sb-based membranes to any substrate, including a flexible host, will pave the road to fabrication of flexible IR imagers.

An additional benefit of membrane technology applied to T2SLs is the possibility to engineer strain distributions, which are not obtainable within the limitations of epitaxial growth processes. For instance, a Sb-based structure will undergo elastic deformation during the release process, redistributing strain intrinsic to the deposition process between different layers in the SL. Furthermore, Sb-based compounds may be bonded and conformed to patterned surfaces of various shapes and sizes to induce local strain of different types and amplitudes. As strain modifies electronic band structure, electronic transport, optoelectronic properties, and phonon structure, one might harness it to obtain unique characteristics not present in the relaxed material.

1.2 Outline of dissertation

In dissertation I report my progress to develop a versatile release and transfer techniques including one-step etch and two-step etch processes, which enables integration of any Sb-based heterostructure on a variety of hosts, including Si, polydimethylsiloxane and metal coated substrates. This novel method of detector fabrication solves the fundamental and technical issues of the-state-of-the art in Sb-based photodetector and is also applicable for a wide range of materials. Utilizing this method enable wafer-level processing for Sb-based detectors and enormously reduce the cost and increase the yield in IR-detector technology.

Chapter 2 provides the detailed information about the theory and design of the heterostructures, including material design and strain engineering. Next, The material growth method, different fabrication steps and various analytical techniques which are used to evaluate the quality of the material before and after transfer is illustrated.

In Chapter 3 two different material systems for IR application are described. First system is InAs/GaSb type II superlattice (T2SL) or Ga containing and second is InAs/InAsSb type II superlattice or Ga free. More details about advantages and disadvantages of each system are discuss in the chapter.

Chapter 4 demonstrates a versatile release and transfer technique, which enables integration of any Sb-based heterostructure with a variety of hosts, including Si, polydimethylsiloxane and metal coated substratesincludes the wet and dry transfer of InAs/GaSb and InAs/InAsSb T2SLs using one-step etch process. Moreover, in this chapter, different material characterisation techniques which are used to show the crystalline structure of the membrane are not altered by the fabrication process, are explained. The chapter is wrapped with using mechanical modeling to show that the strain distributions in elastically relaxed membranes. Chapter 5 covers a

Chapter 1. Introduction

novel method which isolates Sb-based T2SLs in the form of free-standing membranes while releasing. In this process which includes two step of etch, both the top surface and the sidewalls of the membrane are coated with a hard-baked polymer film (i.e., photoresist), and therefore they are unexposed to the chemical etchant. Two-step etch technique is a very effective for Al and Ga containing structures. Since sacrificial layer also contains Al, the selectivity of the etchant is not high between active layer and sacrificial layer. Finally, devices are fabricated and characterized using two-step etch process and compared to the devices that transfer without isolation.

In Chapter 6, transfer and device fabrication on InAs/InAsSb (Ga free) T2SL is explained. Dark current and spectral response of the device has been measured and results compared to a single pixel device which is processed in a conventional method on growth substrate.

The thesis concludes in Chapter 7 with a summary and analysis of the work as well as considerations about future stages of this research.

1.3 Contributions of this work

1- For the first time, release and transfer of T2SL membrane from growth substrate to any host substrate is demonstrated.

2- Structural and optical properties of the materials before and after process is studied, using XRD, SEM, PL, EDS, XPS, TEM. This comprehensive study shows the crystalline structure of the membrane is not altered by the fabrication process, and a minimal elastic relaxation occurs during the release step, as demonstrated by X-ray diffraction and mechanical modeling. Further, In-bump free InAs/InAsSb IR photodetectors fabricated and characterized.

3- Mechanical modeling is utilized to show that the strain distributions in elas-

Chapter 1. Introduction

tically relaxed membranes can be controlled and optimized by tuning the relative thicknesses and elastic symmetry of the layers within the SL.

4- Two-step etch process for Al and Ga containing structures grown on Al compound sacrificial layers is developed. In those type of materials there were difficulties due to the low selectivity of the etchant between active and sacrificial layer.

1.4 Publications

My achievements in Sb-based membrane transfer project are published in:

Invention Disclosures

1- B. Klein, M. Zamiri, F. Cavallo and S. Krishna, "Two step etch for release and transfer of membranes", STC Ref No.2016-013, <http://stcunm.flintbox.com/public/project/29636/>

2- S. Krishna, F. Cavallo, M. Zamiri and B. Klein, "Mixed group-V sacrificial layers for release and transfer of membranes", STC Ref No.2016-011, <http://stcunm.flintbox.com/public/project/29635/>

3- S. Krishna, M. Zamiri, A. Kazemi, P. Zarkesh-Ha, C. Kadlec, B. Klein and F. Cavallo, "Wafer Level Gate Modulation Enhanced Detectors", STC Ref. No. 2016-079-01.

Patent Pending

1- S. Krishna, F. Cavallo, M. Zamiri and B. Klein, "Mixed group-V sacrificial layers for release and transfer of membranes.", US Patent, Docket No. 0023.0181-PCT.

Journal Papers

Chapter 1. Introduction

1- M. Zamiri, F. Anwhar, B. Klein, A. Rasoulof, T. Schuler-Sandy, N. Dawson, C. Deneke, S. Ferreira, F. Cavallo and S. Krishna, "Sb-based superlattice membrane for infrared applications." (PNAS)

2- M. Zamiri, B. Klein, V. Dahiya, S. Nezhadbadeh, F. Cavallo and S. Krishna, "Two-Step Etching for Release and Transfer of Type II Superlattice Membranes." (to be submitted to Applied Physics Letters)

3- M. Zamiri, B.Klein, T. Schuler, V. Dahiya, S. Myers, F. Cavallo, and S. Krishna, "Indium-bump-free Antimonide Superlattice Membrane Detectors on Silicon Substrat." Applied Physics Letters,108.9 (2016): 091110.

4- A. V. Barve, S. Sengupta, J. O. Kim, J. Montoya, B. Klein, M. A. Shirazi, M. Zamiri et al. "Barrier selection rules for quantum dots-in-a-well infrared photodetector", IEEE Journal ofQuantum Electronics, 48(10), (2012): 1243-1251.

5- A. Kazemi, M. Zamiri, J. O. Kim, T.SchulerSandy, and S. Krishna, "Colloidal and Epitaxial Quantum Dot Infrared Photodetectors: Growth, Performance, and Comparison" Wiley Encyclopedia of Electrical and Electronics Engineering. (2014): 1-26.

Conferences

1- M. Zamiri, F. Anwar, B. A. Klein, F. Cavallo, and S. Krishna, "Superlattice Nanomembrane for Potential Mid-Wave Infrared Applications", Oral presentation at 57th Electronic Material Conference, Ohio, June 2015.

2- M. Zamiri, B.Klein, T. Schuler, S. Myers, F. Cavallo, and S. Krishna, "In bump free Antimonide Superlattice Membrane Detectors on Silicon Substrate", Oral presentation at Defense, Security, and Sensing, Maryland, April 2016.

3- M. Zamiri, B. Klein, S. Nezhadbadeh, F. Cavallo and S. Krishna, "Two-Step Etching for Release and Transfer of Type II Superlattice Membranes", Oral presen-

Chapter 1. Introduction

tation at 58th Electronic Material Conference, Delaware (June 2016).

4- M. Zamiri, B. Klein, T. Schuler, S. Myers, F. Cavall oand S. Krishna, "Antimonide Superlattice Membrane Detectors on a Silicon Substrate", Poster presentation at 74th Device Research Conference, Delaware, June 2016.

5- B. Klein, M. Zamiri, F. Anwar, V. Dahiya, F. Cavallo, S. Krishna, "InAs/GaSb TYPE-II Superlattice Membrane Transfer for Doping Density Determination", Oral presentation, 31st North American Molecular Beam Epitaxy Conference, Mexico, October 2015.

6- M. Zamiri, E. Plis, J. O. Kim, S. C. Lee, A. Neumann, S. Myers, S. R. J. Brueck and S. Krishna, "MWIR superlattice detectors integrated with substrate side-illuminated plasmonic coupler", Oral presentation at Defense and Commercial Sensing, Maryland, April 2014.

7- A. Kazemi, M. Zamiri, F. Anwar, J. Ghasemi, T. G. Habteyes, F. Cavallo, S. Krishna, "Lateral transport in Graphene/Ge field effect transistor", Poster presentation at Material Research Society, Fall Meeting and Exhibit, Boston, December 2015.

8- J. Montoya, S. C. Lee, A. Barve, S. Myers, M. Zamiri, S. R. J. Brueck and S. Krishna, "Quantum Dot and Quantum Well Detectors with Plasmonic Resonators", Oral presentation at Quantum Structure Infrared Photodetector, France, June 2012.

Chapter 2

Materials and methods

This chapter describes the materials and methods used in the study of Sb-based superlattice membrane. Figure Fig. 2.1 exhibits the research methodology of my dissertation. This diagram includes three main parts. First step shows the theory and design of the heterostructure. In this project, I have used InAs/GaSb and InAs/InAsSb, two well-known Sb-based superlattice, membrane for transfer study and designed the sacrificial layer. Later, I have used mechanical model to calculate the strain distribution in elastically relaxed membrane with different thickness ratio of the layers. Second part is the material growth and characterization including growth method, various structural and optical techniques that are used in this work. Finally, the device fabrication flow and characterization setups are illustrated

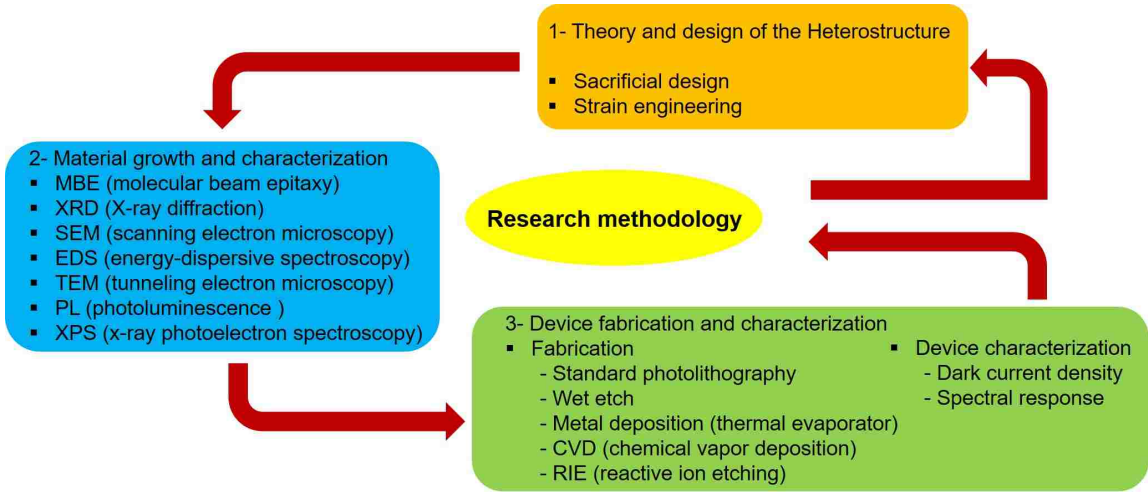


Figure 2.1: Research methodology

2.1 Theory and Design of Heterostructures

2.1.1 Material Design

Thickness and composition of the sacrificial layer were selected to satisfy three requirements: 1) sufficiently good etching selectivity between the sacrificial layer and the T2SL to enable release of the active layer; 2) pseudomorphic growth of the sacrificial layer on the selected growth substrate, namely GaSb; 3) sufficiently high thickness to enhance lateral access of the etching solution, resulting in a faster release process. In general, a sacrificial layer with a relatively high Al content are removed with a high selectivity compared to our selected active layers. In this work we used mixed group V digital alloy $\text{AlAs}_x\text{Sb}_{1-x}$ and ternary $\text{Al}_x\text{Ga}_{1-x}\text{Sb}$ as a sacrificial layer.

$\text{AlAs}_x\text{Sb}_{1-x}$ sacrificial layer

use of Mixed Group-V Sacrificial Layer(s) (MGV-SL) to enable the release and transfer of a large variety of III-V membranes on any substrates. In mixed group V digital

alloy $\text{AlAs}_x\text{Sb}_{1-x}$ sacrificial layer, there are stacks of very thin layers of AlAs (...ML) and AlSb (...ML) superlattice which enable to grow a fairly thick lattice matched sacrificial layer to the growth substrate (GaSb). Mixed group V sacrificial layer contains Al in both layers of the superlattice that enhance the etch rate of the layer.

$\text{Al}_x\text{Ga}_{1-x}\text{Sb}$ sacrificial layer

However, a high Al fraction in $\text{Al}_x\text{Ga}_{1-x}\text{Sb}$ results in an increasing lattice mismatch with the GaSb substrate, thereby reducing the critical thickness of the film. Based on the required characteristics of the sacrificial layer, we performed a growth study to determine the kinetic critical thickness of $\text{Al}_x\text{Ga}_{1-x}\text{Sb}$. For this purpose $\text{Al}_x\text{Ga}_{1-x}\text{Sb}$ of various thicknesses were grown onto GaSb substrates. As-grown samples were inspected by digital image contrast microscopy (DICM) to detect cross-hatching. To obtain a reasonable starting point for our experiment, we selected an Al fraction $x=0.4$, and we calculate the critical thickness of $\text{Al}_{0.4}\text{As}_{0.6}\text{Sb}$ on GaSb using the equation below [47]

$$h_c \sim \frac{a^2}{2(a_0 - a)} \quad (2.1)$$

where a and a_0 are the lattice constant of the $\text{Al}_{0.4}\text{Ga}_{0.6}\text{Sb}$ and the substrate, respectively. Our calculation yielded a starting thickness of 152 nm. Cross-hatching was observed by DICM on a 152 nm-thick $\text{Al}_{0.4}\text{As}_{0.6}\text{Sb}$ grown onto a GaSb substrate. The $\text{Al}_{0.4}\text{As}_{0.6}\text{Sb}$ thickness was reduced in 10 nm increments until cross-hatching was no longer visible. The maximum thickness of the $\text{Al}_{0.4}\text{As}_{0.6}\text{Sb}$ layer without causing cross-hatching was found to be 60 nm.

2.1.2 Strain Engineering

Strain in the released multilayer structures

Consider the heterostructure shown in Figure Fig. ???. Elastic strain sharing analysis can be extended to n-layer systems as long as the mismatch strain distribution at each interface and the elastic properties of each of the layers are known.[48, 49] The coherency conditions at the interfaces are

$$\begin{aligned}\varepsilon_{m1} &= \varepsilon_2 - \varepsilon_1 \\ \varepsilon_{m2} &= \varepsilon_3 - \varepsilon_1\end{aligned}\tag{2.2}$$

where ε_{mi} is the mismatch strain at a given interface and ε_i is the strain in that layer. If we assume perfect adhesion between the layers of the multilayer structure, ε_{mi} will be constant in the as-grown and transferred structure.

The in-plane residual strain in the released multilayer structure can be calculated using a force balance model. This model states at the equilibrium the sum of all mechanical forces in the system is zero

$$\sum_i F_i = \sum_i n_i M_i \varepsilon_i t_i = 0\tag{2.3}$$

where F_i is the mechanical force acting on the i-th layer of the multilayer, n_i is the number of the layer, M is the biaxial modulus, ε_i is the in-plane strain and t is the layer thickness.[48, 49]

For a trilayer, force equilibrium is [49]

$$n_1 M_1 \varepsilon_1 t_1 + n_2 M_2 \varepsilon_2 t_2 + n_3 M_3 \varepsilon_3 t_3 = 0\tag{2.4}$$

If we substitute the misfit strain in the above equation for a trilayer we will have

$$n_1 M_1 \varepsilon_1 t_1 + n_2 M_2 (\varepsilon_{m1} + \varepsilon_1) t_2 + n_3 M_3 (\varepsilon_{m2} + \varepsilon_1) t_3 = 0\tag{2.5}$$

Dividing the left side and the right side of the equation by $M_1 t_1$ we obtain

$$n_1 \varepsilon_1 + n_2 \frac{M_2}{M_1} (\varepsilon_{m1} + \varepsilon_1) \frac{t_2}{t_1} + n_3 \frac{M_3}{M_1} (\varepsilon_{m2} + \varepsilon_1) \frac{t_3}{t_1} = 0 \quad (2.6)$$

If we substitute $M_2/M_1 = \eta_1$, $M_3/M_1 = \eta_2$, $t_2/t_1 = \gamma_1$ and $t_3/t_1 = \gamma_2$ we have

$$n_1 \varepsilon_1 + n_2 \eta_1 (\varepsilon_{m1} + \varepsilon_1) \gamma_1 + n_3 \eta_2 (\varepsilon_{m2} + \varepsilon_1) \gamma_2 = 0 \quad (2.7)$$

By solving this equation, the residual strain in layer 1, ε_1 , is obtained.

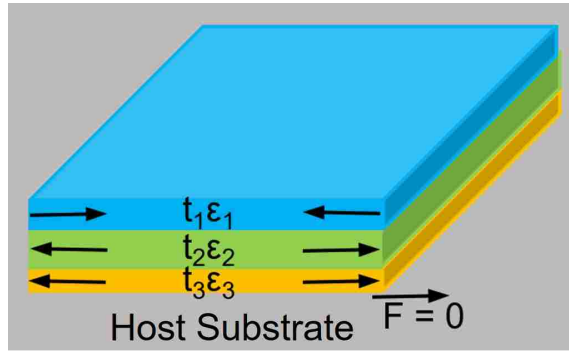


Figure 2.2: Strain distribution in multilayer structure after release

Strain in bent membrane

We use the continuum elasticity theory to calculate the residual strain due to bending in a quantum well or trilayer. Figure Fig. 2.3 shows the trilayer quantum well structure. It contains a quantum well layer (material B) with symmetric barrier layers (material A) on both sides.

In this model, we assume that all layers are perfectly bonded and no plastic deformation occurs while the film is curved in a defect-free sphere with inner radius R (see Figure Fig. 2.3). Local in-plane strain is obtained by

$$\varepsilon_{xx}^i = \varepsilon_{yy}^i = \frac{a_{xx}^i - a_{0,\text{bulk}}^u}{a_{0,\text{bulk}}^u} \quad (2.8)$$

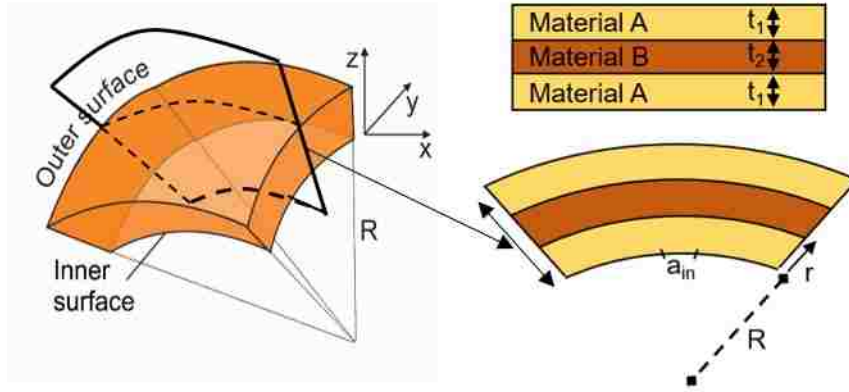


Figure 2.3: Section of a membrane undergoing spherical bending with a radius of curvature R .

where $a_{xx}^i = a_{in}(1 + z/R)$ is the local lattice constant at point z and a_{in} the inner lattice constant of the structure while it is curved in a defect-free sphere with inner radius R . The superscript i identifies the various layers within the heterostructures. The three strain components are related by the plane strain condition

$$\varepsilon_{zz}^i = -\frac{c_{12}^i}{c_{11}^i}(\varepsilon_{xx}^i + \varepsilon_{yy}^i) \quad (2.9)$$

and the strain energy density per each layer is

$$U^i = \frac{Y^i}{\nu^i + 1}(\varepsilon_{xx}^i{}^2 + \varepsilon_{yy}^i{}^2 + 2\nu^i \varepsilon_{xx}^i \varepsilon_{yy}^i) \quad (2.10)$$

The strain energy per unit area is obtained by integrating U^i over the layer thickness, t_i .

The total strain energy in a trilayer is calculated as

$$U_{\text{total}} = \sum_{i=1}^3 \int_0^{t_i} \frac{Y^i}{\nu^i + 1}(\varepsilon_t^i{}^2 + \varepsilon_l^i{}^2 + 2\nu^i \varepsilon_t^i \varepsilon_l^i) dz \quad (2.11)$$

The equilibrium strain state for the curved film is obtained from the solution of $dU_{\text{total}}/da_{in} = 0$.

Using the attained a_{in} from derivation, we calculate the 3 components of the across the thickness of the trilayer. Average strains are obtained by integrating the calculated strain distributions over the layer thickness.[2, 48, 50]

2.2 Material growth and characterization

2.2.1 Molecular Beam Epitaxy

Molecular beam epitaxy (MBE) is crystal growth technique for high quality materials. Over the last few decades MBE has evolved as one of the most prominent epitaxial growth methods for the synthesis of advanced high-quality semiconductor heterostructures. In fact, majority of most pioneering works on semiconductor heterostructures and devices has been realized by MBE due to its high level of growth control, high purity and feasibility of fabricating complex multilayer structures. [51] MBE takes place in high vacuum or ultra-high vacuum (10⁻⁸ - 10⁻¹² Torr). Shutters covering the sources allow the user to finely control the growth thickness atomic layer by layer. [52]

Multilayer structures including Sb-based superlattices (SLs) and AlGaSb sacrificial layers were grown in a VG-80 MBE reactor on n-type (Te-doped with $n \sim 5 \times 10^{17} \text{ cm}^{-3}$) epi-ready GaSb (0 0 1). The substrate is mounted on Mo plates and loaded into the machine through a load lock. Later, the substrate is transferred to the preparation chamber which is under UHV, where they are baked to remove any impurities such as water vapor. After the bake, the substrates are moved to the main growth chamber, which has heated III-V sources, As₂ and Sb₂ valved cracker sources. Once a substrate has been loaded into the growth chamber, it is heated while under group V flux to remove these oxides prior to growth. Indium and gallium growth rates were 0.5 ML/s for Ga (which corresponds to a beam equivalent

Chapter 2. Materials and methods

pressure (BEP) of 1.46×10^{-7} Torr) and 0.45 ML/s for In (which corresponds to a BEP of 1.46×10^{-7} Torr). Growth rates were determined by monitoring intensity oscillations in the reflected high-energy electron diffraction (RHEED) patterns. Group-V fluxes were adjusted using a conventional ion gauge to satisfy a group V/III BEP flux ratio equal to 7.5 and 3.8 for GaSb and InAs, respectively. The substrates were initially outgassed in vacuum, and the surface oxide was removed under Sb flux at 535 °C. The transition between the (1 3) and the (2 5) surface reconstruction on GaSb was observed by RHEED. The temperature corresponding to this transition was taken as a reference for all the growth temperatures. Four different active layers were grown for this work: 1) a 100 nm T2SL, which consisted of 17 periods of 8ML InAs/ 8ML GaSb; 2) a 1.6 μm InAs/GaSb SL including 237 periods of 8ML InAs/ 8ML GaSb; 3) a 2.5 μm InAs/InAsSb SL comprising 340 periods of 14ML InAs/12ML InAs_{0.81}Sb_{0.19}; 4) the p-i-n homojunction SL which consisted of 14ML InAs/12ML InAs_{0.81}Sb_{0.19}. The n-type layers (515 nm) were Te-doped to $2 \times 10^{18}\text{cm}^{-3}$, while the absorber (2060nm) and the p-type layers (158 nm) were Be-doped at $3 \times 10^{16}\text{cm}^{-3}$ and $2.1 \times 10^{18}\text{cm}^{-3}$, respectively. The InAs/GaSb T2SLs are grown as strain-compensated structures by inserting 0.75ML InSb at each InAsGaSb SLs interface. In addition, a Sb soak is at the InAs/GaSb interface to reduce materials interdiffusion. The InAs/InAsSb SL growth conditions were optimized with respect to the substrate temperature and As/Sb beam equivalent pressure (BEP) ratio. The results of this optimization process showed that a substrate temperature of 420 °C with an As/Sb BEP ratio of 8.4 resulted in the best optical and electrical quality SL material. The InAsSb digital alloy layer, composed of 1.7ML InAs0.3ML InSb, was grown by keeping the In shutter open and alternating the As and Sb shutters to provide the desired layer thicknesses.

2.2.2 Scanning Electron Microscopy

The scanning electron microscope (SEM) uses a focused beam of high-energy electrons to generate a variety of signals at the surface of solid specimens. The signals that derive from electron-sample interactions reveal information about the sample including external morphology (texture), chemical composition, and crystalline structure and orientation of materials making up the sample. In most applications, data are collected over a selected area of the surface of the sample, and a 2-dimensional image is generated that displays spatial variations in these properties. [53] Areas ranging from approximately 1 cm to 5 microns in width can be imaged in a scanning mode using conventional SEM techniques (magnification ranging from 20X to approximately 30,000X, spatial resolution of 50 to 100 nm). Precise measurement of very small features and objects down to 50 nm in size is also accomplished using the SEM. The SEM is also capable of performing analyses of selected point locations on the sample; this approach is especially useful in qualitatively or semi-quantitatively determining chemical compositions (using EDS), crystalline structure, and crystal orientations (using EBSD). [53] In this work, SEM images were taken by a JEOL 5800LV system in high vacuum mode using a secondary electrons (SE) detector. A cross-section of the InAs/InAsSb T2SL/bulk Si was prepared in a FEI Q3D ESEM/FIB dual-beam system with Ga ions source.

2.2.3 Energy Dispersive x-ray Spectroscopy

EDS is an analytical technique used for the elemental analysis or chemical characterization of a sample. It relies on an interaction of some source of X-ray excitation and a sample. Its characterization capabilities are due in large part to the fundamental principle that each element has a unique atomic structure allowing a unique set of peaks on its electromagnetic emission spectrum. [54] In this work chemical analy-

sis via energy dispersive x-ray spectroscopy (EDS) was accomplished on the JEOL 2010F in STEM mode. The measurement was performed using the X-MaxN 80T, 80 mm² detector (Oxford Instruments) with a resolution 50000 cps at 200 kV. Aztec software provides the power to acquire and process the EDS data.

2.2.4 Transmission/Scanning Transmission Electron Microscopy

A TEM can be modified into an STEM by the addition of a system that scans the beam across the sample to form the image, combined with suitable detectors. With it, the electrons pass through the specimen, but, as in scanning electron microscopy, the electron optics focus the beam into a narrow spot which is scanned over the sample in a raster. In this work, TEM characterization was performed in a JEOL 2010F high resolution TEM/Scanning-TEM with field emission e-beam accelerated at 200kV.

2.2.5 Photoluminescence Spectroscopy

Photoluminescence spectroscopy is a contactless, nondestructive method of probing the electronic structure of materials. Light with energy above the bandgap is directed onto a sample, where it is absorbed and imparts excess energy into the material in a process called photo-excitation. One way this excess energy can be dissipated by the sample is through the emission of light, or luminescence. In the case of photo-excitation, this luminescence is called photoluminescence.^[52]

Photo-excitation causes electrons within a material to move into permissible excited states. When these electrons return to their equilibrium states, the excess energy is released and may include the emission of light (a radiative process) or may not (a non-radiative process). The energy of the emitted light (photoluminescence)

Chapter 2. Materials and methods

relates to the difference in energy levels between the two electron states involved in the transition between the excited state and the equilibrium state. The quantity of the emitted light is related to the relative contribution of the radiative process.

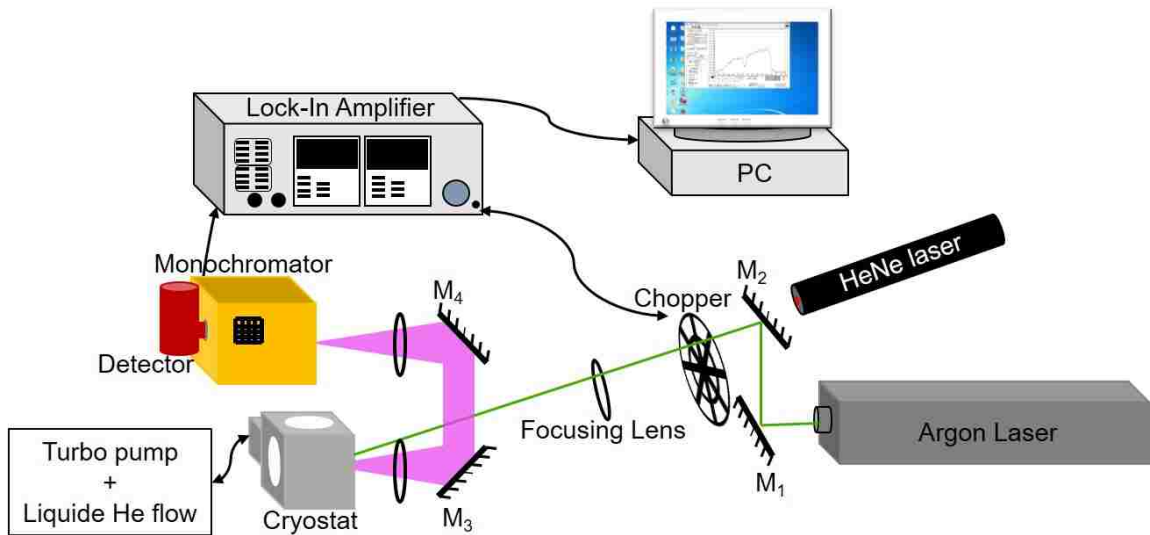


Figure 2.4: Photoluminescence setup schematic. In this setup, laser light is modulated by an optical chopper and focused on the sample using a focusing lens. In PL procedure, the emitted photon from the laser is absorbed by the sample, and then the sample re-emits photons at a wavelength corresponding to its bandgap. This emission from the sample gets collected and directed to a monochromator by series of lenses and mirrors. The monochromator has different grating for specific wavelength range. It scans through a requested wavelength range, and the intensity at each wavelength is measured by the detector. The detector signal and the frequency of the chopper are sent to the lock-in amplifier, which measures the intensity of signals only if they have the same frequency as the chopper. This intensity information is then sent to a computer which plots the PL intensity verses wavelength.[52]

In this work, Photoluminescence (PL) spectroscopy is conducted using a 1.5 W argon laser (514 nm) as excitation source that is directed through a chopper (spinning at 215 Hz) and is focused onto the sample. The emitted PL is collected using CaF₂ lenses and Al mirrors and focused into a monochromator with a grating optimized for a 2.6 - 6 μm wavelength range. The PL intensity was measured through an InSb detector (5.5 μm cut-off wavelength), positioned at the output of the monochromator. A schematic of the PL setup is shown in figure Fig. 2.4.

In this measurement, we modulate the incident laser light using chopper and expect that the detected sample emission by InSb detector has the sample frequency. The signal from detector is sent to the Lock-In amplifier which locks on to the frequency specified by the chopper. This signal data is then sent to a computer to be saved and plotted. In this setup, for low-temperature PL measurements, the sample is mounted in the cryostat, vacuumed to 10^{-7} Torr and cooled down. For room-temperature PL measurements a sample holder has been used to hold the sample in atmosphere pressure and room temperature.

2.2.6 X-ray Diffraction

XRD is one of the most important tool to characterize superlattices and other layered structures materials and gives a large amount of information related to the strain and crystalline quality of the structures.

Consider a crystalline material made up of atoms arranged in a pattern periodic in three dimensions. It has been shown that there is a clear relationship between the diffraction pattern that is observed when X-rays are diffracted through crystal lattices and the distance between atomic planes (the inter-planar spacing) within the material. By altering the inter-planar spacing different diffraction patterns will be obtained. Changing the wavelength of the X-ray beam will also result in a different

diffraction pattern. The inter-planar spacing of a material that is free from strain will produce a characteristic diffraction pattern for that material. The diffraction of X-rays by crystals is described by Bragg's Law, $n\lambda = 2d \sin\theta$

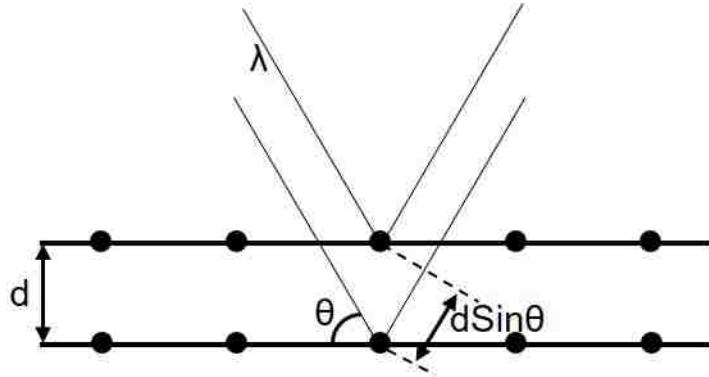


Figure 2.5: X-rays diffraction through crystal lattices and the distance between atomic planes within the material

When a material is strained, elongations and contractions are produced within the crystal lattice, which change the inter-planar spacing of the lattice planes. This induced change in d will cause a shift in the diffraction pattern. By precise measurement of this shift, the change in the inter-planar spacing can be evaluated and thus the strain within the material deduced.

Strains which cause a change in the Bragg angle for x-ray diffraction may be determined quantitatively from a plot of the diffracted x-ray intensity normalized to the incident x-ray intensity (the reflecting power) versus deviation of angle from the Bragg peak of an unstrained crystal.[55]

Each XRD spectrum has a peak for the substrate, in our case the GaSb, and a main or zeroth order peak for the superlattice. The amount by which the peak locations differ indicate the lattice mismatch and incidentally strain in the structure. The breadth of the main peak is an indicator of the roughness of the interfaces between each layer and thus the Full-Width-at Half-Maximum (FWHM) is often quoted

when describing the crystalline quality of a superlattice. Also, the XRD pattern for a superlattice sample includes several satellite peaks due to the numerous repeating period layers. The spacing between these peaks indicate the period spacing of the different layers which is useful to confirm growth conditions and layer thicknesses.[56] The amount of strain can be related to the initial dimensions of the body, and is defined as the strain, ϵ

$$\epsilon = \frac{a_1 - a_0}{a_0} \quad (2.12)$$

where a_1 and a_0 are the deformed and initial body lengths, respectively.

Grazing-incidence X-ray diffraction (GIXD) is a powerful method for probing crystalline structures in thin films. When an X-ray is incident onto a flat matter at a grazing angle, it is totally reflected since the refractive index of matter in the X-ray region is slightly less than unity. At this moment, an evanescent wave propagating parallel to the surface of the matter is generated. If there are diffracting planes perpendicular to the surface and they satisfy Bragg law with the evanescent wave, a diffracted X-ray emerges at a grazing angle nearly the same as the incident wave. Using this phenomenon, the in-plane crystalline order and the orientation distribution of the crystals can be probed.[57]

Co-planar and grazing-incidence X-ray diffraction (GI-XRD) measurements were carried out at the XDR beam line of the Brazilian Synchrotron Light Facility (LNLS) using a beam energy of 10 keV (wavelength $\lambda = 1.24093 \text{ \AA}$) with a 6-circle diffractometer. Sb-based SLs were investigated by XRD before and after transfer to a new host, namely Si. Co-planar measurements, were performed around the GaSb (004) reflection. GI-XRD measurements were performed with an incident angle of 0.2 at the (220) reflection. Diffraction patterns of the co-planar measurements were fitted by a commercial software package resulting in a structure based on the initial growth recipe.

2.3 Device fabrication and characterization

Following crystal growth of the device structures and material characterization, I processed the material into functional detectors and mounted onto chip carriers for characterization. For all type of materials two sets of device is fabricated. One set is transferred and fabricated on Si substrate and second set is fabricated on the growth substrate (GaSb). Finally, the performance of both sets are compared.

2.3.1 Device fabrication

Once grown, I have processed the material into detectors. This process involves the following steps, which are performed in the cleanroom. Standard photolithography is used to define the patterns in photoresist for every step. Detailed device fabrication process has been given in Chapters 4, 5 and 6.

Mesa etching

This is the first step, which involves inductively coupled plasma (ICP) etching for vertical sidewalls. The mesa etching for most of this work was done using BCl_3 gas in the ICP chamber. The sidewalls may be further smoothed by wet chemical etching using phosphoric acid based solutions to reduce the surface roughness.

Membrane transfer

Upon selective removal of the sacrificial layer layer via chemical etching, the membrane becomes freestanding, and it can be transferred to the alternative host using Polydimethylsiloxane (PDMS) or thermal release tape (TRT).

Passivation

Passivation is indispensable for T2SL photodiodes. Surface leakage current is a technological challenge in T2SL detector system. The sidewalls of the mesa can be protected with a number of passivation schemes as provided in (references). In this work, I used CVD method to deposit SiN_{xxx} passivation layer.

Contact metallization

For T2SL detectors, both P and N ohmic contacts are made with Ti/Pt/Au (500/500/3000Å). It is important to do a premetallization acid dip in (1:10) (HCl:H₂O) to remove native oxide. Afterwards, the sample should be cleaned and put in the metal evaporation chamber immediately.

2.3.2 Dark current density

The current that flows through the detectors in the absence of any photon flux is called the dark current. In T2SL detectors, major sources of dark current are minority carrier diffusion current, SRH current (G-R current), tunneling (trap assisted and band to band) current, and surface leakage current. Dark current data provides crucial information about the dominant dark current mechanism in the device.

Dark current data also provides crucial information about the dominant dark current mechanism in the device. Several studies on T2SL dark current has shown, the inverse of the dynamic resistancearea product (R_0A) at zero bias is a function of the perimeter-to-area ratio at 77 K. The surface dependence of (R_0A) can be approximated as

$$\frac{1}{R_0A} = \left(\frac{1}{R_0A}\right)_{\text{bulk}} + \left(\frac{1}{r_{\text{surface}}}\right)\frac{P}{A} \quad (2.13)$$

where $(R_0A)_{\text{bulk}}$ is the bulk R_0A contribution ($\omega \text{ cm}^2$), r_{surface} is the surface resistivity ($\omega \text{ cm}$), P is the diodes perimeter, and A is the diodes area. The slope of the function given by Eq. 2.13 is directly proportional to the surface-dependent leakage current of the diode.[58, 59]

In this work, the current-voltage characteristic of the photodetector were measured at 77 K by a JANIS ST-500 micro-manipulated probe station. The sample was placed in a 105Torr vacuum during electrical characterization. The probe station was equipped with a Scientific Instruments M9700 temperature controller, and the measurements are carried out with a Keithley 2400 source measure unit (SMU).

2.3.3 Spectral response

The spectral response is a very important characterization method for evaluating the performance of a photodetector. This characteristic defines the responsivity, specifies as the generated photocurrent per unit optical power, of the device along with the wavelength variation. The photodetector responsivity is primarily dependent on the device material, structure and the operating conditions in terms of bias voltage, temperature, and wavelength of the incident radiation. Hence, it is crucial to have a complete understanding of the effects of these parameters in order to design and fabricate an optimal photodetector.

Here, to acquire the spectral response or photocurrent spectrum of the fabricated infrared (IR) detector the light frequency of a broad spectrum IR light source (Hawk Eye IR-18), was modulated by a chopper and sent through a monochromator with an optimized grating for a 3-9 μm wavelength range. A JANIS JPF-100 cryostat was used to cool the detector to 77 K. The device is biased by a pre-amplifier with 103 gain and 0.01 V bias. A lock-in amplifier was used to measure the resulting electrical response of the device. Figure Fig. 2.6 shows the schematic of the explained setup.

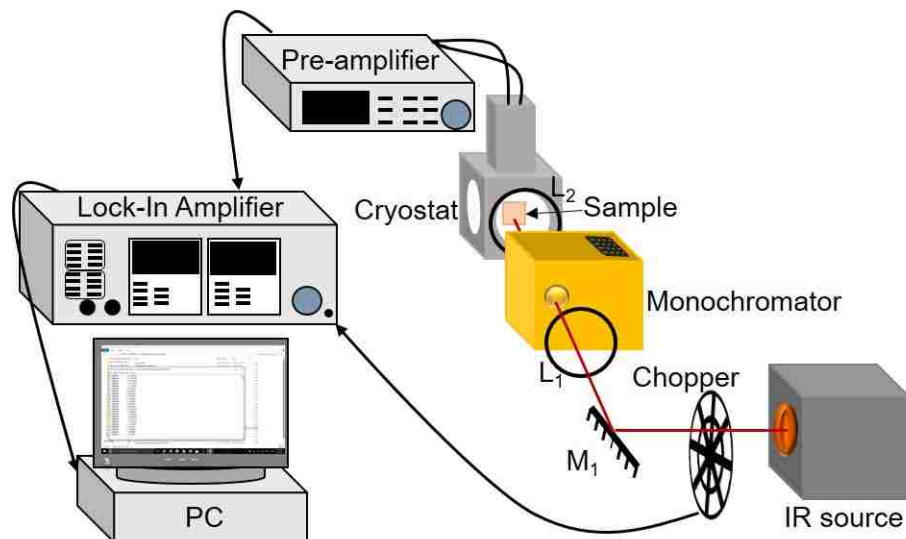


Figure 2.6: Spectral response setup schematic. In this setup, the light frequency of a broad spectrum IR light source is modulated by an optical chopper and sent through a monochromator with an optimized grating for a 3-9 μm wavelength range and focused on the sample using a focusing lens. A JANIS JPF-100 cryostat was used to cool the detector to 77 K. The device is biased by a pre-amplifier with 103 gain and 0.01 V bias. A lock-in amplifier was used to measure the resulting electrical response of the device.

Chapter 3

T2SL material system and applications

This chapter provides the foundation to understand InAs/GaSb type-II strained layer superlattices. Before diving into the details of IR detectors, a description of the electromagnetic spectrum is provided, detailing the different parts of the infrared range. This is followed by applications of infrared detectors, a discussion of the different sensing techniques, and types of infrared sensors. Finally, InAs/GaSb strained layer superlattices are discussed, including a brief history, its best performance metrics, and its advantages and challenges.

3.1 Infrared detectors and applications

Infrared detector technology includes two primary types, which are photon detectors and thermal detectors. Thermal detectors include Golay cells, thermopiles, and bolometers. Photon detectors are further divided into two categories namely photoconductors and photovoltaics. Each of these can be made of semiconductor materials,

Chapter 3. T2SL material system and applications

the most prominent being indium antimonide, mercury cadmium telluride, and gallium arsenide and aluminum arsenide based quantum well detectors.[60]

The infrared can be further segmented by atmospheric transmission windows, sections of the IR spectrum which are transmitted through earth's

atmosphere. The near-IR (0.75 μm - 1.4 μm), short-wave IR (1.4-3 μm), mid-wave IR (MWIR) (3-5 μm), long-wave IR (LWIR) (8-12 μm), and very-long wave IR (30 μm - 1mm). For example, the near- and short-wave IR is often used for fiber-optic communication, while MWIR and LWIR are of interest for infrared cameras. Humans beings also emit IR, with a peak intensity corresponding to approximately 9.2 μm . Thus, the ability to sense photons in the LWIR allows us to observe people in ways that would otherwise be indiscernible by cameras operating in the visible. There are numerous applications for IR detectors, including night vision, navigation, security and surveillance, atmospheric monitoring, and astronomy. IR detectors are used in multi-spectral imaging which allows monitoring of vegetation health or amount of water, from satellite views of the earth. The atmospheric composition can be monitored by IR sensors, search and rescue utilizes IR cameras to find missing people, and defects in fruit can be observed long before the fruit shows signs of decay in the visible wavelengths. Because IR detectors have so many uses, many different methods for sensing IR have been developed. Thermal IR detectors, such as thermometers, Golay cells, pyroelectric detectors, and Bolometers, operate by absorbing photons which heats up the detector and changes some measurable physical property of the detector[52]. Photon detectors work by incident photon interaction with electrons of numerous structures (bulk semiconductor, quantum well, quantum dot, quantum dot-in-well, and superlattices) and materials (InSb, HgCdTe, Si:X). Each of these IR detectors has its own drawbacks as well as advantages. Thermal detectors are much slower and less responsive than photon detectors, as it takes time for them to heat. Photon detectors, especially for MWIR and LWIR, often have to be cryogenically

cooled in order to operate. Rivalries between photon detectors also exist. HgCdTe and InSb are mature, dominant detector technologies for MWIR (InSb, HgCdTe) and LWIR (HgCdTe) applications, but are followed closely in device performance by younger technologies utilizing quantum confinement and heterostructure engineering. One such material, InAs/GaSb strained-layer superlattice (SLS) has the potential to beat the dominant technologies. Many of the optoelectronic devices we know today could not have been made without the realization of heterostructures. At their simplest, heterostructures are semiconductors made of two different materials joined together at an abrupt junction; this configuration consists two materials of dissimilar bandgap. A classic example is AlGaAs and GaAs, which forms the basis for one type of semiconductor laser. This concept of a heterostructure seems rather simple, yet was revolutionary at its inception. An abrupt transition from one semiconductor material to another offered superior control of junction location, which was unattainable with dopant atoms. Further, the refractive index was also abruptly changed with the heterojunction; not only could spatially abrupt junctions be formed, but also could be doubly used as waveguides. The concept of heterostructures paved the way for many new types of semiconductor materials, such as quantum wells, quantum wires, quantum dots, and superlattices.

3.2 T2SL Ga containing structure

The most common form of SLS is the InAs/Ga(In)Sb material system. In this material, thin layers of InAs and GaSb are alternated periodically to form a superlattice (SL). Since this material is grown on GaSb substrates, a thin InSb layer is often added to compensate for the strain induced by the InAs material. As noted before, the bandgap of the SL will be determined by the layer thicknesses. In a superlattice, the Brillouin zone splits into smaller minizones consisting of a series of allowed

Chapter 3. T2SL material system and applications

and forbidden energy bands.[61] This occurs due to the superlattice period being significantly thicker than the crystal lattice constant. The bandgap of a superlattice is determined by the separation between the upper edge of the valence band and the lower edge of the conduction band. This can be tuned over a range of 3m to 30m by changing the layer thicknesses, and thus the SL period, and the layer compositions.[62, 63, 64] The downside to this capability is that the optical absorption capabilities of the SL material are reduced as the layer thicknesses increase. This occurs due to the fact that absorption in an SL structure requires an overlap of electron and hole wavefunctions, which occurs primarily at the interfaces between the two materials. The overall effect is that the amount of absorption per period will be lower for SLs designed to operate at longer wavelengths.[64] A major benefit of the SLS material is that it suppresses interband tunneling and Auger recombination due to the strain inherent in the system. The Auger recombination can be further reduced through careful band engineering. Since the InAs-GaSb SL material has a larger electron effective mass ($0.04 m_0$) than bulk MCT, the tunneling currents are lower than those in MCT detectors with the same bandgap. Furthermore, the SLS is capable of producing better uniformity over the surface of a wafer as well as lower leakage currents. This indicates that it is possible for SL materials to improve on the performance demonstrated by their MCT counterparts. However, despite recent progress made in the growth and fabrication of SL materials[65, 66, 67, 68] and band structure engineering, SL materials have not yet sufficiently improved upon the performance of MCT detectors. The dark current present in InAs-GaSb SL systems is limited by G-R dark current attributed to the presence of Shockley-Read-Hall (SRH) centers in the material. These defects are currently associated with the GaSb layer, and have been theorized to be due to the large difference between optimal T2SL and GaSb growth conditions. It has been demonstrated that the SRH rate approaches a maximum when the energy level of the trap centers approach midgap.[69] Analysis of the formation energy of defects dependent on the location of the Fermi level stabi-

lization energy has demonstrated midgap defects can form in GaAs and GaSb due to the fact that the stabilized Fermi level is located near the valence band or midgap, but not in InAs, wherein the stabilized Fermi level is located above the conduction band edge.[?] This indicates that SRH recombination through midgap trap levels can occur in GaAs and GaSb, but not in InAs. Presuming this is true, the carrier lifetime in InAs should be greater than that in GaSb. This has been experimentally demonstrated in a study that found that the carrier lifetime decreased with increasing thickness of the GaSb layer. Further detail on carrier lifetimes in InAs-GaSb SL materials can be found in previous theses. The large difference between the carrier lifetimes in InAs and GaSb has motivated investigation into the InAs-InAsSb, or Gallium-free, SL material.[52, 56, 64]

3.3 T2SL Ga free structure

The InAs-InAsSb (or Ga-free) SL was developed initially for use in infrared lasers in the 1990s. These lasers were able to demonstrate continuous-wave (CW) operation, indicating some promise in the material. Initial structural characterization was performed via scanning tunneling microscopy (STM), and demonstrated mostly sharp interfaces between the two layers, with some intermixing occurring primarily on the boundary where InAs was grown on InAsSb. This incorporation is due to the intermixing of Sb into the surrounding InAs layers. The material was later proposed for use in IR detectors. The Ga-free SL has shown a type-IIb band alignment, which is the same alignment shown by the InAs-GaSb SL. The Ga-free SL has shown considerable potential as an IR detector material. This is due to the SRH carrier lifetime in this SL being considerably longer than that in the InAs/Ga(In)Sb SL. The length of the SRH lifetime is expected to result in a considerably lower G-R dark current level, and thus, presuming the Ga-free SL is G-R dominated, a lower overall dark

Chapter 3. T2SL material system and applications

current. This belief is reinforced by studies demonstrating that the Ga-free SL material shows good Auger suppression. Since many of the lifetime studies depend on photoluminescence measurement, the effect of AlSb barriers on the carrier lifetime in Ga-free SLs has been studied. Due to this, some groups have begun to develop Ga-free SL detector devices. Also, the bandgap range over which the superlattice can be tuned has been shown to be reasonably wide. Most research has focused on the creation of nBn devices, which have shown a very low dark current, but also a low quantum efficiency (QE) [56]. PIN structure devices show relatively high dark current, which isn't entirely unexpected due to the lack of a barrier, but have also shown a higher quantum efficiency in MWIR and VLWIR. More recent research has shown that a restoration etch may improve the dark current level in these devices. One two-color (MWIR/LWIR) nBn-based device has been demonstrated as well.[64]

Chapter 4

Sb-based membrane transfer using single-step etch process

4.1 Wet and dry transfer process

Fabrication of Sb-based membranes begins with molecular beam epitaxy of InAs/(InAs,Ga)Sb type II superlattices (T2SLs) on a 60 nm $\text{Al}_{0.4}\text{Ga}_{0.6}\text{Sb}$ sacrificial layer. Composition and thickness of the AlGaSb film are carefully selected to avoid any plastic deformation during epitaxial growth. As-grown membranes are released by selective removal of the $\text{Al}_{0.4}\text{Ga}_{0.6}\text{Sb}$ film in a diluted HF solution. Wet and dry transfer methods are utilized to transfer membrane with $1 \times 1 \text{ cm}^2$ and arrays of T2SLs with small lateral sizes ($\sim 24 \times 24 \mu\text{m}^2$) to a new host. Wet or dry transfer to a new host is used depending on the thickness and lateral size of the T2SL. Wet transfer is demonstrated for membranes with large area ($\sim 1 \times 1 \text{ cm}^2$) and thickness varying between 0.1 and 1.6 μm to a new host. In addition, arrays of T2SLs with small lateral sizes ($\sim 24 \times 24 \mu\text{m}^2$) are transferred from a GaSb substrate to alternative supporting materials using dry transfer method . Figure 4.1 (a)-(d) schematically

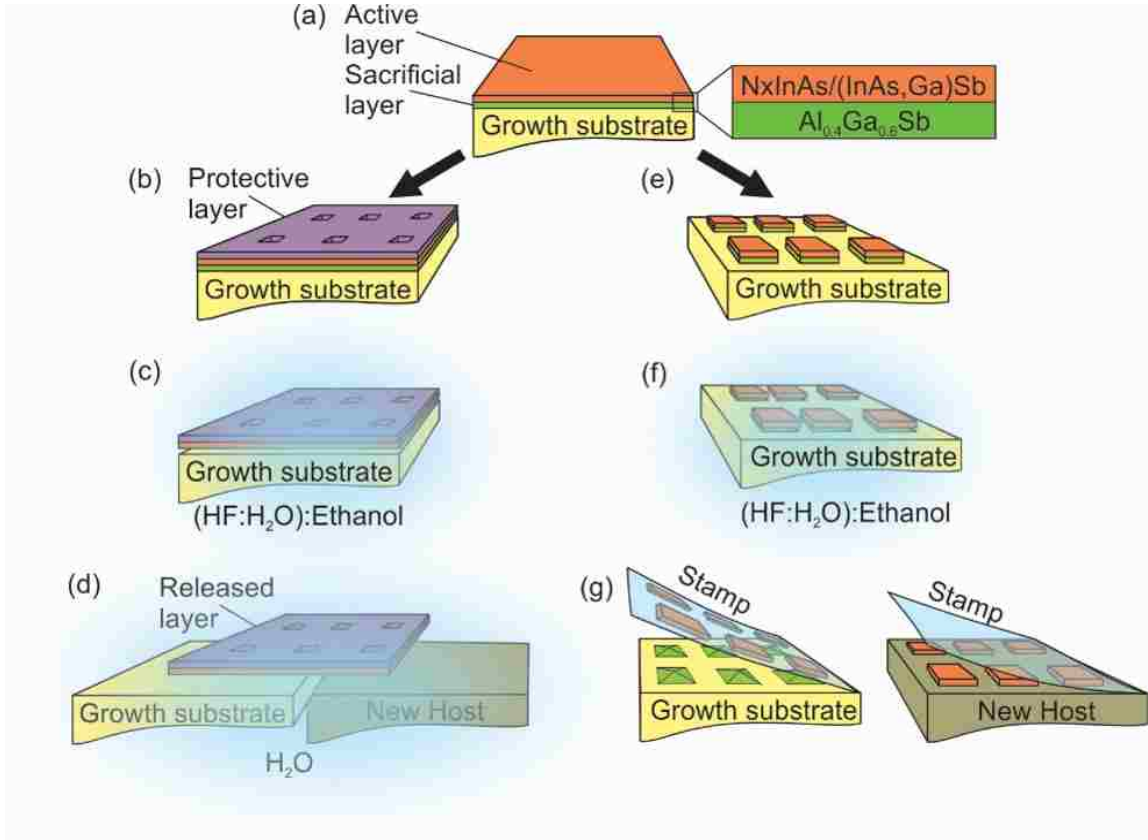


Figure 4.1: Schematic illustration of T2SL transfer from the original growth substrate to a new host using wet and dry techniques. (a) As-grown T2SL on a GaSb growth substrate coated with an $\text{Al}_{0.4}\text{Ga}_{0.6}\text{Sb}$ sacrificial layer. Wet transfer of T2SL is typically used for large area membranes, as illustrated in ((b)-(d)). Protective layer deposited on the T2SL (b). The protective coating/active layer stack is patterned with an array of holes to enhance access of the etchant to the sacrificial layer. Selective etching of the sacrificial in $[(\text{HF}:\text{H}_2\text{O})\text{:Ethanol}]$, resulting in the membrane to weakly bond-back to the native substrate (c). Freestanding membrane in de-ionized water upon debonding from the GaSb support, and membrane transfer to a new host (d). Dry transfer is typically used for 2D arrays of small-area membrane, as schematically depicted in (e)-(g). Unreleased membrane patterned into a 2D array of mesas via standard photolithography (e). Partial selective etch of the sacrificial layer in $[(\text{HF}:\text{H}_2\text{O})\text{:Ethanol}]$ (f). Removal of the mesas from the growth substrate and their transfer to the new support, using a stamp (g).

illustrate wet transfer of T2SLs to a receiving substrate. Prior to release, we coat the T2SL with a polymer or metal film to protect the active layer during selective etching of the $\text{Al}_{0.4}\text{Ga}_{0.6}\text{Sb}$. The need for a protective coating during this process is

Chapter 4. Sb-based membrane transfer using single-step etch process

related to the poor selectivity of the diluted HF solution between the InAs/GaSb SL and the $\text{Al}_{0.4}\text{Ga}_{0.6}\text{Sb}$ sacrificial layer. Two types of samples were fabricated for the wet etch study, referred to as samples A and B. Both samples had holes etched down through the epitaxy to enhance access of the etching solution to the $\text{Al}_{0.4}\text{Ga}_{0.6}\text{Sb}$ sacrificial layer, as shown in figure 4.1. The difference between samples A and B was that sample A had a protective coating of 5 nm of Ti/ 15 nm Au on its topmost layer, whereas sample B had a protective coating of photoresist. Both the protective top layers had holes directly aligned to the holes in the epitaxy. The protective layers doubled as mechanical support in subsequent processing steps. Sample A was fabricated in two lithography steps. First, squares were defined by standard lithography, followed by a blanket coating of Ti /Au, and this left a layer of Ti/Au with square holes. The second lithography protected the metal layer. Then, arrays of holes were dry etched through the T2SL using inductively couple plasma (ICP) with BCl_3 gas to promote access of the etching solution to the sacrificial layer and photoresist was removed after all. Sample B was fabricated in one lithography step, where only the image reversal of the square mask (as in Sample A), was applied, and the epitaxy was subsequently etched using BCl_3 ICP etching, through the epitaxy and down into the substrate. In both cases, the samples were intentionally over-etched all the way into the GaSb substrate ($\sim 2.1\mu\text{m}$ deep), so that the $\text{Al}_{0.4}\text{Ga}_{0.6}\text{Sb}$ sacrificial layer was exposed as a layer in the hole sidewall.

Releasing the membrane from the host substrate was accomplished by etching away the $\text{Al}_{0.4}\text{Ga}_{0.6}\text{Sb}$ sacrificial layer using a diluted HF and ethanol solution ($[(\text{HF}:\text{H}_2\text{O}) 1:700]:\text{ethanol } 1:5$). Samples with PR as a protective layer were released after 16 hours and samples with an Au layer for protection released after 6 hours. Au as protective layer offers metal assisted chemical etching (MacEtch), a simple directional wet etching method. MacEtch, is a wet etching method for semiconductors that can be anisotropic, assisted by a metal catalyst. The catalyst can be patterned metal films (Ag, Au, Pt, Pd, etc.). For samples A and B upon complete etching of

Chapter 4. Sb-based membrane transfer using single-step etch process

the sacrificial layer, the membrane will release from the substrate and either float off the substrate and up to the surface of the HF solution, or it may bond back onto the original GaSb substrate. In both cases, membrane and host substrate were transferred from the etching solution to a shallow beaker of DI water, where the transfer to a new host was performed. The surface preparation of the target substrate is essential for a successful transfer. A hydrophilic surface is preferred, and to ensure a hydrophilic target surface, both the Si and Au/Ti/Si substrates were cleaned with acetone and isopropanol, and then treated with oxygen plasma to form native oxide on the surface. To transfer the membrane to the target substrate, the substrate was dipped into the DI water beaker with the membrane, and the membrane adhered to it through capillary action.

InAs/InAsSb structure is another T2SL used as mid IR absorber as well. This structure was used for the dry transfer experiments, following the process illustrated in figure (1). In sample C, the T2SL was patterned in a 2D array of mesas with $24 \times 24 \mu\text{m}^2$ and $6 \mu\text{m}$ spacing were defined using positive resist (AZ4330), and ICP etched with BCl_3 . The final etch depth was $2.6 \mu\text{m}$, which is more than epilayer thickness, thereby allowing complete access to sacrificial layer. Then, the $\text{Al}_{0.4}\text{Ga}_{0.6}\text{Sb}$ sacrificial layer was partially etched in diluted HF and ethanol solution ($[(\text{HF}:\text{H}_2\text{O}) 1:700]: \text{ethanol } 1:5$), the same solution used to etch samples A and B for wet transfer. After 4 and a half hour, sample was rinsed in water and dried with nitrogen. The pixels were peeled off from GaSb substrate using both, Polydimethylsiloxane PDMS stamp and thermal tape. The PDMS was prepared by 1) mixing 10 parts of the PDMS base with 1 part of the PDMS curing agent, 2) curing the mixture on a hotplate at 85°C for 4 hours, 3) cleaning the surface in toluene for ~ 30 min, and 4) drying the PDMS on top of a 50°C hot plate for approximately 2 hours. The last step of dry transfer with PDMS is to print the mesas from PDMS to the new host substrate, which is cleaned with acetone, IPA, and water, and performing an oxygen plasma treatment with 100 watt power and 0.100 Torr pressure for 2 minutes.

This can be achieved by placing the PDMS/T2SL in contact with the new substrate (see figure 4.1) and slowly peeling off the PDMS stamp with a constant speed from the new host. Next transfer was with heat release single side tape, semiconductor equipment corp product, pixels were peeled off from GaSb substrate as well. Then tape and new substrate which was cleaned using the same way as PDMS transfer, attached together and heated up to 90 to 110 , after 20 seconds tape color turned into white and transferred happened. We demonstrate transfer of T2SL membranes with different in-plane geometry, thickness and layer structure. Figure 4.2 (a)-(c) shows a schematic cross-sectional view and scanning electron micrographs (SEMs) of 100 nm-thick InAs/GaSb T2SLs after release and wet transfer to a Si substrate. Figure 4.2(d) is an SEM of a partially released membrane, which is still coated with a

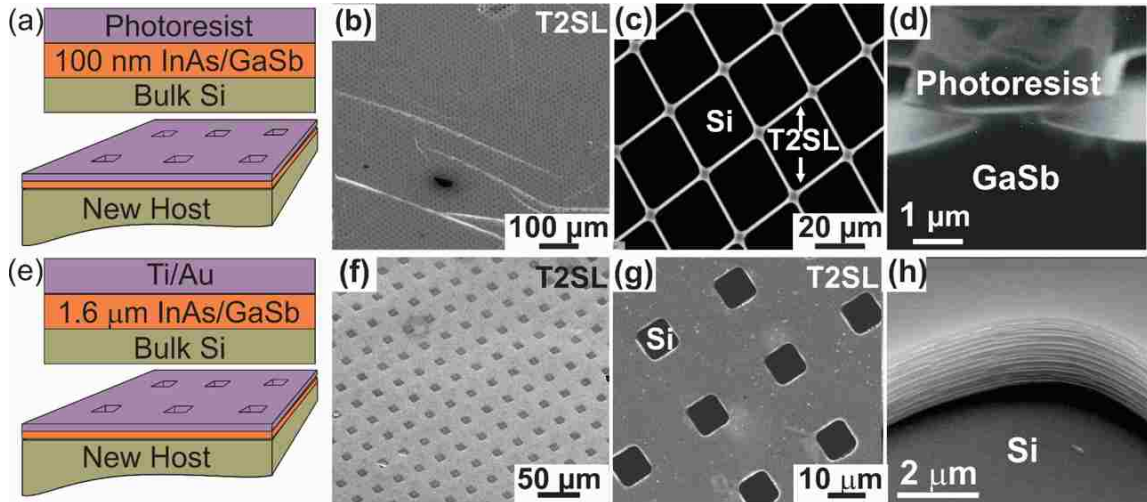


Figure 4.2: Schematic cross-sectional views and SEM of transferred T2SL transferred to various substrates. Cross-section (a) and top-view SEM (b)-(c) of a 100 nm-thick InAs/GaSb T2SL with two different in-plane patterns transferred to a Si substrate. Photoresist serves as a protective coating during membrane release. (d) is an off-axis SEM of a partially released 100 nm InAs/GaSb T2SL bonded to native growth substrate and coated with photoresist. Layer structure (e) and SEM images (f)-(g) of a 1.6 μm -thick InAs/GaSb SL membrane bonded to bulk Si. A Ti/Au film hinders etching of the active layer as removal of the sacrificial layer occurs. (h) is on off-axis SEM of the membrane side-wall, showing that a minimal lateral etching of the GaSb layer occurs during release of the InAs/GaSb SL membrane.

photoresist protective layer. A 1.6 μm -thick membrane with identical layer structure is transferred to bulk Si using a Ti/Au coating as protective layer (see Figure 4.2 (e)-(h)). Figure 4.2 (h) is a high magnification SEM showing that a minimal lateral etching occurs at the membrane sidewalls. We achieve release and dry transfer of 2.5

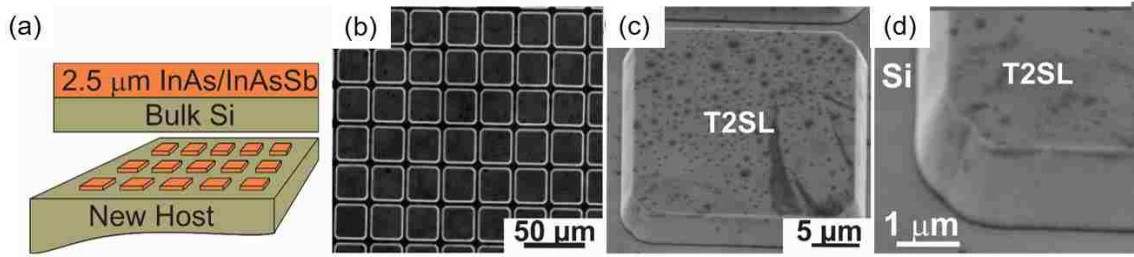


Figure 4.3: Schematic (a) of a 2.5 μm -thick InAs/InAsSb T2SL after release and dry transfer to a Si substrate. (b) Top-view SEM of a 2D array of pixels on bulk Si. (c) Off-axis SEM of a single pixel. Dry transfer of the mesas is mediated by thermal release tape. Tape residues are visible on the surface of the pixel. (d) is a high magnification SEM of the smooth membrane sidewall, showing that no lateral etching of the T2SL occurs during the release step.

μm -thick InAs/InAsSb T2SL patterned in a 2D array of $24 \times 24 \mu\text{m}^2$ mesas or pixels. Figure 4.3 (a)-(b) show a cross-sectional view of the transferred membrane and a SEM of pixels bonded to bulk Si, respectively. Figure 4.3 (c) is a high magnification and off-axis SEM of a single pixel. The transferred membrane exhibits smooth sidewalls (see Figure 4.3(d)) thereby confirming the excellent selectivity of the etching solution between InAs/InAsSb and the sacrificial layer.

A successful release and dry transfer of membranes requires a tight control on the etching time of the sacrificial layer. Indeed, if dry transfer is performed before membranes are completely released, the undercut portion will peel off and the rest of the pixel will stay on the native substrate, yielding transferred pixels with holes in the center (see Figure 4.4). On the other hand, if pixels are transferred long after the undercut is complete, the pixels may have shifted or be released from the substrate surface, resulting in misaligned or missing pixels after transfer to the new substrate

(see Figure 4.4). A successful dry transfer is achieved by peeling off membranes from the native substrates just before complete etching of the sacrificial layer.

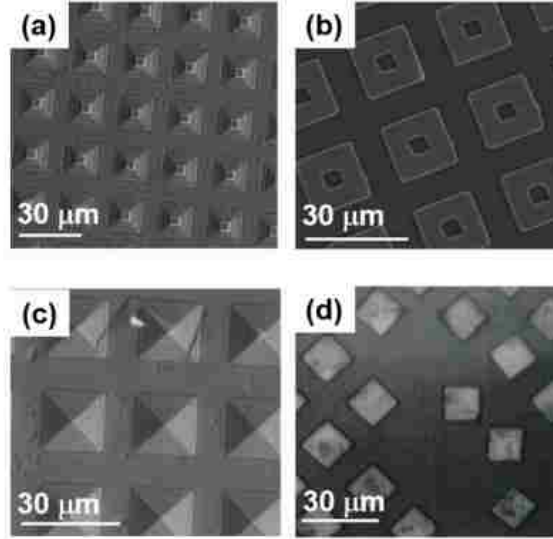


Figure 4.4: Top-view images of native substrates (a)-(c) and new host (b)-(d) after release and transfer of a 2.5 μm -thick InAs/InAsSb T2SL. (a)-(b) are SEM and (c)-(d) are bright field optical images. The native substrate and the new host are bulk GaSb and bulk Si, respectively. The sacrificial layer is 60 nm $\text{Al}_{0.4}\text{Ga}_{0.6}\text{Sb}$. Etching time in diluted HF (see Methods) was 3 hours in (a)-(b) and 5.5 hours in (c)-(d).

4.2 Bonding between Sb-based membrane and - host substrate

Residual $\text{Al}_{0.4}\text{Ga}_{0.6}\text{Sb}$ may result in an increased roughness of the membrane back-side, thereby promoting a weak bond between the membrane and the new substrate. Transfer of membranes on metal-coated substrates may also be used to provide the T2SL with electrical contacts via interface bonding. In this scenario, a residual $\text{Al}_{0.4}\text{Ga}_{0.6}\text{Sb}$ will drastically increase the resistance of the contact. To confirm that the selective etching step completely removes the sacrificial layer, we did a series

of experiments, i.e. atomic force microscopy (AFM), energy dispersive spectroscopy (EDS) and scanning transmission microscopy (STEM). We compare the surface topography of the top and bottom surface of the released membrane using AFM. The EDS analytical technique is performed on the backside of the pixels for elemental analysis to verify the absence of the sacrificial on the membrane layer after peeling off from the growth substrate. Further, STEM and EDS show no air gap at the interface of the transferred pixel and new substrate. Figure 4.5 schematically illustrate the

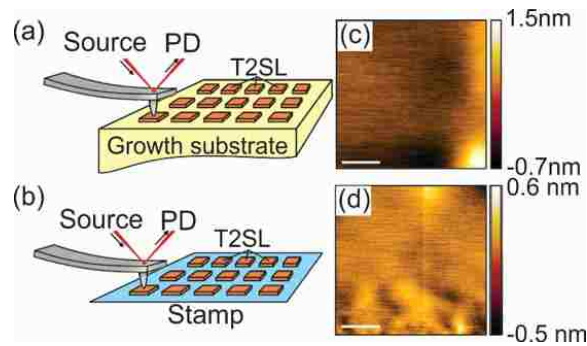


Figure 4.5: Atomic force microscopy of the top (a)-(c) and bottom (b)-(d) surface of an InAs/InAsSb membrane. (a)-(b) Schematic illustration of AFM. (c)-(d) Surface topography as measured over a $1 \times 1 \mu\text{m}^2$ area. We access the bottom surface of the membrane while it is bonded on PDMS, during a dry transfer process. The comparable values of RMS roughness measured in (c) and (d) suggest that the $\text{Al}_{0.4}\text{Ga}_{0.6}\text{Sb}$ has been completely removed by the diluted HF solution, during the release step.

measured areas . We gain access to the backside of the membrane by measuring the InAs/InAsSb SL supported by a polydimethylsiloxane (PDMS) stamp (see Figure 4.5). The PDMS is used to peel the T2SL from the growth substrate after partial release of the film has occurred, thereby leaving the bottom surface exposed. Figure 4.5 show 2D AFM images acquired over $1 \times 1 \mu\text{m}^2$ areas on the front and backside of the T2SL. Atomic force microscopy is performed on an Asylum MFP-3D system in tapping mode. Scans are acquired using NSC15 cantilevers (MikroMasch) with a tip radius of 8 nm and a spring constant of 40N/m. AFM data is analyzed by Gwyddion software. We calculate a root-mean-square (RMS) roughness of 0.112 nm and 0.118

nm from the images in Figure 4.5 (c) and (d), respectively. The comparable RMS roughness of the top and bottom surfaces of the T2SL suggests that the $\text{Al}_{0.4}\text{Ga}_{0.6}\text{Sb}$ has been completely removed by the diluted HF solution, during the release step.

In the AlGaSb sacrificial layer, Al and Ga, the prime components of the layer which are not used in InAs/InAsSb T2SL active region. EDS which is an x-ray technique has been used to identify the elemental composition of the transferred pixels. Since x-ray has a finite penetration depth and it may not go thoroughly to the bottom layer of the transferred pixels, we analyze the transferred pixels onto PDMS or tape, which are bottom-up to ensure one that x-ray senses the layer which is in contact with sacrificial layer. This way of measurement definitely shows the sacrificial layer residual. Figure 4.6 shows the schematic of the measured area. The elemental counts shows no Al or Ga which confirms that no residue of the AlGaSb layer is on the transferred pixels before transferring to the new substrate. we perform scanning

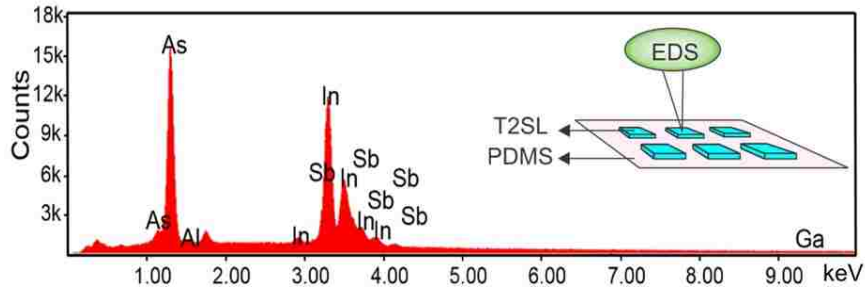


Figure 4.6: EDS analysis of transferred pixels to PDMS

transmission electron microscopy (STEM) and Energy dispersion X-ray spectroscopy (EDS) to investigate the chemical composition and the structural quality of a 2.5 μm -thick InAs/InAsSb T2SL bonded to Si. Prior to membrane transfer, Si is coated with a Ti/Au/Ti film. The T2SL is patterned in a $24 \times 24 \mu\text{m}^2$ pixel prior to release and dry transfer to the new host. Milling by a focused ion beam is used to obtain a thin lamella across the T2SL/Si interface (see Figure 4.7(a)-(b)). Remarkably, figure 4.7(a)-(b) rule out the presence of voids or particles at the membrane/host interface,

by showing a continuous interface bond. Figure 4.7(c) is a scanning transmission

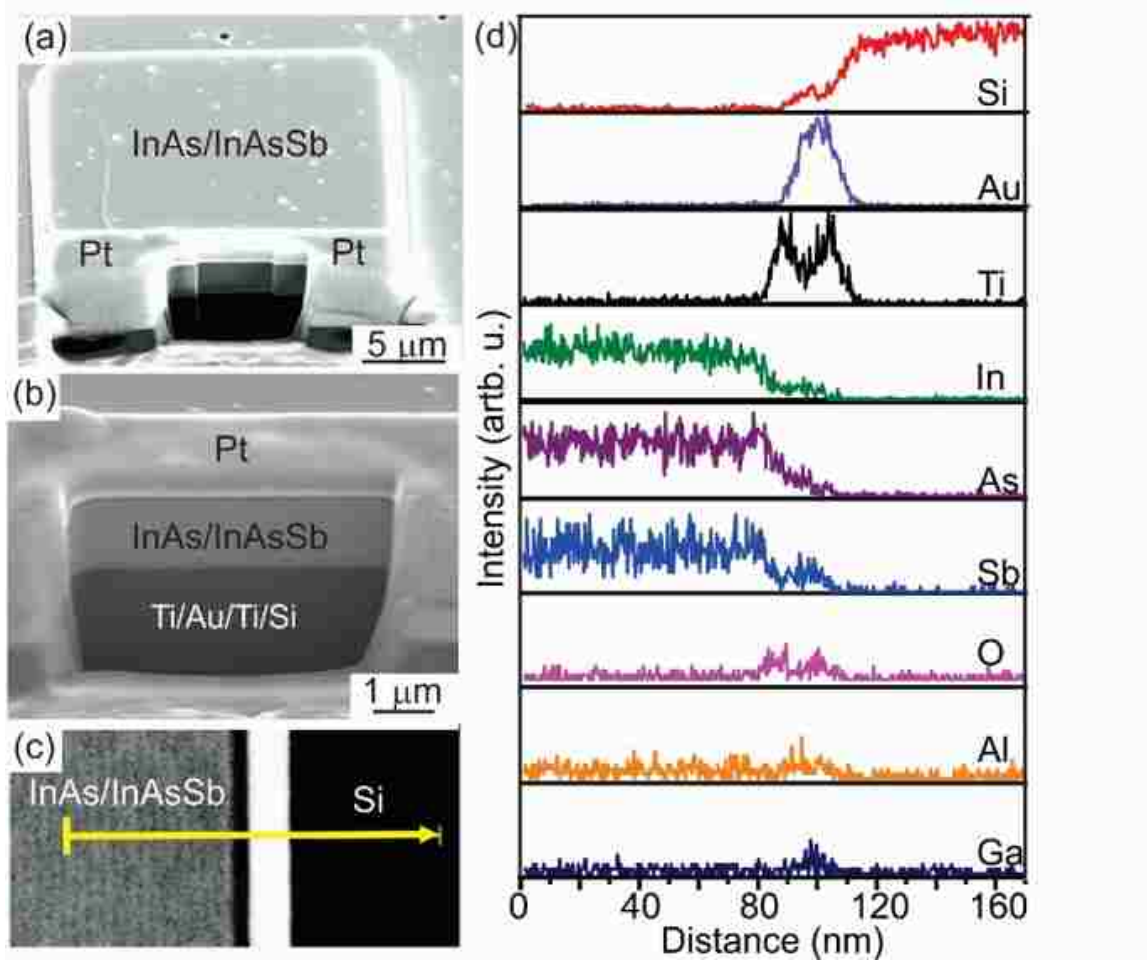


Figure 4.7: Structural characterization of the bonded interface between a 2.5 μm -thick InAs/InAsSb SL and a metal-coated Si substrate. (a)-(b) Off-axis SEM image of an InAs/GaSb SL mesa transferred to a metal coated Si substrate. The visible cross-section across the bonded interface is obtained by FIB. Remarkably (a) and (b) show a continuous bond between the membrane and the new host. (c) High-angle annular dark field STEM across the bonded interface. The material contrast allows identifying the T2SL, as well as the Ti/Au bilayer deposited on Si prior to membrane transfer. (d) Elements concentration profiles obtained by EDS in the direction marked by the white arrow, in (c).

electron microscopy (STEM) image of the T2SL/substrate interface, where the material contrast allows identifying the multilayered structure of the SL and the metal coated substrate. The yellow line marks the path of the EDS chemical analysis, and

the arrow indicates the direction of the performed line scan. The concentration of Ga, Sb, In, As, O, Ti, Au, and Si are extracted from the energy dispersive spectra and displayed in Figure 4.7 (d). The magnitudes of each elemental profile are normalized to the values obtained for Si. The intensity modulation of the STEM image allows accurate correlation with the EDS scans through the interface. In, As, and Sb show an oscillating profile over the T2SL. The Au signal correlates with the bright region in Figure 4.7 (c), and the Ti has a bimodal peaking between the Au and the SL, and between the Au and the Si signal.

4.3 Crystalline structure characterization

As demonstrated in figure 4.2 and 4.3, we have established a successful process to release and transfer T2SL membranes onto any host substrate. As transfer occurs through release of the membrane into a fluid, there is no resistance to strain relaxation, and elastic strain transfers between the various layers in the SL. Furthermore, global and local bending of the membrane typically occurs during release and transfer. Strain redistribution among the layers may affect the electronic structure of the SL (*e.g.*, change the intra-band energy gap). In addition, strain induced by bending or wrinkling can dramatically reduce the critical thickness of each layer for dislocation formation. All of these phenomena will significantly affect the performance of any device embedding T2SLs or any Sb-containing heterostructure. Based on these considerations, as-grown and transferred membranes undergo co-planar (out-of-plane) and grazing-incidence (GI) XRD to evaluate the effect of the release and transfer process on the crystalline quality and strain state of the membranes. Both InAs/GaSb and InAs/InAsSb membranes are investigated. In this study as-grown and transferred membranes undergo co-planar (out-of-plane) and grazing-incidence (GI) XRD. Both InAs/GaSb and InAs/InAsSb membranes are investigated. GI-

XRD measurements at the (220) reflection allow determining the in-plane lattice parameter ($a_{\text{in-plane}}$) of the membrane before and after transfer to a new host. Coplanar measurements around the GaSb (004) reflection are fitted by a commercial software package to obtain the structure of the as-grown and transferred multilayer stacks. We calculate the in-plane strain as $a_{\text{in-plane}} = (a_{\text{in-plane}} - a_{\text{bulk}}) / a_{\text{bulk}}$, where a_{bulk} is the lattice parameter of the relaxed material. The calculated in-plane strains yield the strain distribution among the various layers of the SL membrane, before and after transfer to bulk Si. A comparative analysis of the coplanar patterns measured for the as-grown and transferred membranes determines the effect of the release and transfer process on the crystalline quality of the SL. Figure 4.8(a) shows the out-of-plane XRD pattern acquired from the as-grown AlGaSb/InAs/GaSb multilayer stack on a GaSb substrate. A thin InSb is grown at the GaSb/InAs interfaces to achieve a strain-balanced heterostructure. The investigated InAs/GaSb T2SL is nominally 1.6 μm -thick. The solid circles represent the experimental data acquired around the GaSb (004). The pattern is dominated by the substrate peak at a Bragg angle of 24.005° and by the 0th order peak of the SL structure at 24.026° . We identify SL fringes up to the 4th order, and a shoulder (at lower Bragg angles than the substrate peak) that we ascribe to the contribution of the $\text{Al}_{0.4}\text{Ga}_{0.6}\text{Sb}$ sacrificial layer. The sharp SL fringes as well as the relatively high intensity of the 0th order reflection compared to the substrate peak, demonstrate the high epitaxial quality of the as-grown structure. Fig. 4.9 depicts the obtained GI-XRD reflection for the as-grown (line-circles pattern) and the transferred (line-triangles pattern) T2SL. The two patterns correspond to two perpendicular (220) directions. We observe a single peak for the as-grown and transferred membranes, signifying that both structures are characterized by a single in-plane lattice parameter, *i.e.*, they are pseudomorphic epitaxial layer stacks. The peaks acquired from the as-grown membrane are centered at the angle corresponding to the GaSb lattice parameter ($a_{\text{GaSb,bulk}} = 6.0959 \text{ \AA}$). The two patterns acquired from the transferred sample exhibit both broadening and a shift

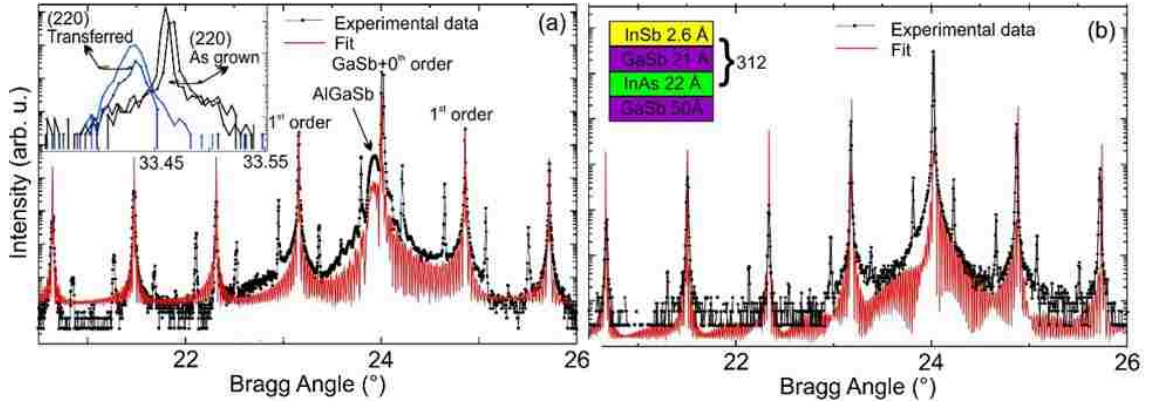


Figure 4.8: (a) Co-planar diffraction pattern acquired around the (004) GaSb peak of the as-grown InAs/GaSb T2SL (Black solid circles). A fit to the experimental data is plotted as a red line. (b) Co-planar XRD pattern acquired from a transferred InAs/GaSb SL on a Si substrate (Black solid circles). The inset shows the layer structure obtained from the fit of the co-planar patterns, plotted as a red line.

to 33.428° indicating a relaxation of the lattice during the transfer. The calculated in-plane lattice parameter for the transferred membrane is $6.10177 \pm 0.0052 \text{ \AA}$, *i.e.*, 0.096% bigger than the initial GaSb lattice parameter. To deduce the various layer thicknesses for the as-grown multilayer, we fit the experimental data in Fig. 4.8 (a) with a calculated pattern from a model structure (red line). For this purpose, we use a generic optimization algorithm. The model assumes a pseudomorphic heterostructure to the GaSb substrate. We extract the following structural parameters for the as-grown multilayer: 50 nm $\text{Al}_{0.3}\text{Ga}_{0.7}\text{Sb}$ / 5 nm GaSb followed by a 312 period SL of 2.16 nm InAs/2.14 nm GaSb/0.26 nm InSb. The layer structure calculated from analysis of the co-planar XRD scans agrees with the one expected from the utilized growth conditions. The resulting fit demonstrates that the whole stack is pseudomorphic to the GaSb substrate. We observe additional satellite peaks in the experimental data that we ascribe to multi-diffraction effects.

Figure 4.8(b) shows the co-planar diffraction pattern of the transferred membrane (black solid circles). The pattern is dominated by the 0th order peak of the

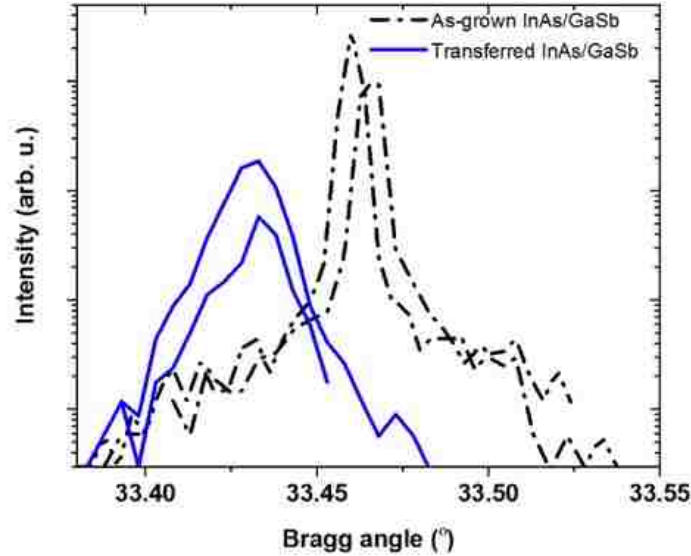


Figure 4.9: In plane diffraction pattern by GI-XRD around the (220) reflection of the as-grown (circle-line pattern) and the transferred (triangle-line pattern) InAs/GaSb.

transferred structure now found at 24.019° . A careful inspection reveals a small systematic shift in the higher order superlattice fringes compared to the diffraction pattern acquired from the as-grown sample (see Fig. 4.8(a)). It is worth pointing out that the substrate peak and the typical shoulder of the AlGaSb layer have vanished as the membrane has been transferred to a new host substrate. Interestingly, we still observe the additional satellite peaks ascribed to multi-diffraction effects of the T2SL suggesting that release and transfer does not degrade the crystalline quality of the film. We calculate the expected diffraction pattern for the transferred membrane (red curve) and compare it to the measured data. In this analysis we use the layer thickness obtained from fitting the co-planar scans of the as-grown samples as well as the in-plane lattice parameter deduced from the GI-XRD scans ($a_{\text{in-plane}}=6.10177 \text{ \AA}$). Figure 4.8(b) shows that such fitting procedure produces a curve in good agreement with the experimental data. These results confirm both the structural model

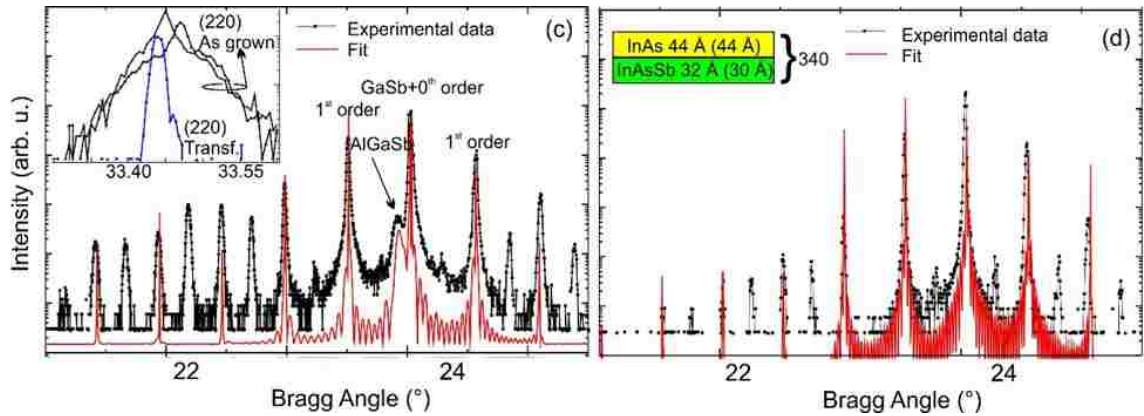


Figure 4.10: Co-planar diffraction pattern of the as-grown (a) and transferred (b) InAs/InAsSb SL membrane (Black solid circles). Both patterns are acquired around the GaSb (004) reflection. A fit to the experimental data is plotted as a red line in (a) and (b). The model layer structure obtained from fitting the co-planar patterns is shown in the inset, in (b). A slight discrepancy in the layer thickness deduced from simulations of the data in (a) and (b) is observed. The thickness within brackets is obtained from fitting diffraction patterns of the as-grown membrane.

calculated from the co-planar scans of the as-grown multilayers, and the in-plane lattice parameter obtained from the GI-XRD measurements.

We carry out a similar analysis for a 2.5 μm -thick InAsSb/InAs T2SL membrane. Figure 4.10(a) shows the co-planar diffraction pattern (black solid circles) around the (004) GaSb peak of the as-grown AlGaSb/InAs/InAsSb multilayer. The pattern is dominated by the GaSb substrate and the 0th order superlattice peaks at 24.01° and 24.03°, respectively. We identify the typical shoulder arising from the AlGaSb sacrificial layer as well as several superlattice fringes at lower and higher angles than the main peaks of the diffraction pattern. The large number of observable superlattice fringes indicate a good pseudomorphic crystal structure of the as-grown multilayer stack. We perform GI-XRD around the in-plane (220) reflection of the as-grown and the transferred membranes. Data are acquired around two perpendicular directions for the as-grown sample (line-circles pattern) and at one reflection for the transferred membrane (line-triangles pattern), as shown in Fig 4.11.

We find the substrate reflections close to their average position of 33.46° , i.e., in good agreement with the first sample set. We ascribe the broad features dominating the GI-XRD of the as-grown membrane to the large thickness of the superlattice, which may result in an inhomogeneous strain distribution. Interestingly, upon release, the (220) reflection sharpens indicating a more equal distribution of strain inside the transferred membrane. Calculations of the in-plane lattice parameter of the transferred membrane from Bragg's law yield $a_{\text{in-plane}} = 6.1000 \pm 0.0074 \text{ \AA}$, which is 0.066%, larger than the lattice parameter of the as-grown structure.

Following procedure reported for the InAs/GaSb SL, we determine the layer structure (right inset in Fig. 4.10(a)) by fitting a calculated diffraction pattern to the co-planar scans. The deduced parameters are 50 nm $\text{Al}_{0.3}\text{Ga}_{0.7}$ layer followed by 340 periods of the 3 nm $\text{InAs}_{0.78}\text{Sb}_{0.22}$ / 4.4 nm InAs superlattice. Good agreement is found with what expected from the growth conditions. Hereby, a single InAsSb layer represents the digital InAs/InSb alloy. We observe a set of reflections which cannot be fitted by partly relaxing the SL membrane, but are compatible with a structure that would have double the thickness for the InAsSb and InAs layer. Therefore, we ascribe these reflections to multiple diffraction effects due to the large number of periods and large total thickness of the T2SL. To confirm the strain relaxation of the transferred InAs/InAsSb SL membrane, we carry out co-planar diffraction around the (004) reflection of the membrane. The obtained pattern is depicted in Fig. 4.10(b). We observe the 0th order SL peak shifted to 24.038° , along with SL fringes up to the 4th order. As expected, the GaSb substrate peak and the shoulder from the AlGaSb layer have vanished. We again identify several higher orders SL fringes, but intensity between them reaches at some places the background level of our setup. Interestingly, the additional fringes observed for the as-grown sample are still present indicating the excellent crystal quality of the transferred membrane. We relax the in-plane lattice parameter of the structural model deduced from the as-grown sample to the parameter determined from the GI-XRD ($a_{\text{in-plane}} = 6.100005$

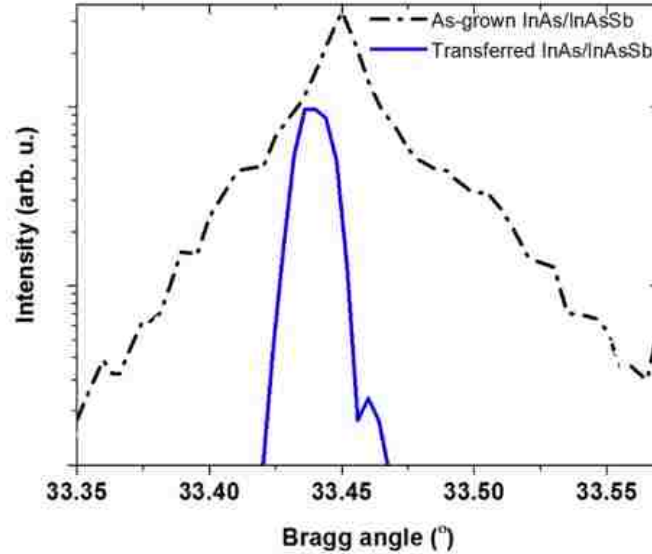


Figure 4.11: The GI-XRD around two (220) reflections of the as-grown SL and one (220) reflection of the transferred multilayer stack.

Å). Interestingly, we obtain a good agreement with the 0th order reflection, but the layer thickness require a minimal change (see inset Fig. 4.10(d) the thickness in the bracket are the thickness obtained from fitting diffraction patterns of the as-grown membrane).

Finally, we evaluate the effect of the release and transfer process on the strain distribution in each layer of the T2SL. For this purpose, we calculate the in-plane strain in the as-grown and transferred membranes using the in-plane lattice parameters obtained from XRD (4.1). Table 1 shows that the release and transfer process results in relaxation of the T2SL and redistribution of the strain established by epitaxial growth among the various layers in the SL. Specifically, while the membrane is freestanding in liquid, the strain through its thickness is balanced, such that only stretching occurs. During this process, part of the compressive strain established by epitaxial growth in the InSb layers transfers to InAs and GaSb, within the InAs/GaSb

Chapter 4. Sb-based membrane transfer using single-step etch process

Table 4.1: In-plane lattice parameters deduced from GI-XRD and co-planar XRD for the InAs/GaSb and InA/InAsSb T2SL, both before and after transfer to bulk Si. Calculated values of in-plane strain in each layer of the SL are also reported along with the bulk lattice parameters per each constitutive material of the multilayer stack.

T2SL	Layer	a_{bulk}	$a_{\text{in-plane}}$		$\varepsilon_{\text{in-plane}}$	
			As-grown	Transferred	As-grown	Transferred
GaSb/InAs/InSb	GaSb	6.0959 Å	6.0959 Å	6.1017 Å	0%	0.095%
	InAs	6.0583 Å			0.62%	0.072%
	InSb	6.4790 Å			-5.92%	5.8%
InAs/InAsSb	InAs	6.0583 Å	6.0959 Å	6.1000 Å	0.62%	0.69%
	InAsSb	6.1424 Å			-0.75%	-0.69%

SL. A similar process occurs within the Ga-free membrane, resulting in the tensile strain in InAs to increase and in the InAsSb to become less compressive.

We compare the in-plane strain obtained for the transferred membrane *via* XRD and continuum mechanical modeling of an elastically multilayer. In this analysis we assume that the strain state and the thickness of each layer within the SL are uniform in the growth direction. Furthermore, all the layers are regarded as perfectly bonded at any stage of the process. We calculate the in-plane strain in the various layers of the InAs/GaSb T2SL using the equations below

$$\varepsilon_{\text{GaSb}} = \frac{\Sigma_1 \eta_1 \varepsilon_{m,1} - \Sigma_2 \eta_2 \varepsilon_{m,2}}{1 + \Sigma_1 \eta_1 + \Sigma_2 \eta_2} \quad (4.1)$$

$$\varepsilon_{\text{InAs}} = -\frac{\varepsilon_{m,1}(1 + \Sigma_2 \eta_2) + \Sigma_2 \eta_2 \varepsilon_{m,2}}{1 + \Sigma_1 \eta_1 + \Sigma_2 \eta_2} \quad (4.2)$$

$$\varepsilon_{\text{InSb}} = \frac{\Sigma_1 \eta_1 \varepsilon_{m,1} + \varepsilon_{m,2}(1 + \Sigma_1 \eta_1)}{1 + \Sigma_1 \eta_1 + \Sigma_2 \eta_2} \quad (4.3)$$

where $\varepsilon_{m,1} = \varepsilon_{\text{GaSb}} - \varepsilon_{\text{InAs}}$ and $\varepsilon_{m,2} = \varepsilon_{\text{InSb}} - \varepsilon_{\text{GaSb}}$ are the mismatch strains between adjacent layers and $\Sigma_1 = M_{\text{InAs}}/M_{\text{GaSb}}$, $\Sigma_2 = M_{\text{InSb}}/M_{\text{GaSb}}$, $\eta_1 = t_{\text{InAs}}/t_{\text{GaSb}}$ and $\eta_2 = M_{\text{InSb}}/M_{\text{GaSb}}$ with M the biaxial modulus of the material and t layer thickness

[48, 49]. We obtain equations 6.1-4.3 using force balance between all the layers in SL

Table 4.2: Layer thickness within the InAs/GaSb and the InAs/InAsSb SL, as expected from the epitaxial growth conditions. Mismatch strain, $\varepsilon_{m,XRD}$, between adjacent layers in the as-grown T2SLs, as deduced from XRD. Biaxial modulus, $M=E/1-\nu$, with E, Youngs modulus and ν the Poissons ratio of the materials [1]. Residual in-plan straine as deduced from XRD, $\varepsilon_{in-plane,XRD}$, and from continuum mechanics modeling, $\varepsilon_{in-plane,CM}$.

T2SL	Layer	Thickness	$\varepsilon_{m,XRD}$	M	$\varepsilon_{in-plane,XRD}$	$\varepsilon_{in-plane,CM}$
GaSb/InAs/InSb	InAs	2.2 nm	-0.62 %	791 GPa	0.72%	0.55%
	GaSb	2.1 nm		914 GPa	0.09%	0.07%
	InSb	0.26 nm	6.52 %	629 GPa	-5.80%	-5.98%
InAs/InAsSb	InAs	4.4 nm	-1.37 %	791 GPa	0.69%	-0.59%
	InAsSb	3.2 nm		760 GPa	-0.69%	-0.72%

and the constraint of coherent lattice across the interfaces [49]. A similar analysis gives

$$\varepsilon_{InAsSb} = \frac{1}{1 + \Sigma_1 \eta_1} \quad (4.4)$$

$$\varepsilon_{InAs} = \frac{1 - \varepsilon_m(1 + \Sigma_1 \eta_1)}{1 + \Sigma_1 \eta_1} \quad (4.5)$$

to estimate in-plane strain in the InAs/InAsSb SL where $\varepsilon_m = \varepsilon_{InAsSb} - \varepsilon_{InAs}$ is the mismatch strain between InAsSb and InAs, $\Sigma_1 = M_{InAs}/M_{InAsSb}$ and $\eta_1 = t_{InAs}/t_{InAsSb}$. Biaxial modulus and layer thickness are indicated with M and t , respectively. In our analysis we utilize the layer thickness estimated from the co-planar XRD patterns of the as-grown membranes (see Figure ?? (b) and (d)), and we calculate the mismatch strain from the values obtained for the as-grown membrane from XRD (see Table 4.1). Table 4.2 shows that the in-plane strain values obtained from XRD and those calculated using continuum mechanical models differ by 0.03-0.17%. We attribute this discrepancy to non-uniformity of the strain state and thickness of the various layers in the growth direction.

As shown by equations 1-5, the residual strain in each layer of the T2SL is

determined by the thickness ratios between the various layers, η . Varying the layer structure within a T2SL is routinely used to engineer the intra-band gap and tune the absorption edge of the material within the IR range. As a result, it is crucial to calculate the strain distribution in the transferred membrane at varying thickness ratios between the InAs and GaSb, and the InAs/InAsSb. In these calculations we fix the mismatch strains to the values reported in Table 4.2. Figure ?? (a) shows that the amount of residual strain in the InAs and GaSb membrane increases with the $t_{\text{InAs}}/t_{\text{GaSb}}$. A similar result is obtained for the layers within the InAs/InAsSb T2SL (see Fig. ?? (b)).

We use high magnification SEM to characterize the sidewalls of the InAs/GaSb and InAs/InAsSb T2SL bonded to a new substrate. Prior to imaging, we release and wet transfer both membranes to bulk Si. We use photoresist as a protective coating of the InAs/GaSb T2SL, and we remove the polymer by solvent treatment before scanning electron microscopy. No protective coating is used during release of the Ga-free membrane. Figure ??(a) and (b) shows the InAs/InAsSb T2SL exhibit smoother sidewalls than the InAs/GaSb T2SL, thereby suggesting that a higher etching selectivity exists between the $\text{Al}_{0.4}\text{Ga}_{0.6}\text{Sb}$ sacrificial layer and the Ga-free SL. We evaluate the impact of release and transfer on the optical quality of the T2SL membrane by photoluminescence (PL) measurements at 300 K. Figure ?? (c)-(d) compare PL spectra acquired from unprocessed InAs/GaSb and InAs/InAsSb active layers while on the growth substrate, and after release and transfer to bulk Si. Ga-containing and Ga-free membranes have a thickness of $1.6 \mu\text{m}$ and $2.5 \mu\text{m}$, respectively, and they are both patterned in a 2D array of $10 \times 10 \mu\text{m}^2$ holes prior to release. Both as-grown T2SL exhibit broad PL spectra, with a dip at $\sim 4.2 \mu\text{m}$, originated by absorption of atmospheric CO_2 , and a cut-off wavelength at $5.5 \mu\text{m}$, determined by the InSb detector of the measurement set-up. PL acquired from as-grown and transferred membranes shows similar spectral features (see Fig. ?? (c)-(d)). Figure ?? (c)-(d) shows that release and transfer results in the PL intensity to decrease by \sim

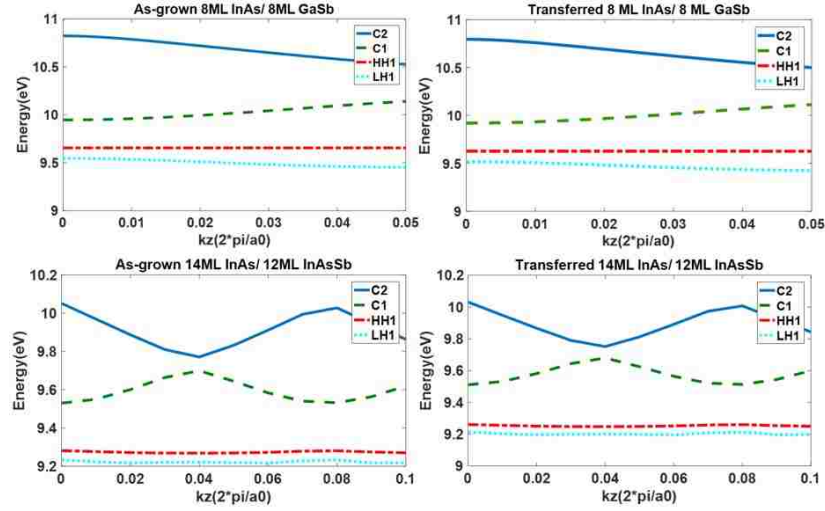


Figure 4.12: E-k dispersion curve along (001) direction (a) as-grown InAs/GaSb, (b) transferred InAs/GaSb, (c) as-grown InAs/InAsSb and (d) transferred InAs/InAsSb.

65% and $\sim 63\%$ for the InAs/GaSb and InAs/InAsSb, respectively. We attribute the lower PL intensity for either InAs/GaSb and InAs/InAsSb transferred membranes to the reduced volume of the emission area resulting from patterning of the films before release. We attribute the broad PL to C1-HH1 and C2-HH1 transitions. The two PL spectra are expected to broaden and merge at 300 K. Further, the variation in individual layer thicknesses may also contribute to broadening of the spectral features. Based on the in-plane lattice parameters obtained by XRD for the as-grown and transferred membranes (see Table 1), we calculate the transition energy from C1 and C2 (in the conduction band) to HH1 (in the valance band) using the empirical pseudopotential method. Simulations yield a 0.2920 eV and a 1.165 eV transition energy from C1 to HH1 and from C2 to HH1, respectively, for the as-grown membrane. These intra-band energy gaps change to 0.2933 eV and 1.163 eV in the transferred SL, due to strain redistribution among the layers. We expect the calculated change for the transition energy in the transferred sample to result in a 19 nm blue-shift and a 2 nm red-shift of the RT-PL peaks originated from the C1-HH1 and from C2-HH1

Chapter 4. Sb-based membrane transfer using single-step etch process

transitions. For the InAs/InAsSb structure, the calculated transition energies vary from 0.2453 to 0.2471 eV (from C1 to HH1) and from 0.769 to 0.765 eV (from C2 to HH1). A corresponding blue-shift of 37 nm and a red-shift of 8 nm is expected in the PL peaks acquired from transferred membrane. These estimated changes in the PL spectra are below the resolution of the measurement PL setup.

Chapter 5

Sb-based membrane photodetector

Currently available infrared detectors are classified as either thermal or photonic detectors. Thermal detectors, such as bolometers, operate at room temperature, thereby enabling low-cost commercial applications, including surveillance and night vision detection in high-end automobiles.[70] Photonic detectors, on the other hand, have much higher performance (sensitivity, responsivity, and speed) compared to thermal detectors but require cryogenic cooling. Moreover, photonic focal plane arrays are realized using an expensive fabrication process, in which part of the processing is wafer-level on the host substrate including mesa delineation, surface passivation, metal evaporation, and indium deposition. This process is followed by a die-level fabrication involving dicing, flip-chip bonding to a silicon read-out integrated circuit, substrate thinning/removal, and packaging. The die-level steps are low-yield processes that dramatically increase the cost and fabrication time for the focal plane arrays. One of the reasons for the low cost of microbolometer detector arrays is that the entire fabrication and packaging is done at a wafer level. In this work, we demonstrate an approach based on epitaxial lift off [8, 71] to realize InAs/InAsSb type II superlattice membrane (T2SL-M) detectors that can be adapted for large-scale wafer integration of photonic detectors on silicon substrates or other flexible

materials.

5.1 Sb-based membrane transfer

The samples were grown by molecular beam epitaxy in a Vacuum Generators V80H solid-source machine equipped with valved Sb and As crackers. The 60 nm-thick sacrificial layer composed of $\text{Al}_{0.4}\text{Ga}_{0.6}\text{Sb}$ followed by the 2.5 μm PIN homojunction device comprising of 14 ML InAs/12 ML $\text{InAs}_{0.81}\text{Sb}_{0.19}$. In which the n-type layers were Te-doped to $2 \times 10^{18} \text{ cm}^{-3}$, while the absorber and p-contact layers were Be-doped at $3 \times 10^{16} \text{ cm}^{-3}$ and $2 \times 10^{18} \text{ cm}^{-3}$, respectively.

Following to growth, we used single-step etch dry transfer method to peel off the InAs/InAsSb T2SL pixels from the growth substrate to the host substrate. Release and dry transfer of membranes requires a tight control of the etching time of the sacrificial layer. Indeed, if dry transfer is performed before a significant portion of the membrane is completely released, the undercut film will peel off while the rest of the pixel will remain on the native substrate, yielding transferred pixels with holes in the center. On the other hand, if the pixels are transferred long after the undercut is complete, the pixels may have shifted or been released from the substrate surface, resulting in misaligned or missing pixels after transfer to the new substrate. A perfect dry transfer yields membranes with small defects on the released side, and it is achieved when pixels are peeled off from the native substrate right before complete etching of the sacrificial layer. Transferred membranes were characterized by optical and SEM. Fig. 5.1 shows a large and a small scale images of the transferred pixels. The area of the transferred arrays was $5 \times 5 \text{ mm}^2$. Fig. 5.1 shows defects, namely, missing pixels, in the transferred array. The yield of our release and transfer process was $\sim 70\%$ 75% . We attribute the defects to particles contaminating the stamp or the new host, resulting in a poor adhesion of the membrane to the PDMS or the new

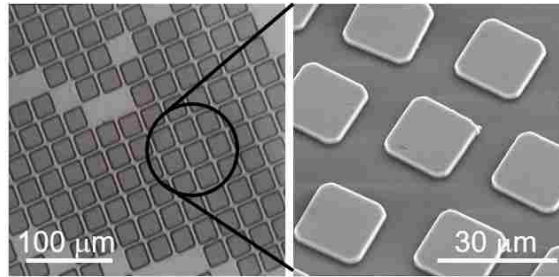


Figure 5.1: Optical microscope and SEM images of transferred InAs/InAsSb pixels on Si/Ti/Au/Ti

host during transfer. The yield of the transfer process can be then reduced by better preparation and cleaning of the stamp and new host substrate.

5.2 Sb-based membrane optical characterization

The optical quality of the transferred T2SL-M pixels and as-grown sample was evaluated by photoluminescence (PL) measurements at room temperature using an argon laser with a power of 1.5 W, an InSb detector, a germanium filter, and a monochromator equipped with a grating rated for 2.6 to 6 μm . PL measurements for both the as-grown sample and the transferred pixels showed midwavelength IR response, but the transferred pixels had additional Fabry-Perot oscillations. These additional oscillations (Fig. 5.2) were likely caused by reflection from the Ti/Au/Ti-coated Si substrate.

5.3 Sb-based membrane photodetector fabrication

Indium-bump-free infrared photodetectors based on T2SL-M were then fabricated using the process shown in Fig. 5.3. InAs/InAsSb pixels were first transferred onto

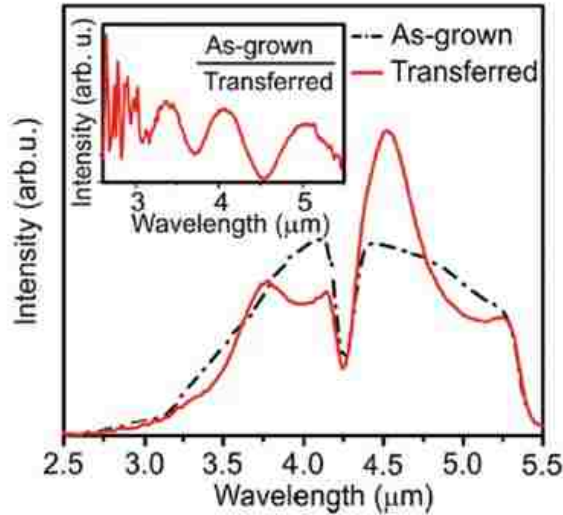


Figure 5.2: A comparison of room-temperature PL spectra between unprocessed InAs/InAsSb on a GaSb substrate and transferred InAs/InAsSb membrane on Si/Ti/Au/Ti substrate.

a supporting Si substrate coated with a Ti (50 Å)/Au (150 Å)/Ti (50 Å) film. The metal layers served as the bottom contact of the detectors. The transferred membranes were annealed at 150 °C on a hot plate for 5 min. Any native oxide film grown on the side walls of the mesas was removed by a 30 s etching in hydrochloric solution (HCl:DI water = 1:20). Then, 100 nm of Si₃N₄ was deposited by PECVD as a blanket coating, covering all the pixels and substrate. This dielectric layer passivated the photodetector pixels and promoted adhesion of the pixels to their new substrate. The dielectric layer also acted as an insulator between the top and bottom contacts. Next, a lithography step was undertaken and a dry reactive ion etch (RIE) was performed to open areas in the Si₃N₄ for metallization. After standard photolithography to define the top and bottom contacts, native oxides were removed from the pixels, using diluted HCl:H₂O (1:20). Finally, Ohmic contacts were thermally evaporated on the defined area using Ti (500 Å)/Pt (500 Å)/Au (3000 Å). Conventional single pixels with a 410×410 μm² area and 300 μm-diameter optical apertures were processed on as-grown (*i.e.*, unreleased membranes). Mesa etching was performed using

Chapter 5. Sb-based membrane photodetector

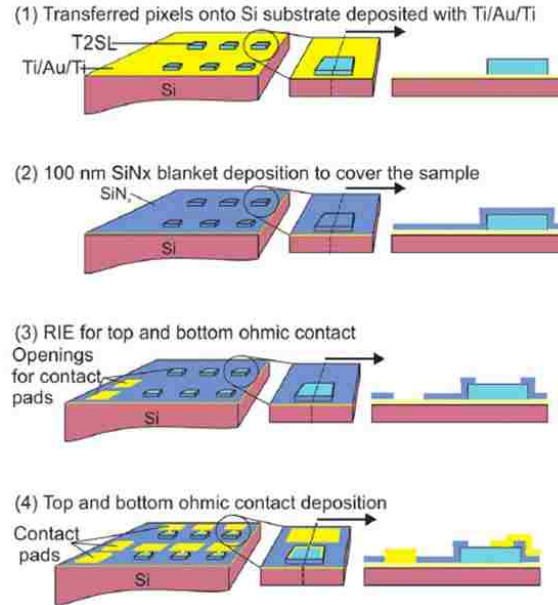


Figure 5.3: Indium-bump-free single pixel photodetector process; (1) T2SL pixels transfer to Si substrate deposited with Ti/Au/Ti, (2) Si_3N_4 blanket layer deposition, (3) Standard lithography and RIE etch to open the area for metal contact deposition, (4) metal contact deposition.

an ICP reactor with BCl_3 gas. The resulting etch depth was $2.4 \mu\text{m}$, a depth corresponding to the middle of the bottom contact layer of the detector. The devices were passivated by a 100 nm-thick Si_3N_4 layer after a short (30 s) dip in a hydrochloric acid solution ($\text{HCl}:\text{H}_2\text{O}=1:20$) to remove native oxides formed on the mesa sidewalls. The Ohmic contacts were simultaneously evaporated on the bottom and top contact layers and consisted of Ti (500 Å)/Pt (500 Å)/Au (3000 Å).

The electrical response of a $24 \times 24 \mu\text{m}^2$ Indium-bump free photodetector on Si was evaluated by I-V measurements, and the results were compared with the as-grown sample. Fig. 5.4 shows the I-V characteristics for both devices at 77 K. Previous publications have reported a comparison of the dark current in devices with different areas fabricated on the same as-grown T2SL. Specifically, lower dark current densities were reported for devices with larger areas, suggesting that surface recombination

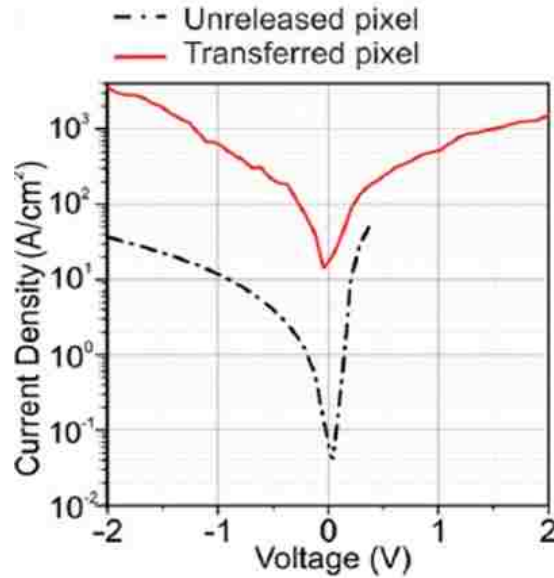


Figure 5.4: current voltage characteristics of Indium-bump-free single pixel and conventional single pixel at 77 K.

at the side-walls plays a crucial role in determining the dark current.[59, 72, 73, 58] As reported in Refs. 8 and 9, the slope of the inverse of the dynamic resistancearea product (RA_{eff}) as a function of the perimeter-to-area ratio at 77K is directly proportional to the surface-dependent leakage current of the diode. The inverse of the dynamic resistancearea product was calculated using

where $RA_{\text{eff,bulk}}$ is the bulk contribution of the RA_{eff} ($\Omega \text{ cm}^2$), r_{surface} is the surface resistivity ($\Omega \text{ cm}$), and P and A are the perimeter and the area of the device, respectively. In this experiment, the perimeter to area ratio was 0.0097 and 0.17 for a pixel with a $410 \times 410 \mu\text{m}^2$ area, and a $24 \times 24 \mu\text{m}^2$ area, respectively. The result is that the surface recombination at the side-walls plays a much less significant role in determining the dark current in the larger pixels. The calculated value of the resistivity, using Equation (1), for the Indium-bump-free photodetectors pixel was $57 \times 10^{-3} \Omega \text{ cm}$, which matches the numbers reported in the reference. Therefore, the higher dark current density of the transferred pixel was partially attributed to surface

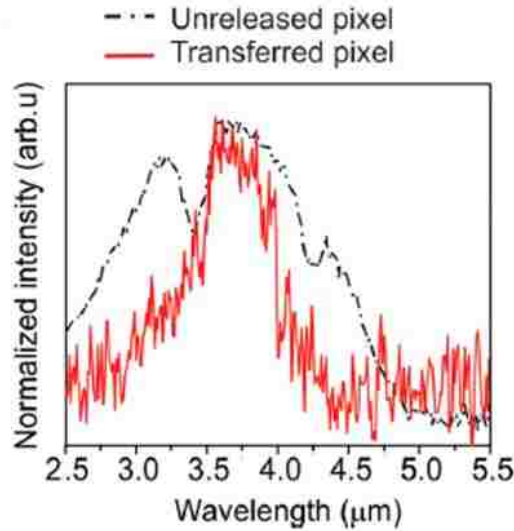


Figure 5.5: Normalized zero bias spectral response measured at 77 K.

leakage currents. The spectral response of the device was evaluated using a broad spectrum IR light source (Hawk Eye IR-18), which was chopped and sent through a monochromator. The grating of the monochromator was optimized for 39 μm . The monochromator output illuminated the detector-under-test, which was cooled down to 77K in cryostat and biased with a preamplifier. This allowed the output voltage response to be collected and recorded by a lock-in amplifier. Fig. 5.5 illustrates the normalized spectral response. The Fabry-Perot effect caused a spectral narrowing and intensity amplification of the PL peak in the transferred sample, which reduced the FWHM and distorted the apparent bandgap of the material in comparison to the as-grown sample.

The transferred pixel for spectral response measurements was also prepared similar to the PL sample, with identical substrate preparation and detector material. Therefore, Fabry-Perot is likely to occur in this pixel as well and would manifest as a distortion in the spectral response. Because of the small pixel size and high dark current which leads to low signal-to-noise ratio of the transferred sample, only

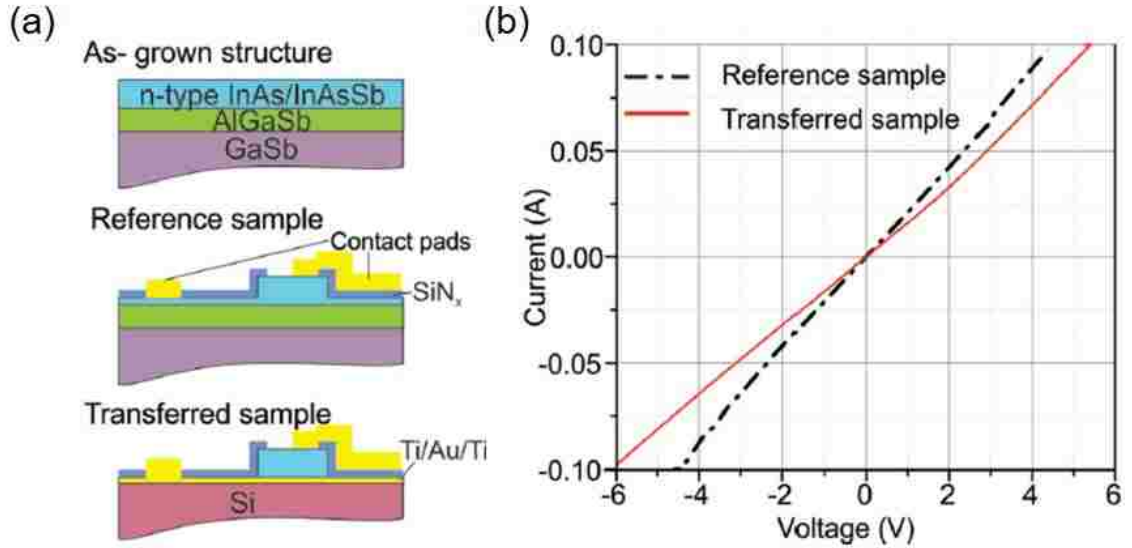


Figure 5.6: Bottom contact behavior, (a) Schematic of reference and transferred samples cross sections, (b) Current-voltage characteristics of reference and transferred sample at 77 K.

the highest part of the response was observable, which led to the spectral response having an apparent cut-off at $4.3 \mu\text{m}$. In both conventional and Indium-bump-free T2SL PIN infrared photodetectors fabrication techniques, top metal contacts were thermally deposited with the same thickness on P-doped InAs/InAsSb layer. In order to investigate how the transfer fabrication method affects the bottom metal contact characteristics, we grew 700 nm-thick N-doped InAs/InAsSb T2SL on a 60 nm $\text{Al}_{0.4}\text{Ga}_{0.6}\text{Sb}$ sacrificial layer on GaSb substrate. The electrical characteristics of the reference and the transferred structure were compared. For the reference sample, Standard optical photolithography was used to define a 2D array of $24 \times 24 \mu\text{m}^2$ square mesa followed by an ICP reactor dry etch with BCl_3 gas. The resulting etch depth was 600 nm that corresponds to the very bottom layer of the highly doped structure. The mesa was passivated by a 100 nm-thick Si_3N_4 layer, and the Ti (500 Å)/Pt (500 Å)/Au (3000 Å) contacts were simultaneously evaporated on the bottom and top of the mesa.

Chapter 5. Sb-based membrane photodetector

For the transferred sample, mesas with the same size were defined and etched to the bottom of the sacrificial layer. Next, the N-doped InAs/InAsSb layer was dry-transferred to Si coated with Ti (50 Å)/Au (150 Å)/Ti (50 Å). Later, the Indium-bump-free process was followed for the transferred pixels. A schematic of the cross section of both processed samples is shown in Fig. 5.6(a). The electrical characterization of the reference and transferred samples was performed in a standard probe station at 77 K. Figure 5.6(b) shows Ohmic bottom contact with $R \sim 50 \Omega$ for both reference and transferred structure. EDS and current-voltage characterization suggest that the release and transfer of membranes did not affect significantly the quality of the bottom contact.

Chapter 6

Sb-based membrane transfer using two-step etch process

Epitaxially grown single-crystalline semiconductor membranes offer a new platform for fundamental science and advanced technology. Progress in membrane fabrication has already significantly altered the landscape, as it relates to properties and applications of group IV and III-V semiconductors, III-nitrides and various oxide materials. Membrane technology applied to Sb-based membranes enables accurate material characterization and engineer strain distributions, which are not obtainable within the limitations of epitaxial growth processes. Membrane fabrication is based on wet and dry transfer process for layers and mesas respectively. In transfer process, membrane is released from the growth substrate by selectively etching the sacrificial layer grown beneath. Further, the freestanding membrane is bonded to the new substrate. In the case of group III-V membrane transfer process, most of the sacrificial layers use Aluminum (Al) containing compounds and rely on the fact that Al and compounds containing Al etch faster than the overlying compound semiconductor or the underlying substrate. However this precludes the inclusion of Al and Ga in the active above the sacrificial layer. Previously, we had demonstrated epitaxial lift off

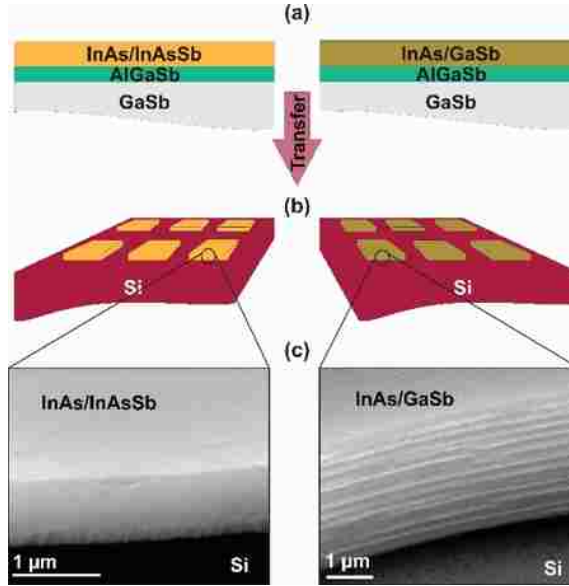


Figure 6.1: Ga free and Ga containing T2SLs after transfer to alternative substrate, (a) Schematic of as-grown InAs/InAsSb and InAs/GaSb structure. (b) Schematic of transferred T2SLs to Si substrate. (d) Off-axis SEM image of the sidewalls of the T2SLs pixels after transfer which shows that diluted HF is highly selective for Ga free T2SL and has poor selectivity for Ga containing T2SL. The diluted HF etchant, etches through the GaSb layers during the release process.

process for InAs/InAsSb type II superlattice membrane (T2SL-M) which is applicable in photonic detectors. Since InAs/ InAsSb is Al and Ga free containing layer, the successful realization of mesa transfer relied on an HF-based highly selective wet etch and an Al-based sacrificial layer. Poor selectivity of the etchant for Al containing sacrificial layer in Al and Ga containing membrane, etches the mesas through the sidewalls and leaves a rough area. Figure 6.1 shows off-axis scanning electron micrograph (SEM) image of the sidewalls of InAs/InAsSb and InAs/ GaSb T2SL mesas after transfer.

In optoelectronic devices, the rough sidewalls increase the imperfections on the sidewalls and consequently enhance the surface effect and the noise of the device. Specially, in small size optoelectronic devices since the surface effect is dominant

in generation-recombination compare to bulk, it plays a very important role in increasing the noise. Recently, scaled smaller size optoelectronic device have received increasing attention due to higher speed, more powerful and higher resolution. For instance, in photodetectors, smaller pixel size increase the resolution of the imager and in LEDs, smaller size enhances device speed. Aforementioned, the essential challenge in small size optoelectronic is the noise due to the surface effect.

In optoelectronic devices, undesirable generation-recombinations are the source of the noise. For instance, in photonic detectors, the total dark current, as a noise source, is comprised by bulk and surface components. The bulk component of the dark current may reduce significantly by hetrostructure engineering in T2SL detectors. Thus, the surface component is the dominant contributor to the total dark current. Furthermore, previous studies have reported in p-i-n devices with $25 \times 25 \mu\text{m}^2$ mesa size, the surface effect is dominant in dark current. Hence, the reduction of surface effects is critical for high-performance optoelectronic devices.

6.1 Two-step etch transfer process

Diluted HF is the fastest etchant for the Al containing sacrificial layers, compared to other selective etchants in literature, but poses a huge problem for transferring mesas that are made out of materials that have very similar etch rates to the sacrificial layer. Standard (one-step etch) dry transfer process which is based on defining mesas using photoresist photolithography, sacrificial selective etching, using stamp to peel off the mesas and transfer to a new substrate, has been reported before for different material systems. Aforementioned, poor selectivity of etchants in Al and Ga containing membrane transfer process causes hollows in those layers that leads to increased area of dangling bonds area and dark current accordingly. Figure 6.2 (a) and (b) shows cross-sectional SEM and scanning transmission electron microscopy

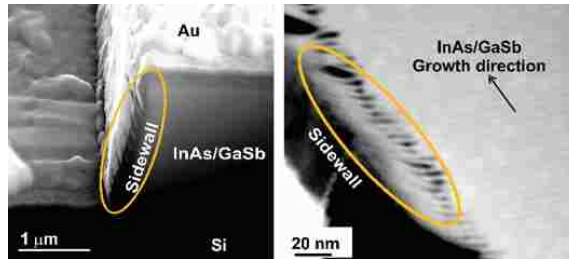


Figure 6.2: Structural characterization of the sidewall of the Ga containing T2SL. (a) cross-sectional SEM image of the sidewall of InAs/GaSb shows release process leaves hollows on the sidewall of the mesa, (b) STEM image of a lamella of the transferred mesa sidewall exhibits that the diluted HF etches through GaSb layer.

(STEM) images of the sidewall of InAs/GaSb after a non-selective etch, release and transfer. A lamella of the transferred pixel ($150 \text{ nm} \times 5 \text{ mm} \times 3 \text{ mm}$) is cut out by a focused ion beam (FIB) and transferred onto a TEM grid. Figure 6.2 (b) exhibits that diluted HF etches through GaSb layers in Ga containing T2SL.

The critical point to transferring Al and Ga containing active layer is following a method in which the wet solution etches the sacrificial layer and does no harm to the rest of the structure. Therefore, we developed a two-step-etch process (see Fig. 6.3 (b)-(g)) to protect the side walls of the active region from the etchant solution. In this process the first step is defining the mesa ($25 \times 25 \mu\text{m}^2$) using standard lithography, followed by inductively-coupled plasma (ICP) etching (etching step 1) down to the top surface of the sacrificial layer. Later, we use another lithography step to apply the $50 \times 50 \mu\text{m}^2$ photoresist squares to protect SLS pixel from any damage from the solution. We do one more ICP etching (etching step 2) to enhance access to the sacrificial layer. Finally, we hard bake the photoresist at 120 C for 10 minutes to harden it and increase the adhesion between photoresist and SLS pixel, in preparation for the sacrificial layer wet etch process. After sample preparation, the sacrificial layer is partially etched in diluted HF (Hf/ DI water : 1/20), after 2 hours the pixels are almost released. Next, using polydimethylsiloxane (PDMS) or thermal release tape

(TRT), we peel off the pixels (still protected with the photoresist) from the original substrate. Then, the remaining sacrificial layer is removed by leaving the pixels in the HF solution, while the pixels are still attached to the PDMS or TRT. Finally, the pixels are transferred to a new substrate, and the protective photoresist layer is removed using a combination of an acetone bath and oxygen plasma. 6.3 (1-e)). We transferred InAs/GaSb T2SL mesas using two-step etch process (with PR as protective layer). Figure 6.3(h) shows SEM image of a pixel after transfer using two-step etch method and PR removal. smooth sidewalls of mesas after exhibits the effectiveness of the process. In this work, we use two different sacrificial layer 1) $\text{AlAs}_{0.09}\text{Sb}_{0.91}$ digital alloy (DA) and 2) $\text{Al}_{0.4}\text{Ga}_{0.6}\text{Sb}$ ternary. The $\text{AlAs}_{0.09}\text{Sb}_{0.91}$ digital alloy sacrificial layer contains 100% Al which potentially can enhance the etch rate. Moreover, $\text{AlAs}_{0.09}\text{Sb}_{0.91}$ layer contains two group V which make it possible to have a lattice matched sacrificial layer to the GaSb substrate and grow a thick sacrificial layer. On the other hand, $\text{Al}_{0.4}\text{Ga}_{0.6}\text{Sb}$ ternary has 60 nm kinetic critical thickness which leaves no cross-hatching in the layer.

6.2 material characterization

The optical properties of the transferred pixels with AlAsSb DA and AlGaSb sacrificial layer were evaluated by photoluminescence (PL) measurements at a number of temperatures, and compared with as-grown materials. This was accomplished using a 635 nm AlGaAs diode barstack laser with a power of 1.5 W, an InSb detector, a 2.5 μm long pass filter, and a monochromator equipped with a grating rated for wavelengths from 2.6 to 6 μm . PL measurements at different temperatures for both the as-grown and transferred samples showed that as the temperature reduces, the PL peak becomes more narrow and has a blue shift. This blue shift is a well-documented phenomenon, as characterized by Varshni. At lower temperatures, carriers get less

energy from phonons to get to the non-radiative centers which causes the less FWHM in the PL spectra. The 75% (check carefully) lower PL intensity observed for the transferred sample, when compared to the as-grown sample, is partially explained by the transferred pixels smaller volume of active material than the as-grown material (reducing the light emission intensity to approximately 1/3), and also because the pixels have more surface area (sidewalls) where surface recombination can dominate.

Furthermore, we performed TEM to evaluate the quality of the interface between the transferred pixel and the new substrate. A lamella of the transferred pixel (100 nm \times 5 μ m \times 3 μ m) is cut out by a focused ion beam (FIB) and transferred onto a TEM grid. Figure 6.4 (c) shows high resolution TEM image of T2SL crystal quality and complete bonded interface of the transferred pixel to new host substrate.

To verify the complete removal of the Al-based sacrificial layer, X-ray photoelectron spectroscopy (XPS) is performed. XPS is a surface-sensitive quantitative spectroscopic technique that measures the elemental composition. (reference) We transfer 25 \times 25 μ m² mesas to TRT, and utilize (XPS) to characterize the chemical compositions contained on the backside of the mesas which was immediately grown on Al containing sacrificial layer. Al compositions is not detected by XPS (see spectra in Figure 6.4 (d)), confirming that no residue of the AlGaSb layer after release and transfer to the stamp.

6.3 Device fabrication and characterization

6.3.1 Fabrication

As mentioned before, two-step etch process is a transfer method which protect the Al and Ga containing membrane during the selective Al containing sacrificial layer

Chapter 6. Sb-based membrane transfer using two-step etch process

etch. This process leaves smooth sidewalls after transfer to a new substrate. Here, we fabricate and characterize three different type of IR photodetectors on InAs/GaSb membrane. First type of detectors are fabricate on InAs/GaSb T2SL transferred mesas to bulk Si using two-step etch process. For the second type, the same device fabrication process is followed for InAs/GaSb transferred to bulk Si using one-step etch process. Finally, we used the conventional detector fabrication method to process the detectors on growth (GaSb) substrate. In both one-step etch and two-step etch process, the $25 \times 25 \mu\text{m}^2$ mesas transferred onto a supporting Si substrate coated with a Ti (50 Å)/Au (150 Å)/ Ti (50 Å) film. The metal layers serves as the bottom contact of the detectors. Any native oxide film grown on the side-walls of the mesas is removed by a 30 seconds etching in hydrochloric solution (HCl:DI water/1:20). Then, 100 nm of Si₃N₄ is deposited by plasma-enhanced chemical vapor deposition (PECVD) as a blanket coating, covering all the pixels and substrate. This dielectric layer passivates the photodetector pixels and promotes adhesion of the pixels to their new substrate. The dielectric layer also acts as an insulator between the top and bottom contacts. Next, a lithography step is undertaken and a dry reactive ion etch (RIE) is performed to open areas in the Si₃N₄ for metallization. After standard photolithography to defined the top and bottom contacts, native oxides were removed from the pixels, using diluted HCl:H₂O (1:20). Finally, Ohmic contacts were thermally evaporated on the defined area using Ti (500 Å)/Pt (500 Å)/Au (3000 Å). We compare the device spectral response and dark current density of the transferred and fabricated devices on Si substrate with a $25 \times 25 \mu\text{m}^2$ device fabricated the on GaSb substrate using conventional method to compare the performance of the fabricated photodetectors using different methods. In conventional method mesas are defined using standard photolithography which followed by dry ICP etch to the middle of the highly p-doped bottom contact. The rest of the device process, consisting of Si₃N₄ deposition, dry etch to open contact areas and metallization, is similar to transferred device fabrication.

6.3.2 Characterizations

In this work, we have fabricated photodetector based on a 1.6 μm -thick InAs/GaSb p-i-n SL to bulk Si. Previous investigations have shown the dark current of a detector can be represented as two major components of bulk component and perimeter component (surface component).

$$I_d = AJ_{\text{bulk}} + PJ_{\text{perimeter}} \quad (6.1)$$

J_{bulk} contains 1) Generation current associated with the Shockley-ReadHall (SRH) process in the depletion region of the detector, 2) Thermally generated diffusion current associated with Auger or radiative process in both the n- and pextrinsic regions of the detector. A surface current, $J_{\text{perimeter}}$, associated with the surface states in the junction. Equation (1) shows by reducing the size of the device, P/A increased and the surface current remains a dominant contributor to the total dark current. Based on previous studies, the performance of detector device with typical mesa dimensions of $\sim 20 \times 20 \mu\text{m}^2$ is strongly dependent on surface effects due to their large surface/volume ratio. Surface effect can be reduced by different passivation method but it is still a big challenge for T2SL detectors.

We perform device characterization at 77K, i.e., the typical operating temperature of IR detectors. Figure 5 (a) compares the dark current density (J-V) of the three different fabricated devices (as-grown, one-step etch transferred and two-step etch transferred) between -1 V and 1V. In addition to symmetrical J-V behavior due to the very leaky diode (p-i-n structure), one-step etch transferred and fabricated device shows $\sim 440 \text{ A/cm}^2$ at -0.1 volt which is the highest dark current density among all three different fabricated device. Both highlighted features of the J-V characteristics measured for the detector on Si suggest that the current follows a low resistance path along the device side-walls. We attribute the higher conductance of the membrane perimeter to the poor selectivity of the etching solution with respect to GaSb, and

resulting lateral etching of material during the release process. Dark current density (J-V) of the fabricated device on two-step etch transferred pixel shows a perfect diode (asymmetric J-V) behavior with four orders of magnitude lower dark current density at -0.1 volt bias. This significant reduction in dark current is due to protecting the sidewalls during the release and transfer. The same measurement is done for fabricated device on growth substrate (GaSb). Figure 6.5 (a) shows $\sim 3 \text{ A/cm}^2$ dark current density at -0.1 bias voltage which is two order of magnitude lower than fabricated detector on Si using one-step etch process to transfer pixels and one order of magnitude higher than two-step etch transferred pixels.

Figure 6.5 (b) shows the normalized spectral response of three type of devices which covers from 1.7-5.7 μm from IR spectra. The visible oscillations in the spectral response of the photodetector based on the transferred membrane originate from multiple reflections at the metal coated Si surface.

Figure 6.6 shows a histogram of dark current density for different types of fabricated devices. It shows the dark current density of the devices is constant in each type of fabricated device.

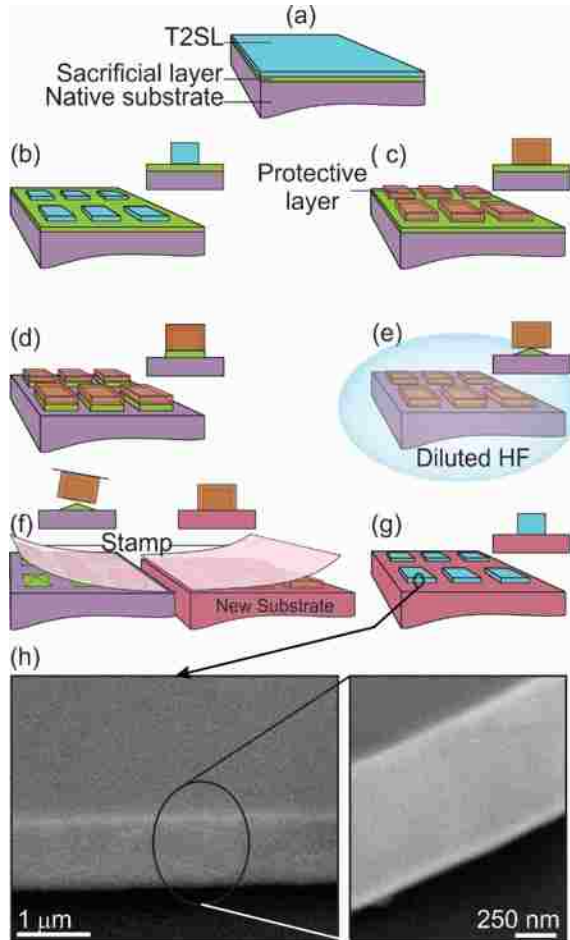


Figure 6.3: Schematic illustration of T2SL two-step etch process, release and transfer from the original growth substrate to a new host. (a) As-grown T2SL on a GaSb growth substrate coated with an $\text{Al}_{0.4}\text{Ga}_{0.6}\text{Sb}$ sacrificial layer. (b) Unreleased membrane patterned into a 2D array of mesas via standard photolithography and etched using ICP to the top of the sacrificial layer to define pixels (first step etch). (c) Pixels covered with PR, using standard photolithography and then hard backed at $120\text{ }^\circ\text{C}$ for 10 minutes. (d) Second step ICP etch to the bottom of the sacrificial layer to enhance etchant access to the sacrificial layer. (e) Partial selective etch of the sacrificial layer in $(\text{HF}:\text{H}_2\text{O})$. (f) Removal of the mesas from the growth substrate and transfer to the new support, using a stamp. (g) Removal of the PR from the transferred pixels. (h) SEM image of the sidewall of a transferred pixel using two-step etch process.

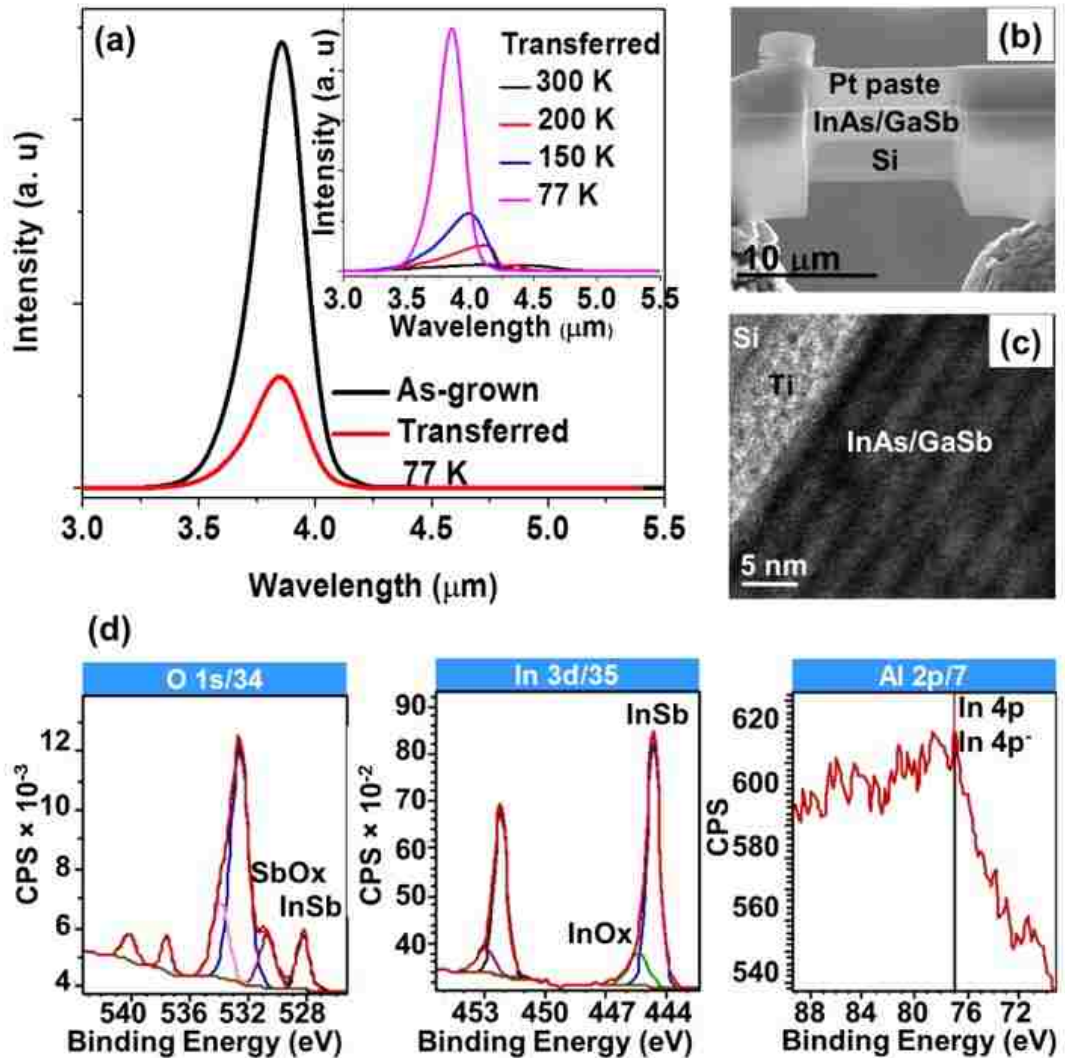


Figure 6.4: Optical and structural characterization of the transferred InAs/GaSb pixels using two-step etch process (a) PL spectra acquired from as-grown and transferred InAs/GaSb using two-step etch process at 77K shows the same spectra and the inset plot exhibits the acquired PL from as-grown transferred InAs/GaSb T2SL on a Si substrate at different temperature, (b) SEM image of the transferred lamella to TEM grid. (c) High resolution TEM image from the transferred pixels and Si/Ti substrate. (b) and (c) show complete bonding between InAs/GaSb pixel and host substrate and rule out the presence of voids or particles at the interface. (d) XPS analysis of the transferred pixels on to thermal release tape which gives access to the bottom of the pixels.

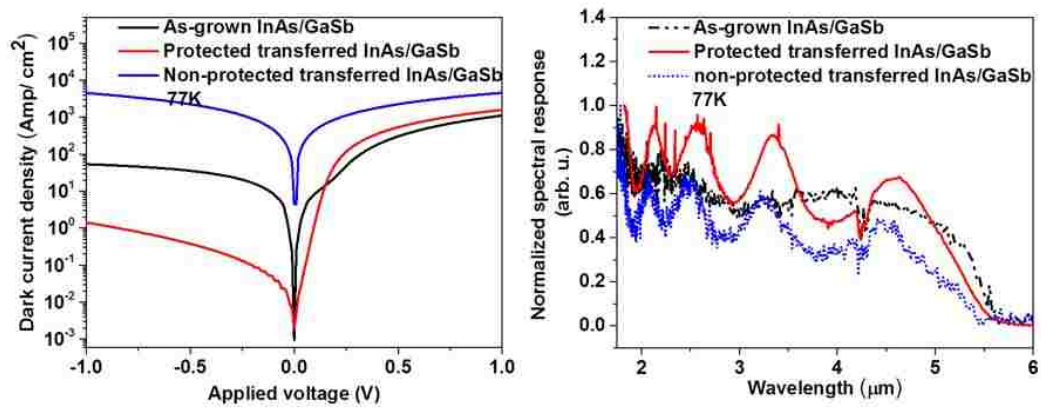


Figure 6.5: Device characterization of 1.6 μm -thick InAs/GaSb T2SLs at 77 K. Three different types of fabricated device with the same lateral dimension of the membrane is 2424 m^2 are compared. First type of device is fabricated on growth substrate (GaSb), second type is fabricated is fabricated on transferred pixels on Si using two-step etch process and the third type is fabricated on pixels on Si substrate using sing-step etch process. (a) Dark current density acquired from three types of device, (b) Spectral response comparison of three different types of devices.

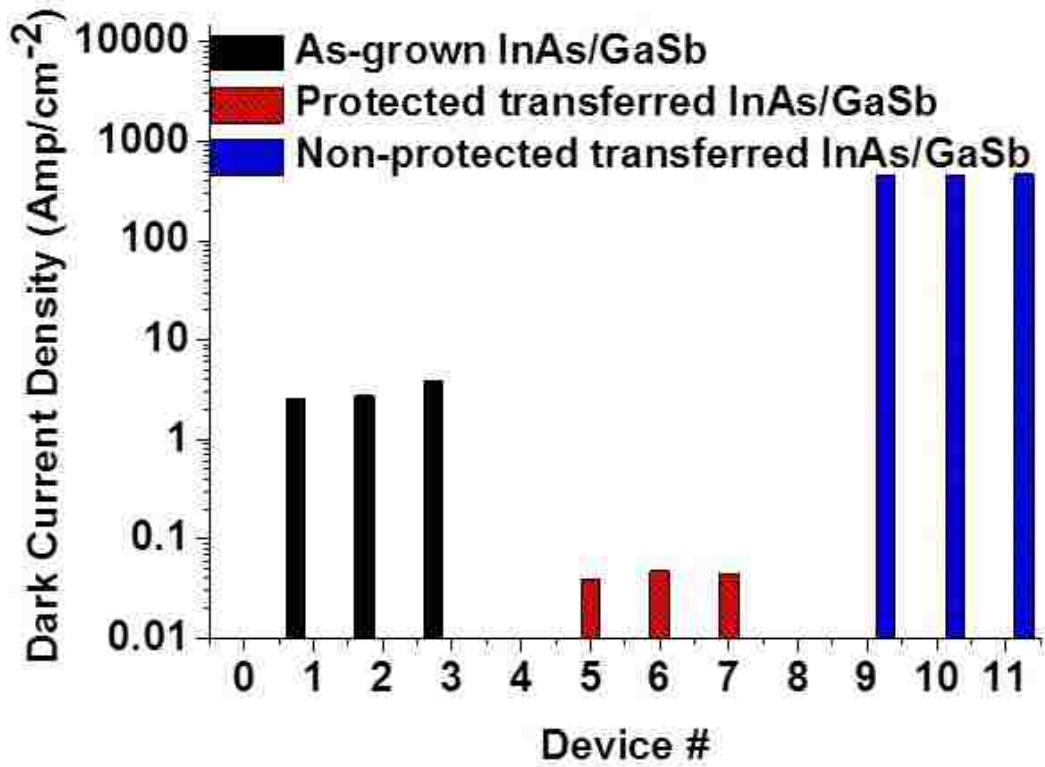


Figure 6.6: Histogram of the dark current density vs. device number. Black lines represent the fabricated devices on growth substrate (GaSb), red lines represent the fabricated devices on transferred pixels on Si substrate using two-step etch and the fabricated devices on transferred pixels on Si substrate using one-step etch.

Chapter 7

Future work

7.1 Conclusion

Integration of Sb-based compound membranes with a Si substrate will potentially solve a number of technological challenges in the fabrication of infrared (IR) optoelectronic devices based on type II superlattices (T2SLs). Typically, T2SLs are epitaxially grown on GaSb substrates. However, GaSb substrates absorb much of the incoming or outgoing radiation in the IR range, thus reducing the signal-to-noise ratio (SNR). In addition, T2SLs/GaSb substrates are bonded to a Si read-out circuit (ROIC) to realize infrared focal plane arrays (FPAs). As the detectors-ROIC combination is cryogenically cooled during operation, the large thermal mismatch between the GaSb substrate and the Si ROIC results in structural failure of the imaging device, via cracking of the absorber or delamination of the detectors from the ROIC. To overcome these issues, the GaSb substrate is routinely removed via chemical-mechanical polishing (CMP) and selective etching, thereby increasing manufacturing costs, and leading to device failure. Transfer of T2SL to Si will eliminate the issue of the thermal mismatch between the ROIC and the IR detectors, thereby

Chapter 7. Future work

increasing the yield of the fabrication process.

Furthermore, transfer of Sb compounds to insulating materials will enable a thorough investigation of electrical transport in the heterostructure via Hall and van Der Pauw measurements, i.e., two techniques not applicable to Sb-based heterostructures supported by semiconducting growth substrates. These studies will foster a greater understanding of fundamental properties of Sb-containing multilayers, such as background carrier concentration, lateral and vertical carrier mobility, both of which significantly affect the device performance.

Membrane technology applied to Sb-based structures will enable to engineer strain distributions, which are not obtainable within the limitations of epitaxial growth processes. For instance, a T2SL will undergo elastic deformation during the release process, redistributing strain intrinsic to the deposition process between the InAs and (InAs,Ga)Sb layers in the SL. Furthermore, Sb-based membranes may be bonded and conformed to patterned surfaces of various shapes and sizes to induce local strain of different types and amplitudes. As strain modifies electronic band structure, electronic transport, optoelectronic properties, and phonon structure, one might harness it to obtain unique characteristics not present in the relaxed material. Bonding Sb-based membranes to any substrate, including a flexible host, will pave the road to fabrication of flexible IR imagers and low power transistors.

7.2 Future work

Epitaxially grown Sb compounds have recently received increasing attention as functional layers in infrared detectors and sources, high mobility transistors, resonant tunneling diodes and low-power analog and digital electronics. Sb-based membrane technology has the potential to improve the performance of infrared detectors. Moreover, membrane technology enable wafer-level FPA processing to reduce the cost and

Chapter 7. Future work

increase the yield in infrared imagers fabrication and packaging. I have done a comprehensive study on Sb-based T2SL membrane and fabricated IR photodetectors on Si substrates. in this desirtaion. Here, I propose a few projects using Sb-based membranes for optoelectronic device applications.

1- I design two different methods for the wafer-level processing. More detail about this process is explained in the following section.

2-I suggest to bonded Sb-based T2SLs membrane to Si coated with patterned metal serves as the bottom contact and a metamaterial structure to enhance the near field. The patterned metal layer is a plasmonic coupler structure which enhances absorption in the active area of the photodetectors and increases the signal-to-noise ratio of infrared detectors.

3- Strain engineering the Sb-based compounds to change the strain because it has impact on carrier mobility in S-based structures by considering strain-induced band splitting, band warping and consequent carrier repopulation, and altered conductivity effective mass and scattering.

5- transfer process enables a thorough investigation of electrical transport in the heterostructure via Hall and van Der Pauw measurements, which are not applicable to T2SLs supported by GaSb substrates.

7.2.1 Wafer-level infrared photodetectors

Currently available infrared detectors are classified as either thermal or photonic detectors. Thermal detectors, such as bolometers which work at the wavelengths between 7.5-14 μm , operate at room temperature, thereby enabling low-cost commercial applications, including surveillance and night vision detection in high-end automobiles. Photonic detectors, on the other hand, have much higher performance

Chapter 7. Future work

(sensitivity, responsivity, and speed) compared to thermal detectors and engineering the structure terminate to detection a broad IR wavelength range between 3 to 30 μm but require cryogenic cooling. Besides, the incredible growth in microbolometers over the last 20 years has been enabled by aligned wafer bonding. Many microbolometers have very small moving parts, which must be protected from the external environment. Initially, this was done using special packages at the die level, which was relatively expensive. Wafer-level capping of microbolometers seals a wafers worth of microbolometers in one operation, and these capped devices can then be packaged in a much simpler and lower-cost package. The state-of-the-art for photonic infrared focal plane arrays is realized using a process in which part of the processing is done at a wafer level on the host substrate including mesa delineation, surface passivation, metal evaporation, and indium deposition. This process is followed by a die-level fabrication involving dicing, flip-chip bonding to a silicon read-out integrated circuit, substrate thinning/removal, and packaging. The die-level steps are low yield processes that dramatically increase the cost and fabrication time for the focal plane arrays.

Recently, the DOD has a concerted effort to develop infrared sensors and cameras for low-cost, large-format, and high-performance imaging in the short-wave infrared (SWIR), medium-wave infrared (MWIR), and long-wave infrared (LWIR) spectral bands. These infrared detectors must be able to be fabricated directly on silicon-based readout integrated circuit (ROIC) substrates at the wafer scale. The U.S. Defense Advanced Research Projects Agency (DARPA) in Arlington, Va., issued a broad-agency announcement for the Wafer Scale Infrared Detectors (WIRED) program. DARPA researchers would like the ability to manufacture high-quality miniature SWIR, MWIR, and LWIR detectors as affordably as the industry makes high-quality visible-light digital cameras for cell phones and other small handheld devices.

I believe the Sb-membrane transfer process could enable wafer level fabricate of complicated photonic heterostructures on a host Si wafer and the entire process can be undertaken at a wafer level. Another advantage of using this approach is that the host substrate can be recycled after the transfer is undertaken. We propose a new process flow which gives the capability of wafer-level fabrication and wafer-leveling packaging of photonic detectors. Reducing cost and increasing yield are the results of these two methods.

7.2.2 Method I: Die to wafer integration

In this method, following the crystal growth of the device structures on a sacrificial layer which is grown on GaSb substrate, wafer-level integration starts with the Sb-based membrane transfer to Si substrate and then the following steps take place. There can be several variables for changes within the fabrication procedure but the process is broadly divided into the following steps 1) Pixels or mesas definition using standard photolithography following by ICP etch (BCl_3 gas) 2) Utilizing dry transfer process to peel off the pixels from a whole GaSb growth substrate and transfer them to arbitrary substrate (e.g. Si). This process is explained with details in chapter 3. The substrate should be covered with a conductive layer before transfer which serves as the bottom contact for all pixels. Because of the backside illumination through the Si substrate, this covering conductive layer should be transparent in IR wavelength range, Graphene or very thin layer of metal can be good nominate for this purpose. 3) Next step is pixels passivation to have higher performance devices. Same as the conventional method, different method of passivation such as SiN and SU8 can be used. 4) One step standard photolithography and RIE etch removes the passivation layer from the contact areas and metal deposition on these areas produce metal ohmic contacts for the pixels. In order to hybridizing the detectors to the read out integrated circuit, Indium bumps are required. Like the conventional FPA

Chapter 7. Future work

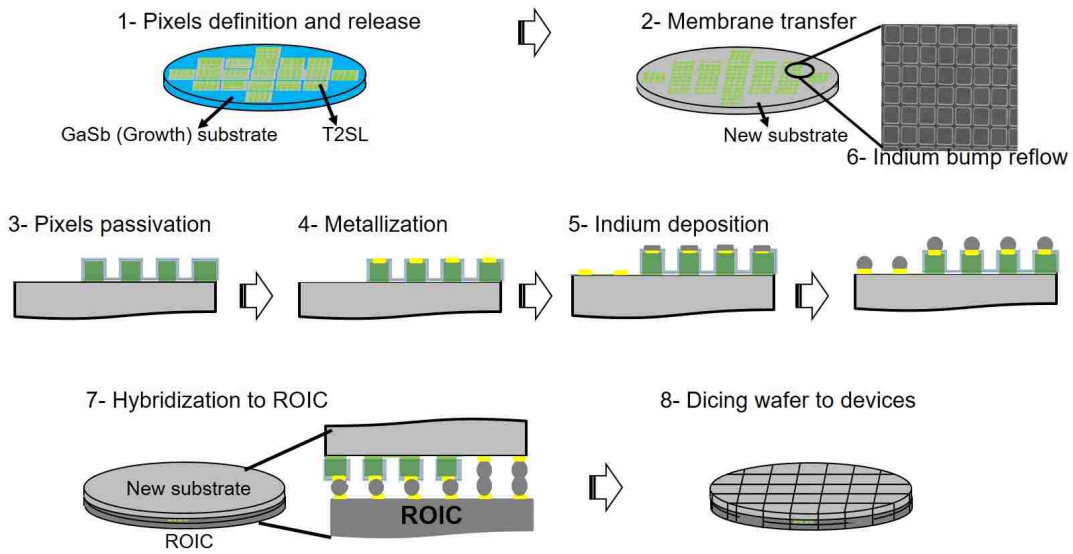


Figure 7.1

fabrication method, following steps are taken to make indium bumps. 5) Standard photolithography to open the areas on metal contacts for Indium layer deposition 6) Indium bumps are shaped using Indium reflow 7) And at the last step detectors are hybridized to ROIC by bonding Indium bumps from both sides. Figure 7.1 shows the schematic of this method.

7.2.3 Method II: Die to wafer integration

In this method, Like previous method, following crystal growth of the device structures on a sacrificial layer which is grown on GaSb substrate, Sb-based membrane is can be release using selective etch process and then transfer to the ROIC directly. There can be several variables for changes within the fabrication procedure but the process is broadly divided into the following steps 1) Defining pixels or mesas using standard photolithography and ICP etch (BCl₃ gass) 2) Utilizing dry transfer process to peel off the pixels from a whole GaSb growth substrate and transfer them

to arbitrary substrate (e.g. Si). This process is explained with details in chapter 3. The substrate should be covered with a conductive layer before transfer which serves as the bottom contact for all pixels. Since this covering conductive layer should be transparent in IR wavelength range, Graphene or very thin layer of metal can be good nominate for this perpose. 3) Next step is passivating the pixels to have higher performance devices. Same as the conventional method, different method of passivation such as SiN and SU8 can be used. 4) Passivation follows by making metal contact on top and bottom contact layer of the structure. One step standard photolithography and RIE etch removes the passivation layer from the contact areas and depositing metal on these areas produce metal ohmic contacts for the pixels. In order to hybridizing the detectors to the read out integrated circuit, Indium bumps are required. Like the conventional FPA fabrication method, following steps are taken to make indium bumps. 5) Standard photolithography open the areas on metal contacts for Indium layer deposition 6) Indium bumps are shaped using Indium reflow 7) And at the last step detectors are hybridized to ROIC by bonding Indium bumps from both sides. Figure 7.2 shows the schematic of this method.

7.3 Membrane metamaterial detectors

Recently, there has been a great deal of interest in confining light at metal/semiconductor interface by using SPW. Employment of SPs for IR sensing applications is a very promising research area, because coupling a detector with surface plasmon modes leads to both resonant and broadband enhancement, *i.e.* encoding of spectral and polarization information within the pixel and improving of detectors signal-to-noise characteristic. To achieve higher intensity near field, the absorber should be placed in that area and very close to the plasmonic coupler structure.

Membrane transfer method for FPAs has the capability of peeling off the pixels

Chapter 7. Future work

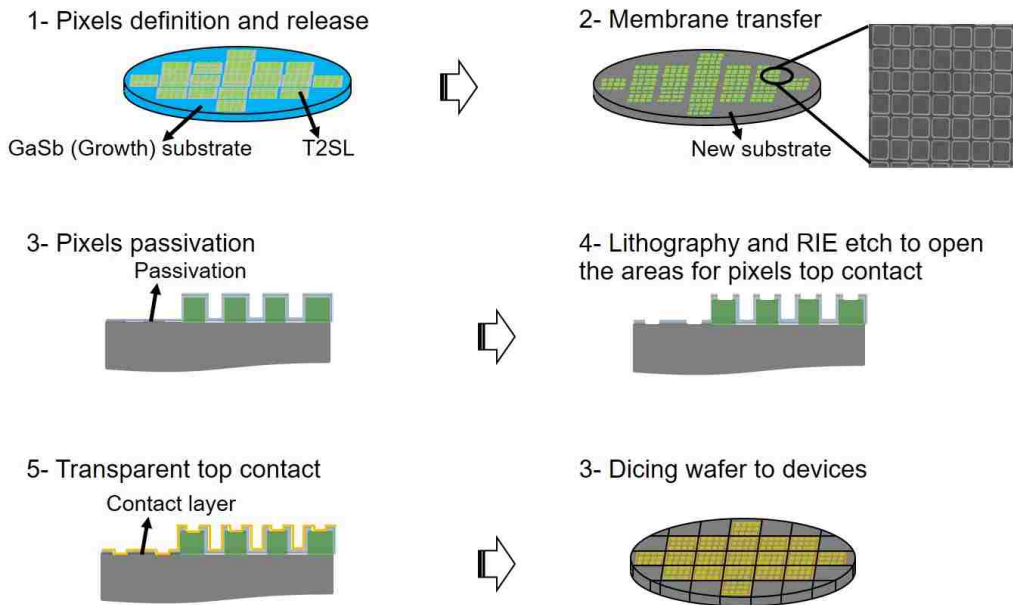


Figure 7.2

from growth substrate and transferring to Si covered with patterned metal layer (SP structure).

Previously, I have demonstrated a broadband enhancement of the SNR of a T2SL MWIR detector integrated with the surface plasmon coupler.

It is known to reduce dark current levels in T2SL detectors both bulk and surface dark current components have to be reduced. Scaling the lateral dimensions of a T2SL detector (e.g. typical mesa dimensions of individual FPA pixels are $20 \times 20 \mu\text{m}^2$) leads to a large surface/volume ratio and surface leakage current becomes the dominant dark current contribution. This component can be significantly reduced by various passivation methods such as sulfide, silicon dioxide and polymeric layers and even overgrowth with wide bandgap materials. Passivation is expected to suppress oxidation of the side walls and saturate dangling bonds to prevent surface states. To reduce volume currents, different methods such as the use of barrier layers to block dark current, nBn structure, volume reduction, etc are used. The volume of

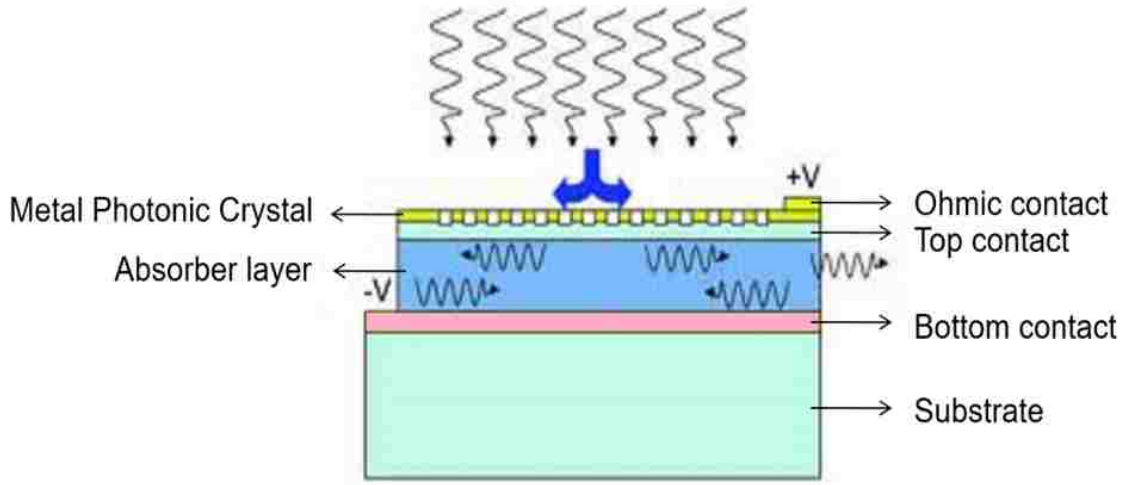


Figure 7.3: schematic of utilizing surface plasmon coupler on a photodetector. In this design, incident light excites the surface plasmon mode at the interface of the metal-semiconductor and couple the light to the detector laterally and enhance the signal

a T2SL detector may be reduced by scaling the active SLS thickness of the device. Then the "bulk" component of the dark current (SRH and thermally generated diffusion current) will be linearly diminished. However, the quantum efficiency (QE) of the device will also be decreased. Reduced volume T2SL with thin layers do not improve the SNR because the signal depends on thickness linearly, while the G-R noise scales as the square root of the thickness. One way to compensate QE and signal loss is by utilization of surface Plasma wave (SPW) assisted coupling of incident electromagnetic radiation laterally into the absorber layer. This way, QE is enhanced in the thin T2SL device, while low dark current levels are maintained. Different research groups have demonstrated enhanced absorption in quantum-dot photodetectors through integration with plasmonic coupling structures.

Generally, a metal film with a 2-dimensional (2D) hole array, referred to as a metal photonic crystal (MPC), has been used as a plasmonic coupler . To use surface plasmon polaritons (SPPs), the active region must be placed in the near field within

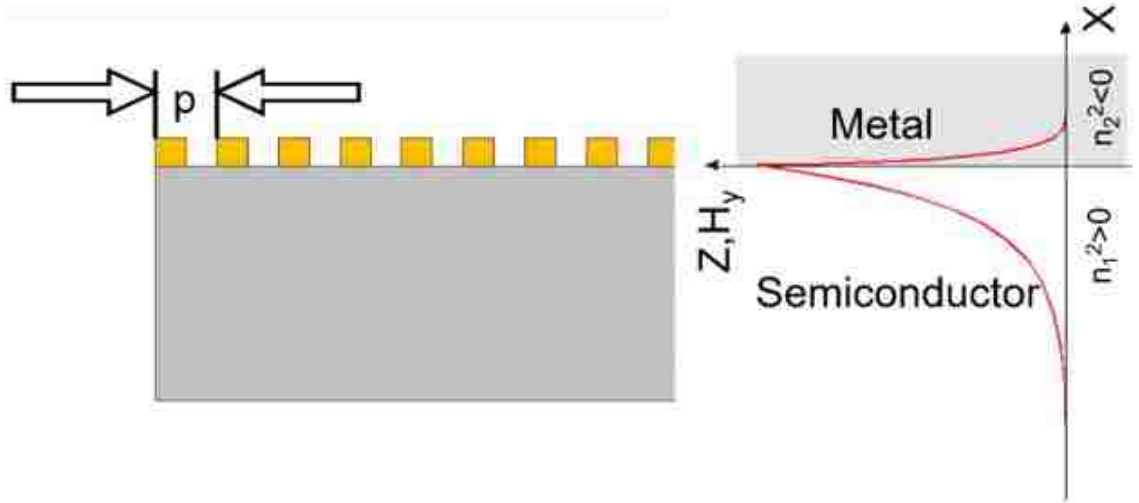


Figure 7.4: Schematic of metal and semiconductor interface and the electromagnetic field behavior at this interface.

the decay length of the plasmonic mode. For a 2-D hole array and normally incident light, the peak wavelength, λ_{ij} , and the SPW evanescent depth, δ_{ij} , are related to period of the array, p , the dielectric constants of the metal, ϵ_m , and the dielectric material in contact with the metal, ϵ_d , as given by equations (1) and (2)

where i, j are the scattering orders of the array. Absorption of the SPW in the T2SL provides a solution to maintaining the absorption of a thick T2SL layer while benefiting from the reduced noise of a thin T2SL layer. Previous SPW studies have shown that for an MPC-integrated QDIP substrate-side illumination is more effective than air-side illumination. On the other hand, conventional industrial FPAs are flipped and light is incident through the substrate. So, to be compatible with manufacturing processes, this flip-chip geometry has to be retained. CMS is a good substitution for MPC for substrate-side illumination (SSI). In this design even though single pixel devices are tested, SSI is used and a corrugated metal surface (CMS) is used as a coupler.

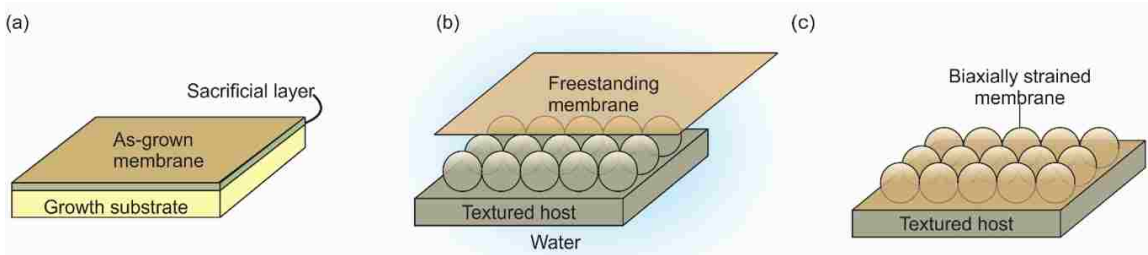


Figure 7.5: (a)-(c) Schematic illustration of membrane transfer to a substrate textured with a 2D array of spheres. (a) As-grown membranes bonded to their sacrificial layer are pseudomorphically strained to the native substrate. Wet transfer of membranes (b) to a textured host results in the film to conform to the shape of the pattern. Strain redistributes across layers as the membrane is freestanding in liquid. (c) Biaxially strained membrane.

7.4 Strain engineering

Antimonide-based membranes can be bonded to any material, including flexible and patterned substrate. Membranes bonded to flexible hosts may be stretched or bent to induce a uniform elastic strain in the film. Alternatively, freestanding membranes can be transferred and conform to micro- and nano-scale patterned features due to their extremely low bending stiffness. In this case the film undergoes local elastic deformation (i.e., bending). Global or local bending may be used to impart a controlled amount of elastic strain in Sb compounds. Here, we demonstrate the potential of membrane technology to strain-engineer Sb-based compounds, thereby enhancing electrical transport in these materials. For this purpose we use continuum mechanical modeling to estimate the amount of strain imparted through bending in a 10 nm InSb membrane cladded by 30 nm Al_{0.2}In_{0.8}Sb. InSb quantum wells exhibit a relatively high hole mobility as the structure is under significant biaxial compressive strain due to the lattice mismatch between InSb and Al_xIn_{1-x}Sb. Transfer of a thin InSb/Al_xIn_{1-x}Sb heterostructures to a textured surface with an array of micro-/nanospheres allows increasing the amount of strain in InSb beyond the limitations of epitaxial growth. Figure 7.5 (a)-(c) schematically illustrate membrane transfer

Chapter 7. Future work

to a textured substrate. Initially the membrane is bonded to its native substrate (Figure 7.5 (a)), and it is pseudomorphically strained to the lattice parameter of the substrate. During release the membrane is freestanding, hence free to elastically relax. Wet transfer (Figure 7.5 (b)) to a textured surface results in the membrane to experience spherical bending and biaxial strain (Figure 7.5 (c)).

Micro/nanospheres on a substrate can be obtained by a variety of processes, including self-assembly of silica spheres and templating by colloidal crystals. We calculate the strain distribution across the thickness a 30/10/30 nm $\text{Al}_{0.2}\text{In}_{0.8}\text{Sb}/\text{InSb}/\text{Al}_{0.2}\text{In}_{0.8}\text{Sb}$ under a spherical bending of radius $R=5\ \mu\text{m}$. Heterostructures are modelled as-grown on $\text{Al}_{0.2}\text{In}_{0.8}\text{Sb}$ relaxed buffers. A sketch of the bent membrane and the calculated in-plane strains are in Figure 7.6, respectively. The strains in the as-grown and freestanding membranes are also plotted in Figure 7.6. As-grown InSb experiences a 1.06% biaxial compressive strain, while no deformation occurs in the $\text{Al}_{0.2}\text{In}_{0.8}\text{Sb}$ layer upon growth (green lines in Figure 4(e)). During release the membrane undergoes elastic relaxation yielding a 0.9848% compressive strain in InSb, and a 0.0752% tensile strain in $\text{Al}_{0.2}\text{In}_{0.8}\text{Sb}$ (red lines in Figure 7.6). Strain values in the released membranes are calculated as described in the Supplementary information. A spherical bending with a radius of curvature $R=5\ \mu\text{m}$ produces a linearly varying strain across the heterostructures ranging from -1.9% to -2.1%, which includes the strain due to the release process.

Figure 7.7 plots the average, minimum and maximum volumetric strain in InSb for R going from 0.1 to 5 μm . Minimum and maximum strains are calculated at the two InSb/ $\text{Al}_{0.2}\text{In}_{0.8}\text{Sb}$ interfaces. Average values of compressive strain remain more or less constant at 2% for R 0.3-5 μm . A higher strain gradient at low R results in the volumetric strain to increase up to 3.8 % at $R=0.1\ \mu\text{m}$.

The strain engineering is applicable for layered Sb-based structures to enhance the carrier transport and make high speed detectors.

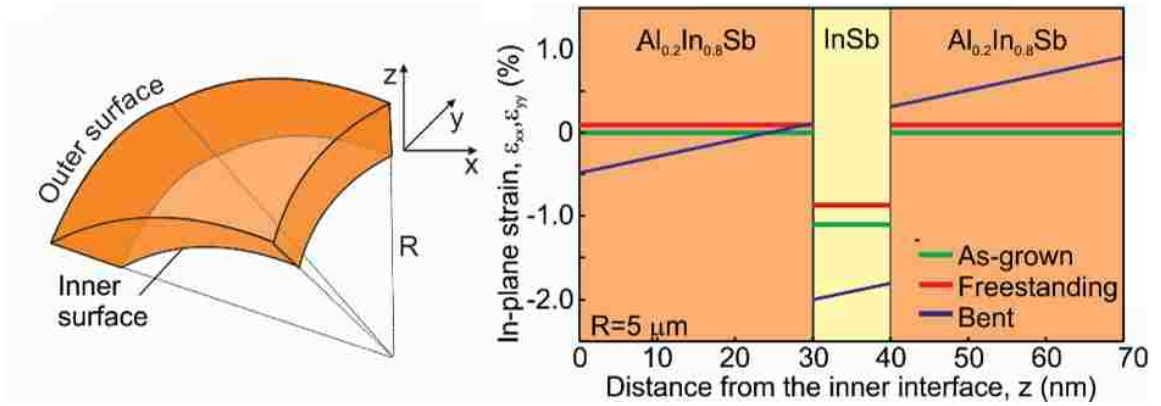


Figure 7.6: The textured host can be obtained through a variety of processes, including self-assembly of silica spheres and templating by colloidal crystals. (a) Section of a membrane undergoing spherical bending with a radius of curvature R . (b) In plane strain profile across the thickness of an AlInSb/InSb/AlInSb heterostructures. Strain in the as-grown (green), freestanding (red) and spherically bent (black) membranes are plotted.

7.5 Electrical transport characterization

Previously mentioned fundamental properties of T2SL absorbers, such as background carrier concentration and vertical carrier mobility, have not yet been very well characterized due to the conductive growth substrate. the background carrier concentration in Sb-based T2SL could be characterized by transferring to insulating substrate and via standard techniques, such as Hall and van Der Pauw measurements. From the measurements made, the following properties of the material can be calculated:

- The resistivity of the material
- The doping type (i.e. whether it is a P-type or N-type material)
- The sheet carrier density of the majority carrier (the number of majority carriers per unit area). From this the charge density and doping level can be found
- The mobility of the majority carrier

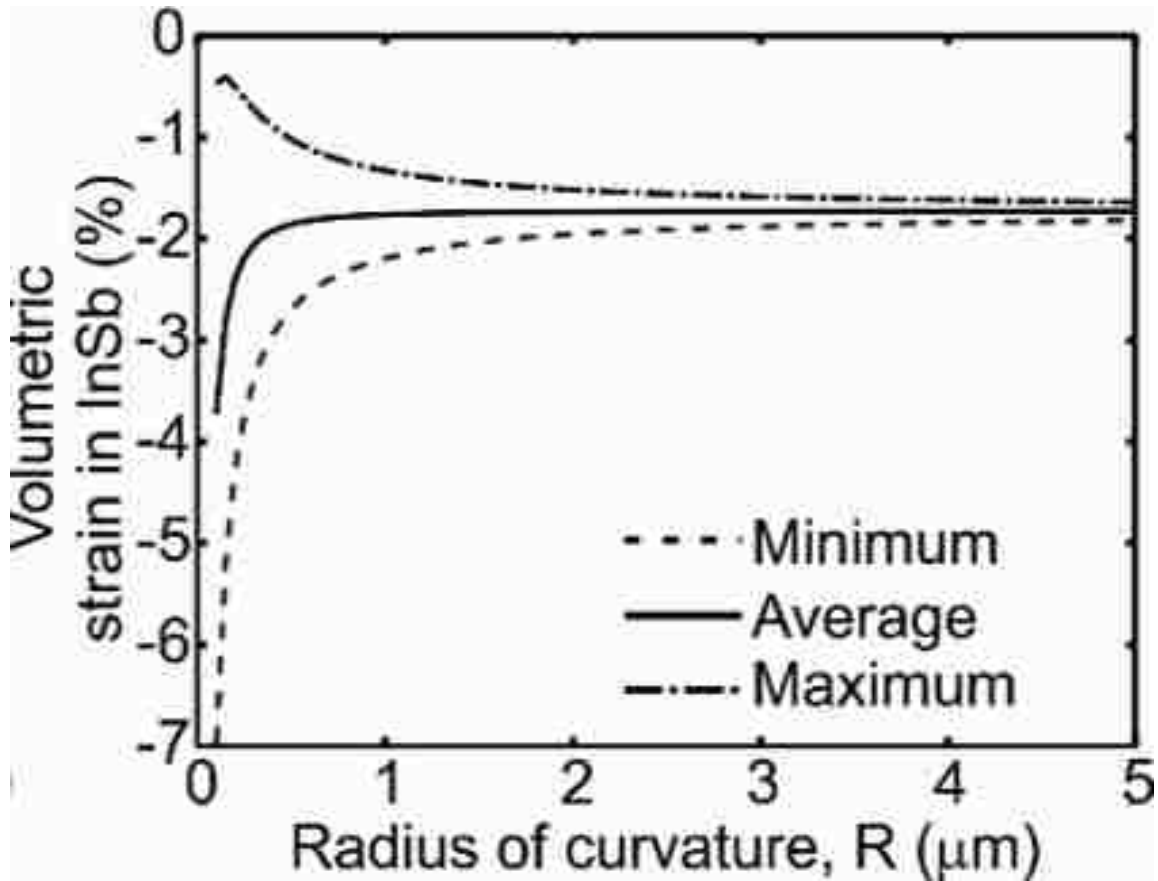


Figure 7.7: Minimum, maximum and average strain in the InSb quantum well vs. a radius curvature varying between 0.1 and 5 μm .

I have transferred $24 \times 24 \mu\text{m}^2$ pixels from GaSb substrate to a non-doped Si substrate, subsequently, one standard photolithography step is applied to open the area for four contact pads on the corners of the pixel. The native oxide on the opened area is removed by 30 seconds soaking the sample in HCl: DI water/ 1:20. Next, we thermally deposit Ti (50 nm)/ Pt (50 nm)/ Au (300 nm) to have electrical contacts on the sample and finally, for Hall measurements, sample should be wirebonded to a sample carrier. 7.8 shows a pixel with 4 contact pads and wires.

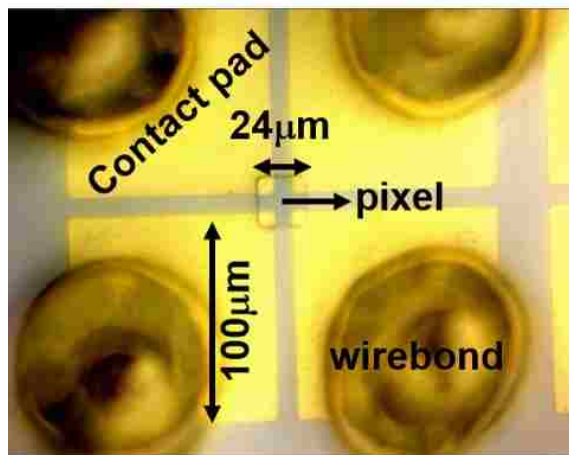


Figure 7.8: Fabricated and wirebonded $24 \times 24 \mu\text{m}^2$ pixel for Hall measurements

References

- [1] Po-Chiang Chen, Guozhen Shen, Haitian Chen, Young-geun Ha, Chao Wu, Saowalak Sukcharoenchoke, Yue Fu, Jun Liu, Antonio Facchetti, Tobin J Marks, et al. High-performance single-crystalline arsenic-doped indium oxide nanowires for transparent thin-film transistors and active matrix organic light-emitting diode displays. *Acs Nano*, 3(11):3383–3390, 2009.
- [2] Francesca Cavallo and Max G Lagally. Semiconductor nanomembranes: a platform for new properties via strain engineering. *Nanoscale research letters*, 7(1):1–10, 2012.
- [3] Jongseung Yoon, Sung-Min Lee, Dongseok Kang, Matthew A Meitl, Christopher A Bower, John Rogers, et al. Heterogeneously integrated optoelectronic devices enabled by micro-transfer printing. *Advanced Optical Materials*, 3(10):1313–1335, 2015.
- [4] Yize Stephanie Li, Pornsatit Sookchoo, Xiaorui Cui, Robert Mohr, Donald E Savage, Ryan H Foote, RB Jacobson, Jose R Sanchez-Perez, Deborah M Paskiewicz, Xian Wu, et al. Electronic transport properties of epitaxial si/sige heterostructures grown on single-crystal sige nanomembranes. *ACS nano*, 9(5):4891–4899, 2015.
- [5] Pornsatit Sookchoo, Faisal F Sudradjat, Arnold M Kiefer, Habibe Durmaz, Roberto Paiella, and Max G Lagally. Strain engineered sige multiple-quantum-

REFERENCES

- well nanomembranes for far-infrared intersubband device applications. *ACS nano*, 7(3):2326–2334, 2013.
- [6] Kuniharu Takei, Morten Madsen, Hui Fang, Rehan Kapadia, Steven Chuang, Ha Sul Kim, Chin-Hung Liu, E Plis, Junghyo Nah, Sanjay Krishna, et al. Nanoscale ingasb heterostructure membranes on si substrates for high hole mobility transistors. *Nano letters*, 12(4):2060–2066, 2012.
- [7] Hyunhyub Ko, Kuniharu Takei, Rehan Kapadia, Steven Chuang, Hui Fang, Paul W Leu, Kartik Ganapathi, Elena Plis, Ha Sul Kim, Szu-Ying Chen, et al. Ultrathin compound semiconductor on insulator layers for high-performance nanoscale transistors. *Nature*, 468(7321):286–289, 2010.
- [8] Eli Yablonovitch, T Gmitter, JP Harbison, and R Bhat. Extreme selectivity in the lift-off of epitaxial gaas films. *Applied Physics Letters*, 51(26):2222–2224, 1987.
- [9] DL Owen, D Lackner, OJ Pitts, SP Watkins, and PM Mooney. In-place bonding of gaas/ingaas/gaas heterostructures to gaas (0 0 1). *Semiconductor Science and Technology*, 24(3):035011, 2009.
- [10] EJ Renteria, SJ Addamane, DM Shima, CP Hains, and G Balakrishnan. 3 μ m thick gasb membrane diodes integrated with cvd diamond heat spreaders for thermally managed tpv cells. In *Photovoltaic Specialist Conference (PVSC), 2015 IEEE 42nd*, pages 1–3. IEEE, 2015.
- [11] Weiquan Yang, Hongjun Yang, Guoxuan Qin, Zhenqiang Ma, Jesper Berggren, Mattias Hammar, Richard Soref, and Weidong Zhou. Large-area inp-based crystalline nanomembrane flexible photodetectors. Technical report, DTIC Document, 2010.

REFERENCES

- [12] Hiroshi Yamaguchi, Remi Dreyfus, Sen Miyashita, and Yoshiro Hirayama. Application of inas freestanding membranes to electromechanical systems. *Japanese journal of applied physics*, 41(4S):2519, 2002.
- [13] Yongfeng Mei, Suwit Kiravittaya, Mohamed Benyoucef, Dominic J Thurmer, Tim Zander, Christoph Deneke, Francesca Cavallo, Armando Rastelli, and Oliver G Schmidt. Optical properties of a wrinkled nanomembrane with embedded quantum well. *Nano letters*, 7(6):1676–1679, 2007.
- [14] Angelo Malachias, Yongfeng Mei, Ratna K Annabattula, Christoph Deneke, Patrick R Onck, and Oliver G Schmidt. Wrinkled-up nanochannel networks: long-range ordering, scalability, and x-ray investigation. *ACS nano*, 2(8):1715–1721, 2008.
- [15] SW Seo, KK Lee, Sangbeom Kang, S Huang, William A Doolittle, NM Jokerst, and AS Brown. Gan metal-semiconductor-metal photodetectors grown on lithium gallate substrates by molecular-beam epitaxy. *Applied Physics Letters*, 79:1372, 2001.
- [16] W Shan, AJ Fischer, JJ Song, GE Bulman, HS Kong, MT Leonard, WG Perry, MD Bremser, and RF Davis. Optical studies of gan and gan/algan heterostructures on sic substrates. *Applied physics letters*, 69(6):740–742, 1996.
- [17] Jau-Jiun Chen, Soohwan Jang, F Ren, Yuanjie Li, Hyun-Sik Kim, DP Norton, SJ Pearton, A Osinsky, SNG Chu, and JF Weaver. Selective and nonselective wet etching of zn_{0.9}mg_{0.1}o/zno. *Journal of electronic materials*, 35(4):516–519, 2006.
- [18] Wan-Jian Yin, Shiyu Chen, Ji-Hui Yang, Xin-Gao Gong, Yanfa Yan, and Su-Huai Wei. Effective band gap narrowing of anatase tio₂ by strain along a soft crystal direction. *Applied physics letters*, 96(22):221901, 2010.

REFERENCES

- [19] Yoon Sung Nam, Sang Wook Lee, KS Baek, SK Chang, Jae-Ho Song, Jung-Hoon Song, Seok Kyu Han, Soon-Ku Hong, and Takafumi Yao. Anisotropic optical properties of free and bound excitons in highly strained a-plane zno investigated with polarized photorefectance and photoluminescence spectroscopy. *Applied Physics Letters*, 92(20):201907–201907, 2008.
- [20] Deborah M Paskiewicz, Rebecca Sichel-Tissot, Evguenia Karapetrova, Liliana Stan, and Dillon D Fong. Single-crystalline srro3 nanomembranes: A platform for flexible oxide electronics. *Nano letters*, 16(1):534–542, 2015.
- [21] A Rogalski. New material systems for third generation infrared photodetectors. *Opto-Electronics Review*, 16(4):458–482, 2008.
- [22] HS Kim, E Plis, JB Rodriguez, GD Bishop, YD Sharma, LR Dawson, S Krishna, J Bundas, R Cook, D Burrows, et al. Mid-ir focal plane array based on type-ii inas/gasb strain layer superlattice detector with nbn design. *Applied Physics Letters*, 92(18):183502, 2008.
- [23] Y Wei, A Gin, M Razeghi, and GJ Brown. Advanced inas/gasb superlattice photovoltaic detectors for very long wavelength infrared applications. *Applied physics letters*, 80(18):3262–3264, 2002.
- [24] HS Kim, OO Cellek, Zhi-Yuan Lin, Zhao-Yu He, Xin-Hao Zhao, Shi Liu, H Li, and Y-H Zhang. Long-wave infrared nbn photodetectors based on inas/inassb type-ii superlattices. *Applied Physics Letters*, 101(16):161114, 2012.
- [25] A Bauer, F Langer, M Dallner, M Kamp, M Motyka, G Sek, K Ryczko, J Misiewicz, S Höfling, and A Forchel. Emission wavelength tuning of inter-band cascade lasers in the 3–4 μm spectral range. *Applied Physics Letters*, 95(25):251103, 2009.

REFERENCES

- [26] WW Bewley, James R Lindle, CL Canedy, M Kim, CS Kim, DC Larrabee, I Vurgaftman, and JR Meyer. Gain, loss, and internal efficiency in interband cascade lasers emitting at $\lambda= 3.6\text{--}4.1 \mu\text{m}$. *Journal of Applied Physics*, 103(1):013114, 2008.
- [27] Cory J Hill and Rui Q Yang. Mbe growth optimization of sb-based interband cascade lasers. *Journal of crystal growth*, 278(1):167–172, 2005.
- [28] Benjamin V Shanabrook, W Barvosa-Carter, Robert Bass, Brian R Bennett, JB Boos, William W Bewley, Allan S Bracker, James C Culbertson, ER Glaser, Walter Kruppa, et al. Engineered heterostructures of 6.1-angstrom iii-v semiconductors for advanced electronic and optoelectronic applications. In *SPIE's International Symposium on Optical Science, Engineering, and Instrumentation*, pages 13–22. International Society for Optics and Photonics, 1999.
- [29] Irina T Sorokina and Konstantin L Vodopyanov. *Solid-state mid-infrared laser sources*, volume 89. Springer Science & Business Media, 2003.
- [30] Brian R Bennett, Richard Magno, J Brad Boos, Walter Kruppa, and Mario G Ancona. Antimonide-based compound semiconductors for electronic devices: A review. *Solid-State Electronics*, 49(12):1875–1895, 2005.
- [31] Brian R Bennett, Theresa F Chick, Mario G Ancona, and J Brad Boos. Enhanced hole mobility and density in gasb quantum wells. *Solid-State Electronics*, 79:274–280, 2013.
- [32] Bin Wu. *Sb-BASED HIGH ELECTRON MOBILITY TRANSISTORS: PROCESSING AND DEVICE CHARACTERIZATION*. PhD thesis, University of Notre Dame, Department of Electrical Engineering Notre Dame, Indiana, 4 2003. An optional note.

REFERENCES

- [33] Jian Ping Sun, George I Haddad, Pinaki Mazumder, and Joel N Schulman. Resonant tunneling diodes: models and properties. *Proceedings of the IEEE*, 86(4):641–660, 1998.
- [34] Arun Goud Akkala. *NEGF SIMULATION OF ELECTRON TRANSPORT IN RESONANT TUNNELING AND RESONANT INTERBAND TUNNELING DIODES*. PhD thesis, Purdue University, Department of Electrical Engineering Purdue University West Lafayette, Indiana, 12 2011. An optional note.
- [35] Mahmoud Omar Manasreh. *Antimonide-related strained-layer heterostructures*, volume 3. CRC Press, 1997.
- [36] Brian R Bennett and J Brad Boos. Antimonide-based compound semiconductors for low-power electronics. Technical report, DTIC Document, 2013.
- [37] Pierre-Yves Delaunay, Binh Minh Nguyen, Darin Hofman, and Manijeh Razeghi. Substrate removal for high quantum efficiency back side illuminated type-ii inas/gasb photodetectors. *Applied Physics Letters*, 91(23):1106, 2007.
- [38] David R Rhiger, Robert E Kvaas, Sean F Harris, Richard E Bornfreund, Yen N Thai, Cory J Hill, Jian V Li, Sarath D Gunapala, and Jason M Mumolo. Progress with type-ii superlattice ir detector arrays. In *Defense and Security Symposium*, pages 654202–654202. International Society for Optics and Photonics, 2007.
- [39] Gert Finger, Reinhold J Dorn, Manfred Meyer, Leander Mehrgan, Jörg Stegmeier, and Alan Moorwood. Hybrid active pixel sensors in infrared astronomy. *Nuclear Instruments and Methods in Physics Research Section A: Accelerators, Spectrometers, Detectors and Associated Equipment*, 549(1):79–86, 2005.

REFERENCES

- [40] James W Beletic, Richard Blank, David Gulbransen, Donald Lee, Markus Loose, Eric C Piquette, Thomas Sprafke, William E Tennant, Majid Zandian, and Joseph Zino. Teledyne imaging sensors: infrared imaging technologies for astronomy and civil space. In *SPIE Astronomical Telescopes+ Instrumentation*, pages 70210H–70210H. International Society for Optics and Photonics, 2008.
- [41] Robert Rehm, Martin Walther, Johannes Schmitz, Matthias Wauro, Wolfgang Luppold, Jasmin Niemasz, Frank Rutz, Andreas Wörl, Jan-Michael Masur, Lutz Kirste, et al. Substrate removal of dual-colour inas/gasb superlattice focal plane arrays. *physica status solidi (c)*, 9(2):318–321, 2012.
- [42] C Cervera, JB Rodriguez, JP Perez, H Ait-Kaci, R Chaghi, Leszek Konczewicz, Sylvie Contreras, and P Christol. Unambiguous determination of carrier concentration and mobility for inas/gasb superlattice photodiode optimization. *Journal of Applied Physics*, 106(3):033709, 2009.
- [43] B Klein, J Montoya, N Gautam, and S Krishna. Selective inas/gasb strained layer superlattice etch stop layers for gasb substrate removal. *Applied Physics A*, 111(2):671–674, 2013.
- [44] Sang Jun Lee, Zahyun Ku, Ajit Barve, John Montoya, Woo-Yong Jang, SRJ Brueck, Mani Sundaram, Axel Reisinger, Sanjay Krishna, and Sam Kyu Noh. A monolithically integrated plasmonic infrared quantum dot camera. *Nature communications*, 2:286, 2011.
- [45] Tara Martin, Robert Brubaker, Peter Dixon, Mari-Anne Gagliardi, and Tom Sudol. 640x512 ingaas focal plane array camera for visible and swir imaging. In *Defense and Security*, pages 12–20. International Society for Optics and Photonics, 2005.
- [46] Mohamed Henini and Manijeh Razeghi. *Handbook of infra-red detection technologies*. Elsevier, 2002.

REFERENCES

- [47] Joanna R Groza and James F Shackelford. *Materials processing handbook*. CRC press, 2007.
- [48] Deborah M Paskiewicz, Boy Tanto, Donald E Savage, and Max G Lagally. Defect-free single-crystal sige: a new material from nanomembrane strain engineering. *ACS nano*, 5(7):5814–5822, 2011.
- [49] Michelle M Roberts, Levente J Klein, Donald E Savage, Keith A Slinker, Mark Friesen, George Celler, Mark A Eriksson, and Max G Lagally. Elastically relaxed free-standing strained-silicon nanomembranes. *Nature materials*, 5(5):388–393, 2006.
- [50] Peng-Fei Qiao, Shin Mou, and Shun Lien Chuang. Electronic band structures and optical properties of type-ii superlattice photodetectors with interfacial effect. *Optics express*, 20(3):2319–2334, 2012.
- [51] Tom Kuech. *Handbook of Crystal Growth: Thin Films and Epitaxy*. Elsevier, 2014.
- [52] Brianna Klein. Defect investigations in inas/gasb type-ii strained layer superlattice. 2015.
- [53] Weilie Zhou, Robert Apkarian, Zhong Lin Wang, and David Joy. Fundamentals of scanning electron microscopy (sem). In *Scanning Microscopy for Nanotechnology*, pages 1–40. Springer, 2006.
- [54] Phuc D Ngo. Energy dispersive spectroscopy. In *Failure Analysis of Integrated Circuits*, pages 205–215. Springer, 1999.
- [55] Bertram Eugene Warren. *X-ray Diffraction*. Courier Corporation, 1969.
- [56] Nutan Gautam. Unipolar barrier strained layer superlattice infrared photodiodes: physics and barrier engineering. 2012.

REFERENCES

- [57] Pulak Dutta. Grazing incidence x-ray diffraction. *Curr. Sci*, 2000:1478–1483, 2000.
- [58] Hedda Malm, Rickard Marcks von Württemberg, Carl Asplund, Henk Martijn, Amir Karim, Oscar Gustafsson, Elena Plis, and Sanjay Krishna. Recent developments in type-ii superlattice detectors at irnova ab. In *SPIE Defense, Security, and Sensing*, pages 83530T–83530T. International Society for Optics and Photonics, 2012.
- [59] EA Plis, T Schuler-Sandy, DA Ramirez, S Myers, and S Krishna. Dark current reduction in inas/inassb superlattice mid-wave infrared detectors through restoration etch. *Electronics Letters*, 51(24):2009–2010, 2015.
- [60] Stephen Myers. Mid-wave and long-wave single uni-polar barrier infrared detectors based on antimonide material systems. 2013.
- [61] Leo Esaki and Ray Tsu. Superlattice and negative differential conductivity in semiconductors. *I B M J RES DEVELOP*, 14(1):61–65, 1970.
- [62] Elena A Plis. *Mid-IR type-II InAs/GaSb nanoscale superlattice sensors*. PhD thesis, The University of New Mexico, 2007.
- [63] HJ Haugan, F Szmulowicz, GJ Brown, and K Mahalingam. Optimization of mid-infrared inas/gasb type-ii superlattices. *Applied physics letters*, 84(26):5410–5412, 2004.
- [64] Theodore Schuler-Sandy. Investigation of infrared detectors based on the gallium-free superlattice. 2016.
- [65] HJ Haugan, GJ Brown, and L Grazulis. Effect of interfacial formation on the properties of very long wavelength infrared inas/gasb superlattices. *Journal of Vacuum Science & Technology B*, 29(3):03C101, 2011.

REFERENCES

- [66] Z Tian, RT Hinkey, Rui Q Yang, D Lubyshev, Y Qiu, JM Fastenau, WK Liu, and MB Johnson. Interband cascade infrared photodetectors with enhanced electron barriers and p-type superlattice absorbers. *Journal of Applied Physics*, 111(2):024510, 2012.
- [67] N Gautam, HS Kim, MN Kutty, E Plis, LR Dawson, and S Krishna. Performance improvement of longwave infrared photodetector based on type-ii inas/gasb superlattices using unipolar current blocking layers. *Applied Physics Letters*, 96(23):231107, 2010.
- [68] J Be Rodriguez, E Plis, G Bishop, YD Sharma, H Kim, LR Dawson, and S Krishna. nbn structure based on inas/ gasb type-ii strained layer superlattices. *Applied Physics Letters*, 91(4):043514, 2007.
- [69] We Shockley and WT Read Jr. Statistics of the recombinations of holes and electrons. *Physical review*, 87(5):835, 1952.
- [70] Antoni Rogalski. Infrared detectors: an overview. *Infrared Physics & Technology*, 43(3):187–210, 2002.
- [71] Matthew A Meitl, Zheng-Tao Zhu, Vipin Kumar, Keon Jae Lee, Xue Feng, Yonggang Y Huang, Ilesanmi Adesida, Ralph G Nuzzo, and John A Rogers. Transfer printing by kinetic control of adhesion to an elastomeric stamp. *Nature materials*, 5(1):33–38, 2006.
- [72] E Plis, MN Kutty, S Myers, HS Kim, N Gautam, LR Dawson, and S Krishna. Passivation of long-wave infrared inas/gasb strained layer superlattice detectors. *Infrared Physics & Technology*, 54(3):252–257, 2011.
- [73] Vinay Bhagwat, Yegao Xiao, Ishwara Bhat, Partha Dutta, Tamer F Refaat, M Nurul Abedin, and Vikram Kumar. Analysis of leakage currents in mocvd

REFERENCES

grown gainassb based photodetectors operating at 2 μm . *Journal of electronic materials*, 35(8):1613–1617, 2006.